J. Moscow Phys. Soc. 8 (1998) 93–170.

Scientific status of plasma focus research

A Bernard[1], H Bruzzone[2], P Choi[3], H Chuaqui[4], V Gribkov[5], J Herrera[6], K Hirano[7], A Krejčí[8], S Lee[9], C Luo[10], F Mezzetti[11], M Sadowski[12], H Schmidt[13], K Ware[14], C S Wong[15], V Zoita[16]

[1] NATIONS UNIES, UNSCOM Secretariate Bldg, S-3035C 42nd Street and 1st Avenue NEW YORK, N.Y. 10017, USA

[2] Facultad de Ciencias Exactas y Naturales, Universidad de Buenos Aires, Buenos Aires, Argentina

[3] EPPRA, X-POLE, Ecole Polytechnique, Palaiseau 91128, France

[4] Facultad de Fisica, Universidad Católica, Casilla 306, Santiago 22, Chile

[5] P N Lebedev Physical Institute, Russian Academy of Sciences, Leninskiĭ Prospekt 53, 117924 Moscow, Russia

[6] Instituto de Ciencias Nucleares, Universidad Nacional Autónoma de Mexico, Circuito Exterior C.U. A.Postal 70-543 04510 Mexico D.F.

[7] Department of Electronic Engineering, Gunma University, 1-5-1, Tenjin-Cho, Kiryu-shi 376, Gunma, Japan

[8] Institute of Plasma Physics, Czechoslovak Academy of Sciences, P.O. Box 17, 182 11 Praha 8, Czechoslovakia

[9] Nanyang Technological University, 469 Bukit Timah Road, 259756 Singapore

[10] Department of Electrical Engineering, Tsinghua University, Beijing, P.R. of China

[11] Dipartimento di Fisica, Universitá di Ferrara, Via Paradiso, 12, Ferrara, Italy

[12] Department of Thermonuclear Research, Soltan Institute for Nuclear Studies, 05-400 Świerk, Warsaw, Poland

[13] Institut für Plasmaforschung, Universität Stuttgart, Pfaffenwaldring 31, D7000 Stuttgart 80, Germany

[14] Defence Special Weapons Agency, 6801 Telegraph Road, Alexandria, Virginia 22310-3398, USA

[15] Physics Department, University of Malaya, 59100 Kuala-Lumpur, Malaysia

[16] National Institute for Laser, Plasma and Radiation Physics, Dense Magnetized Plasma Laboratory, P.O. Box MG36, Magurele, R-76911 Bucharest, Romania

Received 20 September 1997

---

1. Introduction

This article differs from those usually published in the Journal of the Moscow Physics Society in three ways. The first is its volume. The justification for publishing such a large article is that it represents the foundation lying at the base of the International Centre for Dense Magnetized Plasmas created under the auspices of UNESCO. It is proposed that this center, whose temporary location (for five years) will be in Warsaw, Poland, where it will use installations rented from the Institute of Plasma and Laser Microfusion Physics, will begin operation at the end of 1998. The participants of the international working group involved in the preparation of the project hope that the Center will serve simultaneously as a basis for both fundamental research in non-linear and turbulent phenomena in dense magnetized plasmas, and for the preparation of highly-qualified specialists in this area and the propagation of new technologies throughout the world. Naturally, the research performed at the Center will also make it possible to identify and develop possible applied aspects of this research.

The second way in which this article differs from typical JMPS articles is that it does not present the very latest results of research in plasma focus physics, since this text was composed three years ago. However, after numerous discussions, the authors—leading specialists in this field from around the world—chose for this paper data that they felt to be the most representative, reliable, and accurate. Thus, the material presented here, in the opinion of the authors, accurately reflects the current state of research in this field, which has become a classical field of physics over the now more than forty years of its development.

Finally, the reader will quickly see that this paper contains virtually no interpretative material. In particular, there is no discussion of theoretical models or the history for their development. Creating a new Center with wide-ranging goals intended for the study of intriguing scientific problems, we wanted at this initial stage to limit our consideration to the collection of verified experimental data—a reliable "data base"—and not encumber the text with ideological discussions and retrospective considerations. On the threshold of a new technical step in research in which an important role should be played by plasma technology, we thought it appropriate that the future workers in the new Center should fill out a "tabula rasa" based on the development of the results presented here, of nearly a half century of plasma focus physics—one of the most developed sources of dense magnetized plasmas.

1.1. Principles

Over the past thirty years, a particular class of dense magnetized plasmas has been produced by a device generally known as a Dense Plasma Focus or, more simply, a Plasma Focus [1–4]. This is a two-dimensional accelerator that forms a Z-pinch on or near the axis at the end of a coaxial plasma. It was noted to be a copious source of X-rays and neutrons when deuterium is present in the chamber at a pressure of about 1 Torr. With 0.9 MJ stored energy and neon as a working gas, over 120 kJ of K-line radiation were emitted [5, 6] and, in another 0.5-MJ installation, a record yield of more than 10^{12} neutrons was obtained [7]. However, plasma focus devices driven by only a few kilojoules of stored energy exhibit essentially the same behavior, which is the reason there have been so many studies of this phenomenon, including research in connection with academic work.

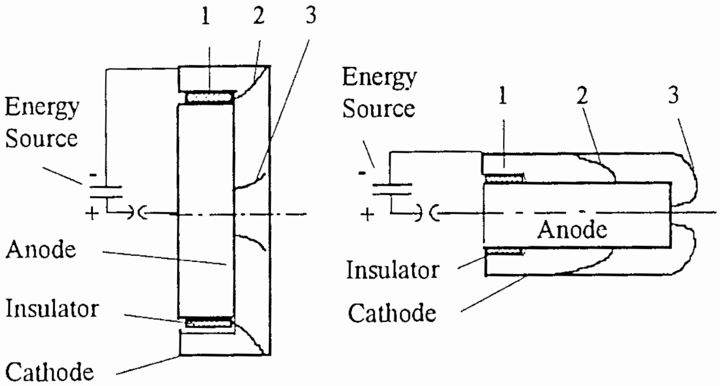

Figure 1. Left: Filippov design; right: Mather design.

Plasma focus machines are pulsed electrical discharges in gases in which microinstabilities and turbulence lead to the generation of powerful beams of electrons and ions and the emission of a large number of X-rays, and also to the generation of fusion neutrons and protons, when the fill gas is deuterium. Two different chamber designs were developed independently by Filippov in the Soviet Union and Mather in the United States. Schematic drawings of the two machines are shown in Figure 1. In the first phase (see 1 in both drawings), when the pulsed power is applied, breakdown occurs along the cylindrical insulator. Under the action of the Lorentz force, the conducting plasma sheath moves from position 1 to position 2 (see Figure 1). In 3, the sheath has reached the axis of symmetry of the chamber.

The machine can be optimized so that the current is maximum when the sheath reaches the axis by appropriately choosing the dimensions—the length and diameters of the electrodes—and of the operational pressure in relation to the characteristics of the energy source. At this time, turbulence and beams occur in a small volume on axis, near the anode end. Most experiments have been done with capacitor banks of a few tens to a few hundred kilojoules under voltages of 20 to 60 kV. The propagation time from breakdown in 1 to sheath on axis in 3 is then a few microseconds. The turbulence and beam generation phase is much shorter, of the order of a few tens of nanoseconds. In a general sense, a plasma focus can be considered a power transformer: the energy progressively stored as kinetic and magnetic energy by and around the moving current sheath is abruptly converted into beams, with a large power increase.

The apparatus is described in Section 2. The following three sections deal with the breakdown, rundown, and pinch phases. Breakdown should lead to the development of a regularly axisymmetric sheath along the insulator. The applied voltage and voltage rise time as a function of gas composition and pressure are important parameters. Experiments have shown that the propagating plasma sheath is not a thin and dense plasma, but rather a fairly broad and diffuse structure. The section that follows describes the anomalous resistance phase that occurs when the plasma sheath has reached the axis under the action of the Lorentz force. This is the fundamental stage of the discharge, in the sense that, without this very large impedance rise, one never observes the generation of electron beams, ion beams, X-rays, neutrons, and other fusion products. These topics are studied in Sections 7–10. Several types of instabilities have been invoked to explain various phenomena observed in the discharge. These are detailed in Section 11. The last two sections give conclusions and references.

1.2. Diagnostics and interpretation

Let us now consider briefly how ideas have evolved since the beginning of research in this field. It was inferred from D–D neutron yield and optical measurements showing the formation of a dense filament on axis that the filament was a thermal plasma, assuming all current flowing in front of the anode pinches to a small radius and communicates the energy to ions, which are then thermalized. There were few diagnostic techniques, and their time and length scales were about 10 ns and 1 mm. Since these early times, progress in detection techniques has improved these resolutions by a factor of at least 10. A large number of refined measurement methods were also developed and applied to the study of plasma focus experiments. There are numerous references connected with this topic, and we have listed here only a few representative ones. The accumulated data have progressively shown that the neutron emission was not thermal, and that complex and short-lived phenomena took place in the plasma. One of the most interesting features is the concentration of energy in space and time that occurs naturally in the plasma when powerful beams are emitted from a small zone near the anode. A sizeable fraction of the source energy (5 to 15 percent) can be delivered to the beams.

While the general features of plasma history are more or less clear, further progress is needed to develop more detailed explanations of the relevant phenomena. Clearly, improving diagnostics and instrumental resolution is one way to accomplish this. Even at the present stage of data measurement, we would certainly improve our understanding of the physics if various diagnostics could be applied to a single plasma under study. This is not practical for a single laboratory, considering the variety of possible diagnostics and the personnel required to carry them out. This is why a common facility in which diagnostics developed at various institutes could be installed is the most necessary part of a cooperative program.

1.3. Matching sources and plasma chambers

In addition to data collection and analysis, a large part of the total effort in plasma focus research has been devoted to the development of experiments powered by large energy sources. These were successful in showing that plasma focus experiments can be done using a very large energy or current range—from 20 to 2000 kA. However, difficulties were encountered, and the adjustment of parameters (electrode and chamber dimensions, nature and pressure of the gas) becomes more and more critical as the energy increases. This is probably due to the fact that two types of phenomena occur during a discharge. The first is connected with breakdown, propagation, and concentration, and requires a certain set of parameters—for instance, there is a minimum pressure of the fill gas below which the experiment reproducibility becomes very low. The second type of phenomenon, which occurs when the sheath is in position 3 in Figure 1, is the rapid increase of resistance and the subsequent generation of beams when the drift velocity between the electrons and ions is large. One can favor the development of this effect, essentially, by lowering the filling pressure. It is clear that it is not possible to optimize both phenomena unless some degree of freedom is added. This was done by injecting gas in the region near the insulator in a transient mode [8]. Good results were obtained using this approach, and such a device should be usable for facilities in the range 0.5–1 MJ and above.

1.4. Comparison with other experiments

The Filippov machine was developed as a modification of the straight Z-pinch to "hide" the insulator zone from the pinch region and prevent restrikes caused by radiation from the hot plasma. The Mather plasma focus was a modified regime from a coaxial plasma gun operated at higher fill pressure. As can be seen in Figure 1, the geometries of experiments in the two cases are fairly different, and the first phases are also different. However, since the sheaths are well formed and do not suffer from restrikes, they both end up with the same interaction of a linear current discharge with the plasma.

It is interesting that other experiments exhibit comparable phenomena. The most obvious case is the standard Z-pinch, when operated at the proper pressure [9]. There are also so-called "exploding wires", in which the source is a megavolt line generator [10]. Other experiments include capillary discharges [11], vacuum sparks [12], etc. If operated in a turbulent regime, these experiments all exhibit a strong impedance rise that leads to the emission of X-rays and neutrons when deuterium is present. Although they have not been studied nearly as extensively as plasma focus experiments, it seems likely that the relevant phenomena are essentially the same.

The prime purpose of the International Centre for Dense Magnetized Plasmas is precisely to study the fundamental physics of the interaction of a current with a gas when the conditions are suitable for the development of microinstabilities and turbulence and the generation of beams and radiation.

2. Apparatus description

A plasma focus system can be divided into three principal elements: the electrical energy source and pulsed electrical power circuit driving the plasma discharge; the mechanical, vacuum, and gas hardwares consisting of the vacuum chamber, coaxial electrode system, vacuum system, and gas handling system; and the data acquisition and diagnostic systems.

2.1. Electrical circuit

As in many pulsed electrical power systems, the equivalent circuit diagram of the plasma focus system is very simple, although the actual physical hardware may be quite complex. Figure 2 shows the equivalent circuit of the plasma focus.

The subscripts "o" denote the initial values of various circuit parameters established by the choice of hardware design of capacitors, switches, inductance, and the initial charge voltage. The initial capacitor bank energy is $E_0 = C_0 V_0^2/2$. In energy systems with electrical input energies larger than 50–100 kJ, the capacitor banks are divided into several parallel modules, which are individually switched for ease of control and safer operation. The parallel modules are switched simultaneously using a single master triggering pulse, to keep the jitter among the switching times of the various modules low. This type of high power technology is currently within the means and capability of most laboratories.

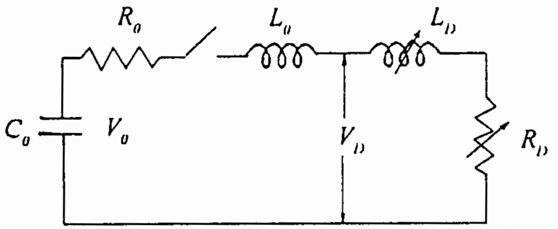

Figure 2. Equivalent electrical circuit of the plasma focus discharge.

The effect of the plasma discharge in the above circuit can be characterized by the combination of a time varying inductance (L_D) and a time varying resistance (R_D). It is now well understood that only part of the total discharge current measured externally (say, by a Rogowski coil) actually flows through the plasma pinch [13], a phenomenon which is sometime termed the current "shedding" effect [14]. This, in fact, remains an interesting area of investigation in plasma focus studies. Note that the equivalent circuit shown in Figure 2 should then be modified by adding a parallel branch to account for this effect.

Historically, the first experiments were done with capacitor banks of a few ten kilojoules with peak plasma currents of about half a megaampere. Later, the scaling law as a function of electrical current (a parameter of more significance to the physics behavior than the stored energy) was investigated, particularly for neutrons. This explains the (loose) terminology that will be found in the followings sections: intermediate size refers to the original experiments with maximum current 400–600 kA (15–50 kJ); small size refers to lower currents (1–15 kJ); and large size to currents above 1 MA (150–1000 kJ). In most cases, the capacitor bank voltage is between 20 and 60 kV, but it is much higher in a few experiments [15, 16].

2.2. Plasma focus devices

As noted in Section 1, there are two distinct electrode geometries for plasma focus devices, named after their respective discoverers around 1960, N V Filippov [2] and J W Mather [3]. In both geometries, the current discharge is initiated along the surface of an insulator in a coaxial electrode region, which is not in the line of sight of the radial Z-pinch region. Figure 1 shows the basic features of the Mather and Filippov plasma focus electrode geometries. The obvious differences are in the electrode dimensions and the diameter (d) to axial length (z) aspect ratio of the inner electrode. A Mather-type plasma focus has a small aspect ratio of typically 0.25 or below, with an inner electrode diameter of between 2 to 22 cm. A Filippov-type plasma focus, on the contrary, has a large aspect ratio greater than 5. Its inner electrode diameter is between 50 to 200 cm.

The electrodes of the plasma focus are usually made of copper or stainless steel, although in at least one device [17], the anode is made of kovar. The electrodes are arranged in a coaxial geometry. The anode may be a solid cylinder or a cylindrical tube, to avoid excessive hard X-ray emission from the anode surface due to electron bombardment. The cathode is in the form of a squirrel cage, consisting of between 8 to 24 copper rods arranged concentrically around the anode. Such an arrangement is usually preferred over a tubular cathode.

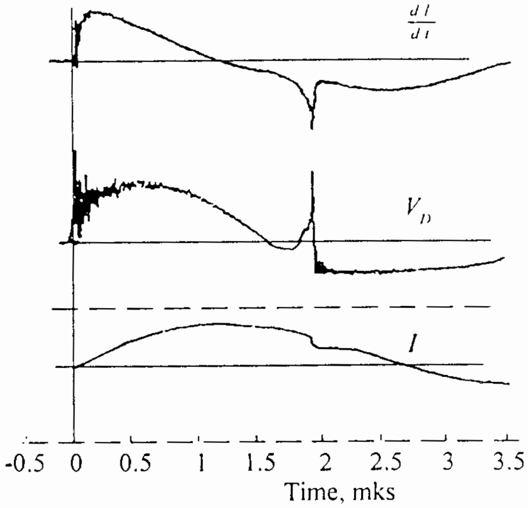

Figure 3. Typical waveforms for the time derivative of the current (upper), voltage (middle), and current (lower) of a plasma focus discharge.

The insulator may be made of pyrex glass, alumina, or ceramic. Several studies [18–20] indicate the great importance of the insulator material for the operation of plasma focus experiments. In one of these [20], the neutron yield begins to saturate at an input energy of 300 kJ when pyrex insulator is used. The situation improves when ceramic insulator is used instead of pyrex.

The experiment chamber is filled with a gas at a low pressure from a fraction of a Torr to several Torrs. The gas most commonly used is deuterium, as the large neutron yield from fusion reactions can be analyzed and serves as a diagnostic tool. Many experiments have been conducted with other gases or mixtures of gases, particularly for spectroscopy studies. Vacuum and gas handling requirements are standard and similar to other plasma studies. The pressure values used in various experiments will be presented in the following sections. In addition to the SI unit for pressure (Pa), the mbar (100 Pa) and Torr (133.322 Pa) are used.

2.3. Data acquisition and diagnostic systems

The most basic diagnostics performed in the study of any plasma focus system are measurements of the discharge current flowing through the plasma and the voltage drop across its electrodes. Information about the dynamics of the plasma focus discharge can be deduced from these parameters. The discharge current of the plasma focus is most commonly measured using a Rogowski coil (total current) or a magnetic probe (localized current distribution). Either the current itself or the time derivative of the current is obtained. Resistive probes are used in many systems to measure the transient voltage during the plasma focus discharge, due to their ease of installation and operation. Since it is not possible to connect the probe to measure the voltage drop across the plasma directly, this measurement is usually made externally across the electrodes of the system. The current and voltage waveforms of a typical plasma focus discharge are shown in Figure 3.

The sharp voltage spike and current dip are features typical of a focusing discharge in which a large increase of the plasma column impedance has occurred. The high-frequency oscillations at the beginning of the signals (and also during the pinch phase) are due to the transmission line connecting the capacitor bank to the electrodes [21]. It is possible that the resistive probe is not fast enough to measure the extremely sharp rising edge during the final few nanoseconds of the voltage spike that is typical of the proper operation of a plasma focus discharge. Capacitive voltage probes have also sometimes been used for this measurement. These have a highly nonlinear frequency response and must be calibrated. In fact, it has been shown [22] that with a properly measured current waveform, it is possible to deduce the corresponding waveform of the transient voltage directly across the plasma without actually measuring it. With reference to Figure 2, it is easy to see that the voltage across the plasma during the discharge can be written:

$$V_{\mathrm{D}} = \frac{\mathrm{d}(L_{\mathrm{D}} I)}{\mathrm{d}t} + IR_{\mathrm{D}} = V_0 - \frac{\int I\,\mathrm{d}t}{C_0} - L_0 \frac{\mathrm{d}I}{\mathrm{d}t} - IR_0 \,.$$

Thus, the waveform of V_{D} can be deduced if the discharge current waveform $I(t)$ has been measured accurately, preferably with a fast digital oscilloscope with one or two gigasamples per second sampling rate (equivalent single shot bandwidth of 250 or 500 MHz). The time integral and time derivative of $I(t)$ can be obtained numerically from the measured waveform of $I(t)$ after it has been transferred into a computer. The system parameters L_0 and R_0 can also be deduced from $I(t)$.

The plasma produced at the densest and hottest phase of the plasma focus is an intense source of radiation, including X-rays. With an electron temperature of around 1 keV, the peak of the emission spectrum of the focused plasma is expected to be at wavelengths shorter than 1 nm. Moreover, the plasma is expected to be fully ionized. Thus, when a gas such as argon, neon, krypton, or xenon is used as the operating gas of the machine, intense inner shell line emission in the X-ray region will be obtained. Hence, it is essential to incorporate X-ray detection systems in the plasma focus system. At present, the time evolution of the X-ray emission from the plasma focus is most commonly obtained using a soft X-ray PIN diode. This type of X-ray detector has a reasonably linear response for X-ray photons with wavelengths from 0.1 to 1 nm. It is also small in size, so that a multichannel system can be set up easily. Photomultipliers are generally used for hard X-rays with wavelengths shorter than 0.1 nm. It is also informative to obtain time-integrated images of the X-ray emitting region of the plasma focus, since this gives an indication of the size and shape of the plasma at its densest and hottest phase. This is usually done using a simple pinhole camera. It is also possible to couple a fast shutter, such as a microchannel plate, to the pinhole camera to obtain gated time-resolved images of the pinch events [23]. An important feature that can be observed even in a time-integrated X-ray pinhole image is the presence of a localized centre of intense X-rays in the plasma focus. Evidence for the filamentation of the current sheet during the pinch phase of the plasma focus can also be revealed by X-ray pinhole images [24].

When deuterium is used as the working gas of the plasma focus, copious fusion neutrons will be produced from the plasma. Neutron yields as high as 10^{12} neutrons per discharge have been measured [7]. The absolute neutron yield per discharge of the plasma focus is usually measured using a foil activation detector setup in which either an indium or a silver foil is activated and the resulting radioactive decay measured by a Geiger counter. A scintillator–photomultiplier system is usually employed for time-resolved measurements of the neutron pulse from the plasma focus.

A variety of other advanced diagnostic techniques have also been developed and used to study the plasma focus discharge plasma. These include Thomson parabola ion energy analyzers [25, 26], laser scattering [27], interferometry, shadow and Schlieren techniques [28], X-ray streak photography [29], Cherenkov detectors for high energy electron detection [30], Faraday cups [31], and neutron pinhole cameras [32].

2.4. Non-conventional energy sources

The physics phenomena of plasma focus experiments essentially concern the interaction of a linear current discharge with a plasma. It is clear that other pulsed current sources can be used, as long as the proper breakdown conditions are provided. Fast capacitors are a convenient energy storage, and have been used to provide plasma focus experiments with a large energy range from 1 kJ to 1 MJ. However, other energy sources have also been used successfully. In capacitive–inductive energy storage, the current rise time can be reduced by almost an order of magnitude and the voltage across the load can be increased by a factor of about five. The driver consists in this case of a standard capacitor bank that charges a series inductor; the inductive energy is transferred to the load by means of a fast opening switch and a closing switch. The use of this type of electrical energy source may substantially increase the neutron yield of a plasma focus experiment [33].

Another way to construct a pulse power source is to store the electromagnetic energy directly in an inductor rather than in a capacitor, as described above. Such a source with a *fixed* inductance has been used in some experiments, and made possible the generation of multiple plasma singularities accompanied by multiple neutron pulses [34].

Other inductive storage systems use *time-varying* inductances: these are based on magnetic flux compression generators and have been used in several countries [35–41] to power plasma focus single-shot experiments. Magnetic flux compression generators [42] are based on the work done by chemical explosives to compress an initial magnetic flux by driving a conducting surface containing the flux, thus increasing the electromagnetic energy of the system. These systems can easily be scaled to energies of tens of megajoules, and are best suited for large, proof-of-principle experiments in which currents of many megaamperes must be delivered to the load.

3. Breakdown phenomena

It has been observed in many experiments that an azimuthally symmetric electrical discharge can be initiated when a high-voltage pulse is applied between the two coaxial electrodes of a plasma focus facility filled with a working gas under an appropriate pressure (usually several mbar H_2 or D_2). Such a discharge is preceded by an electrical breakdown phase that generates some initial plasma configuration through which the discharge current can flow. According to Paschen's law [43], the values of the static breakdown voltage in any plasma focus electrode system operating with deuterium gas at pressures from 1–10 mbar are below 1 kV, i.e., an order of magnitude

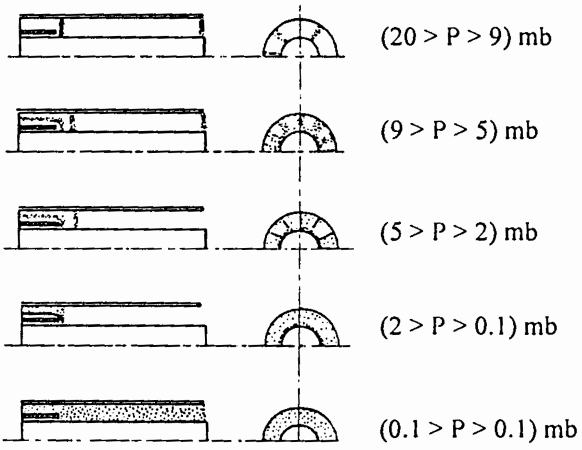

Figure 4. Various modes of the breakdown formation as a function of the initial pressure in a small plasma focus device [53]. The inner electrode diameter is 3.8 cm.

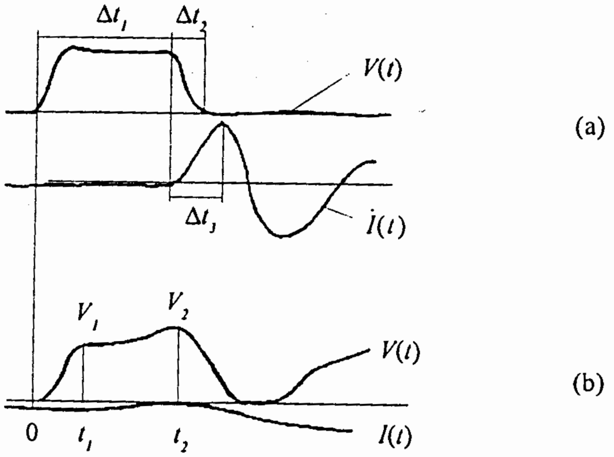

Figure 5. Electrical waveforms characterizing the plasma focus breakdown phase: (a) voltage and current derivative measured in a small plasma focus device [51], (b) voltage and current traces measured in a large plasma focus facility [52]. The amplitude and time scales are different.

lower than the usual bank voltages. Hence, the breakdown in such devices is always a highly overvolted phenomenon. The development of a high-current discharge in a plasma focus system depends substantially on various parameters of the electrodes and solid insulator, as well as on the initial gas conditions [18, 27, 44–55].

3.1. Initial conditions

If the initial pressure in a given electrode-insulator configuration is too low, the discharge can develop in the entire interelectrode volume [18, 49–51]. When the pressure is too high, the discharge can be accompanied by a radial filamentary discharge between the coaxial electrodes [18, 49–53], as shown in Figure 4. If the initial pressure is optimized, a sliding discharge can develop along a tubular insulator.

Sliding discharges along insulators (sometimes called a "gliding discharge" or "flashover") have been investigated by high-voltage engineers for many years [43, 49, 52]. It is often explained as a surface capacitance effect. Usually, the highest electric field appears at the edge of the outer electrode, and the discharge is initiated there. As the discharge develops, depending on the gas and surface conditions, the surface capacitance gradually charges, but the highest electric field remains at the front of the discharge. This promotes the propagation of the ionization front along the insulator. When the sliding discharge reaches the end of the insulator, it connects the two electrodes. After some time (usually 50–500 ns), the conductance of the sliding discharge becomes high enough for the discharge to convert into a plasma sheath (the full breakdown phase).

The entire process, including the emission of primary electrons (probably from the electrode edges and irregularities in the insulator), the formation of electron avalanches, the development of the sliding discharge, and the conversion into the full breakdown phase, can be illustrated by corresponding voltage and current traces, as shown in Figure 5. Usually, the initial voltage rise is followed by a voltage drop, determined by the development of the breakdown and by the parameters of the electrical circuit [18, 27, 47–54].

The time delay τ_D between the switching of the electrical circuit and the electrical breakdown in a plasma focus device appears to be almost independent of the voltage applied (within reasonable limits), but depends strongly on the initial gas pressure [49, 53], as shown in Figure 6. The operational pressure range is limited to values for which the initial sliding discharge develops in a suitable way. Simultaneously, the discharge development depends on other parameters, e.g., the material and dimensions of the insulator [49].

An essential condition for a regular plasma focus discharge is the formation of a distinct quasi-homogeneous plasma layer at the insulator surface (the so-called current sheath), as shown in Figure 7. During the formation and initial motion of the plasma sheath, the discharge current can usually be approximated by a sinusoidal waveform, although the beginnings of the voltage and current waveforms have a complicated character [52–55] as noted above.

In fact, in addition to the primary sliding discharges along the insulator surface, filamentary radial discharges are often observed [45], as shown in Figure 8. Therefore, the total discharge current (I_T) can initially be divided into two parts: a current flowing through the homogeneous plasma sheath (I_S), and a current carried by random filaments (I_R). When the current sheath is pushed by electromagnetic forces away from the insulator, the I_S current becomes saturated, but secondary breakdowns carrying a new current component I_L (Figure 9) can develop in the interelectrode region [50].

Various physical models have been developed to describe the ignition phase. The first one-dimensional approach was proposed many years ago [56]. Two-dimensional two-fluid models [57, 58], developed for magnetohydrodynamic modelling of an entire plasma focus discharge (until the final pinch phase), have assumed the existence of a thin, fully-ionized plasma layer as an initial condition. In a more elaborate three-fluid magnetohydrodynamic model [59], moving ionized gas is used to account for the ionization of the neutral gas.

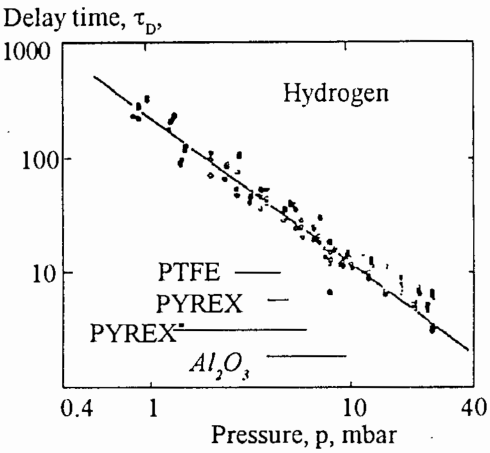

Figure 6. Delay time of break-down as a function of the initial pressure for hydrogen filling, with operating pressure ranges for various insulators, as measured in a small plasma focus device [49].

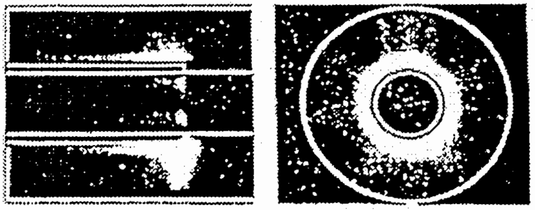

Figure 7. Image-converter pictures of the development of a plasma focus discharge about 100 ns after breakdown along the insulator [49]. The white lines show the electrode and insulator contours.

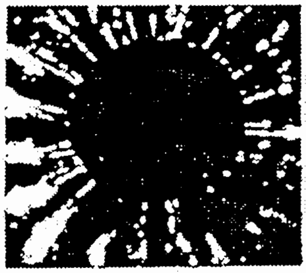

Figure 8. Distinct radial filaments (filamentary vortices) in a current sheath, as observed in a small plasma focus device by an image-converter camera adjusted along the z-axis [45].

A new two-dimensional approach to describe the initial formation of the current sheath near the insulator has recently been proposed [60]. This model is based on the continuity equations for electrons and positive ions, Poisson's equation, the constitutive relations for the drift velocities, and an approximate formula for the ionization coefficient. The basic differential equations were solved numerically using

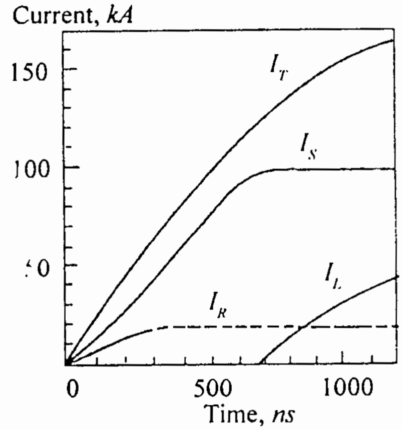

Figure 9. Partition of the total discharge current (I_{T}) among the current flowing through the plasma sheath (I_{S}), the current carried by random filamentary discharges (I_{R}), and the loss current flowing behind the current sheath (I_{L}), as measured in a small plasma focus device [50].

a finite difference scheme with a nonuniform grid. Calculations were performed for a small plasma focus device [60] powered by a 12-kJ capacitor bank with a charging voltage $U_0 = 35\,\mathrm{kV}$ and $(\mathrm{d}U/\mathrm{d}t)_0 = 10^{11}\,\mathrm{V/s}$.

3.2. Experimental studies

Numerous experiments have been carried out in various laboratories to study the formation of plasma focus discharges [18–20, 27, 44–54, 61]. It has been observed that negative polarity of the inner electrode hinders breakdown and the formation of a current sheath. The initial steepness of the current rise, which depends on the inductance and the charging voltage of the electrical circuit, also plays a stimulating role. Detailed measurements with good space and time resolution performed using optical and spectroscopic methods have revealed that:

(1) Under appropriate gas conditions, an ionization front develops along the insulator surface from the cathode towards the anode edge [18, 20, 49–55].

(2) The development of a sliding discharge and formation of a current sheath can be optimized by changing the electrode configuration, as shown in Figure 10. Use of a knife-edge cathode facilitates the plasma focus discharge [18, 48, 50].

(3) The filamentary structure of the current sheath depends on the electrode configuration and the initial operating pressure [18, 27, 45–54, 61]. Motion and interaction of different current filaments can induce the reconnection of magnetic field lines [45, 61].

(4) The axial acceleration of the current sheath is preceded by the formation of a double layer structure consisting of the ionization front and the magnetic piston [27, 44–47, 57].

(5) The breakdown and ionization phase depends substantially on the insulator material and its surface structure [19, 49, 50, 62]. Some conditioning plasma focus discharges, after which hard X-ray emission appears, may also influence the breakdown phase. Such conditioning discharges not only clean the electrode and

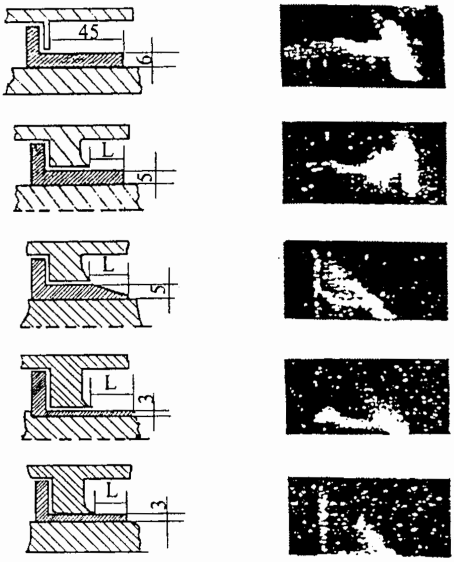

Figure 10. Various electrode–insulator configurations investigated during the optimization of a 13 kJ plasma focus device [18], and corresponding ICC pictures (on a different scale) taken about 20–30 ns after the discharge initiation.

chamber walls, but also modify the surfaces of the anode [63] and insulator [19, 64].

(6) Various active methods influencing current-sheath formation can also be applied, e.g., initial gas puffing or additional preionization, but such methods must still be optimized [19, 27, 55].

3.3. Conclusions

Since large plasma focus facilities have failed to achieve the expected nuclear fusion efficiency, investigations of current-sheath formation become of primary importance for the optimization of high current discharges. Future studies should especially be concentrated on

(1) further experimental investigation of the formation of current sheaths and their fine structure;
(2) further studies of active methods influencing the breakdown and ionization phase, e.g., the application of special materials and configurations, appropriate gas puffing, or intense irradiation of the insulator surface with UV pulses, laser beams etc;
(3) further development of two and three dimensional theories in order to better explain the formation of plasma structures.

4. Current sheath run-down

The second stage in the development of a plasma focus discharge consists in the propagation of a magnetically driven plasma sheath from its formation zone to the axis of the electrode system. Figure 1 schematically shows three consecutive positions of a current sheath during this stage, known as "current sheath run-down". The unifying feature in this stage is the evolution of a current sheath moving against a stationary neutral gas, while, at the beginning of the following stage (the pinch phase), some portion of the current sheath has reached the axis of the device somewhere in front of the central electrode, and must move against a hot and dense plasma. This will be treated in the next chapter, but, in any case, it is clear that the run-down stage is relevant for the subsequent formation of a dense and energetic plasma (the pinch), at least in two respects, namely:

(a) the current sheath should arrive at the axis simultaneously with the first maximum of the discharge current;

(b) the profile (r, z) and structure of the current sheath should have certain characteristics for good pinch formation.

Condition (a) is easy to understand and is a common requirement of all pinch devices. This condition establishes the relationship between the device parameters, which can be approximately expressed by a simple formula in Mather-type devices.

Condition (b) is more complex, and includes the requirements that the radial collapse be axially symmetric, that the (r, z) profile of the current sheath be smooth (wiggly profiles, identified as viscosity dominated Rayleigh–Taylor instabilities [67], are frequently observed at relatively low operating pressure [65, 66]), that the current sheath structure be thin and uniform. These requirements have not yet been expressed in quantitative terms, and the relationships they impose on the device parameters are certainly necessary.

4.1. Conceptual picture of run-down

Due to the large values of the discharge current, the magnetic piston moves against the neutral gas at supersonic speeds from nearly the very beginning of its motion. Because of the $1/r$ dependence of the magnetic field in the electrodes, the current sheath profiles during run-down are curved r–z functions. Since no significant tangential stresses exist in the current sheath, the forces acting on it are everywhere normal to its surface. Therefore, the evolution of the current sheath should be conceived as a sort of swelling balloon, rather than as the movement of a rigid piston. This is a very important point for understanding the particle densities resulting from the sweeping of mass along its path.

The mean free paths for both ion-atom charge exchange and elastic collisions are very small at usual filling pressures, so that the moving structure produces a gas-dynamical shock, which heats and compresses the neutral gas in its front. Therefore, a current sheath structure should be formed between the neutral unperturbed gas and the piston, made up of a dense and hot neutral layer, an ionizing region, a plasma region with currents circulating at its trailing edge, and a nearly vacuum-magnetic field region. Note that this conceptual picture of a current sheath, however reasonable, does not necessarily account for all the details observed in actual experiments, such as the presence of radial filaments in current sheaths. Naturally, the complete structure of a given current sheath is determined by the structure of the current pattern that drives it, and if this pattern is azimuthally filamented (see Section 3), the plasma structure will also be filamentary.

4.2. Measurements and numerical modelling

The diagnostics commonly used to study this stage are, on the one hand, magnetic probes (which detect only the piston structure) and, on the other hand, Schlieren, shadow, and interferometric arrangements, image converter cameras, spectroscopic systems, and other light detecting schemes (which provide information about the plasma zone). Simultaneous measurements of both type of structures with reasonable accuracy are, however, very few.

Magnetic probe measurements have been performed in virtually all laboratories working on these devices. The various current sheath kinematics derived from these measurements are in good agreement, yielding axial velocities (in Mather-type devices) from 3 to 15 cm/μs and radial converging velocities from 10 to 50 cm/μs. The total current flowing in the current sheath can be derived from the integrated signals, and it is frequently found [68–71] that large fractions (up to 50%) of the current going into the device circulates behind the current sheath (particularly in larger devices). The current density profiles obtained from those measurements typically yield rather broad (1 to 2 cm) structures, sometimes with more than one peak [72]. These results should, however, be taken with caution in view of the perturbations introduced by the probe body which, as was recently shown [73], can spuriously enlargen widths and even introduce spurious peaks in the signals. More refined measurements of these structures are needed using non-perturbative methods, such as Faraday rotation techniques.

Measurements of the plasma zone have mostly been performed in the last phase of run-down, when the current sheath leaves the inter electrode space (see the plane of interferograms in Figure 11). Typically, they yield electron densities from 10^{17} to $10^{18}\,\mathrm{cm}^{-3}$, extending several millimeters in the direction perpendicular to the current sheath front [74–76]. Normally, current sheaths are thinner in the region near the central electrode [77]. The electron densities are directly proportional to the filling pressure. The leading edge of the density profile is very steep (<1 mm) during the "coaxial" phase [78, 79] and more relaxed during the convergence phase (~ 3 mm) [80]; this could be a consequence of increased radiative preionization of the neutral gas [80]. All measurements of relative positions between the current sheath and plasma show that the current structure coincides with the trailing edge of the electron density, as expected. Recently, a new technique was developed, based on the measurement of the light intensity emitted by the current sheath in a narrow visible spectral range. This technique can provide maps of the electron temperature in current sheaths with nanosecond time resolution [81], and requires simultaneous measurement of the plasma density. In spite of the fact that it still requires some improvement, it is very promising.

Filamentary structured current sheaths have been detected either through image converter pictures [27, 82, 83] or shadowgrams [84]. There has been little systematic study of this characteristic of current sheaths, but all available evidence suggests that the filaments appear when the device is operated at relatively high pressure values, that is, beyond the optimum pressure for the formation of dense plasma [84]. The experimental and theoretical study of this filamentary structure is certainly a very interesting subject in itself.

Many theoretical descriptions of current sheath run-down have been proposed, ranging from simple to complex. The simpler theories involve various versions of so-called "snowplow models" (either one dimensional or two dimensional [85, 86]), which

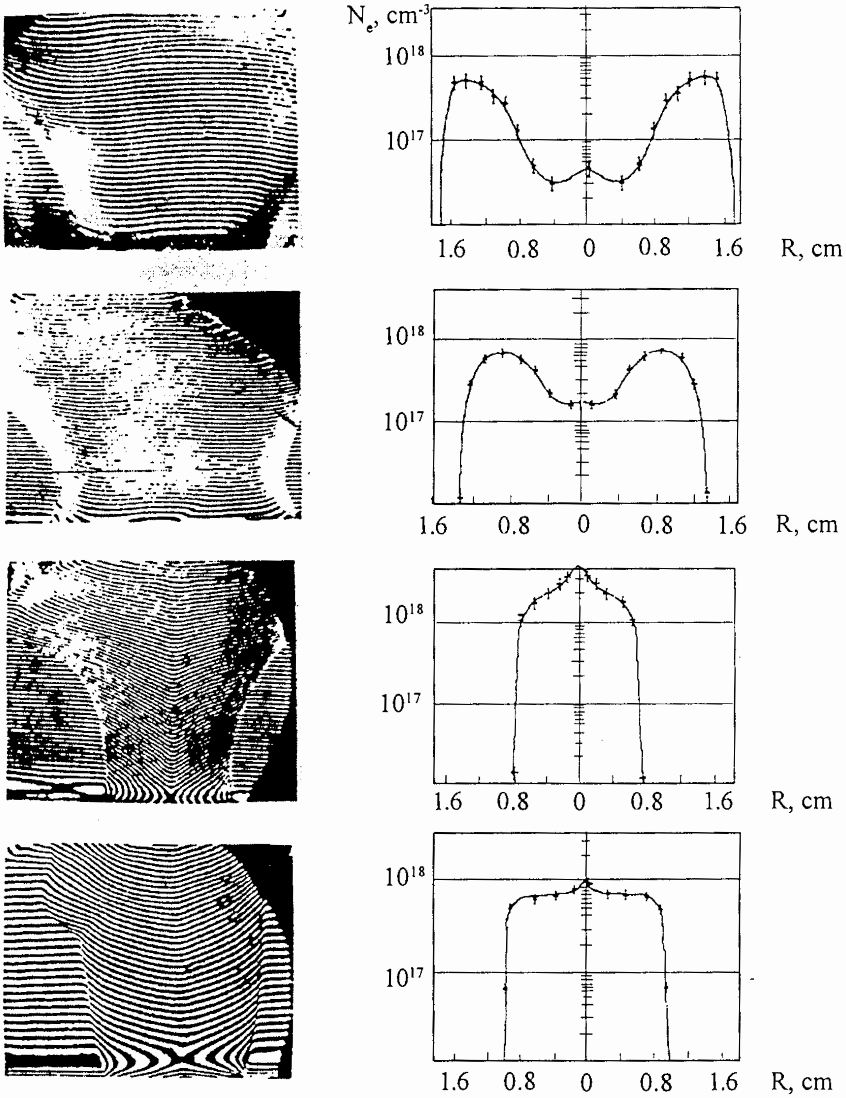

Figure 11. Four ruby-laser interferometry frames taken during a single Filippov-type plasma discharge (35 kJ, 25 kV, 0.3 Torr D_2). The exposure time of every picture is 1.5 ns, and the delay time between frames is 36 ns. The anode is located at the bottom edge of the pictures; the diameter of the pinch near the anode at the time of the so-called "first compression" (third picture from top) is 1.5 cm.

have been shown to predict reasonably well current-sheath velocities and, in their two dimensional versions, also current-sheath profiles [87]. Note, however, that the fitting of this type of model to experimental data frequently requires the introduction of a "sweeping efficiency," which has been interpreted as incomplete sweeping of the filling gas. In some cases (in one dimensional models), this sweeping efficiency resulted from the curvature of the current sheath, but there are other factors (such as filaments) that could be a source of gas leakage through the current sheath.

Plasma or current structures are explicitly ignored by these models, but it is still possible to use them to evaluate the internal energy delivered to the current sheath. Using this approach, a relation was found between the upper pressure cut-off for neutron production and the energy required for ionizing the filling gas [88]. This relation is interesting, since it expresses part of condition (b).

Several two dimensional, time dependent, two fluid (electron and ion) magnetohydrodynamic codes [57, 89] have been developed, which, coupled with an external circuit equation, can describe the evolution of the current-sheath parameters and structure during the run-down. The equations used by these codes are written in Eulerian form, and must be solved on a calculation grid that must have cell size larger than 1 mm, due to memory size and/or calculation time limitations. This is a major problem, since the leading and trailing edges obtained from such calculations can be seen to extend over only a few grid points, so that they cannot be trusted as a description of structures. In addition, a simple dimensional analysis shows that viscous and heat conduction effects become significant only on spatial scales two or three orders of magnitude smaller, rendering irrelevant the inclusion of these terms in the equations.

Another shortcoming of these codes arises from the fact that ionization during the formation and propagation of a current sheath is not taken into account. In fact, the filling gas is assumed to be fully ionized from the very beginning of the calculations. Other studies have been done to overcome these limitations. A three-fluid, one-dimensional, time-dependent magnetohydrodynamic code including ionization processes was presented in [59], and later [90], a similar two-dimensional code was developed. The results of these studies are limited to special cases, and no systematic exploration of variations of the current-sheath structure with device parameters was given, probably due to the large calculation times involved. In any case, the grid sizes used were still undesirably large. It was shown, however, that, in some cases, sizable fractions of the fill gas were left unionized behind the current sheath.

Another treatment of the ionization dynamics was undertaken [91] using a scheme that was one-dimensional and stationary, but included two excited atomic states (five fluids) and took into account radiation. One of the advantages of these models is the minor computational effort they require, which enabled the use of very small spatial scales and, consequently, the parametric study of the current-sheath structure. The results show that the ionization scale is very small (~ 0.1 mm) and that radiative energy losses can become significant (~20%), depending on the parameters used.

4.3. Conclusions

Further work is clearly required for adequate modeling of current sheaths. Two-dimensional magnetohydrodynamic codes require grid sizes that are much less than 0.1 mm if they are to describe reasonably well shock heating and ionization growth, but this is nearly impossible to do with current computers. A possible way to tackle this problem is to use Lagrangian schemes, which, notwithstanding their difficulties (i.e., cell deformations), greatly reduce memory and time requirements. Since the structure of the current sheath at the end of run-down will be the initial condition for the following pinch stage, the need of having an accurate description of the run-down stage cannot be overemphasized.

The interaction of a current sheath with the electrodes has thus far received little attention [92, 93]. This problem is relevant for the operation of larger devices, and is important for our understanding of certain possible technological applications (e.g., coatings). Both experimental and theoretical studies of this subject are required.

5. Pinch phase

In the development of a plasma focus discharge that begins with breakdown along an insulator, resulting in the formation of a current-carrying plasma sheath, followed by the acceleration of this sheath as a consequence of the current rise during the run-down phase, the pinch phase is the final phase of plasma compression. This pinch occurs on axis near the current maximum, and plays a very important role, due to its extremely high energy density, transient character, and the fact that it is a source of intense radiation, high-energy particles, and copious nuclear fusion products. The main phases of a plasma focus are strongly interrelated. It is known that the structure of the current sheath as it is formed during the breakdown has a strong influence on the pinch phase. The pinch phase and, especially, the associated emission phenomena (X-radiation, e beams, ion beams, neutrons) have been the primary subject of plasma focus research during the last three decades.

The pinch phase starts with the rapid collapse of the azimuthally symmetric, but non-cylindrical, funnel-shaped plasma sheath (driven and penetrated by the current sheath) toward the axis. A dense and hot plasma column 1 to 15 mm in diameter and 10 to 70 mm in length is formed. Optimization of the pinch depends on various parameters, including the rate and manner with which the magnetic energy in the interelectrode space (and partly outside, in the external circuit) is converted to plasma and particle energy.

An example of the dynamic behavior of a pinch (280 kJ, 500 Pa D_2) is presented in Figure 12, which shows a sequence of interferograms (exposure 1 ns, $\lambda = 337\,\mathrm{nm}$) [94]. The reference point in the chronology is the time of the first compression to minimum radius ($t = 0$, $r = r_{\mathrm{min}}$). Following this first compression, the plasma column expands ($t \approx 80\,\mathrm{ns}$) and is compressed again locally ($t > 100\,\mathrm{ns}$) due to $m = 0$ instabilities. Measured radial-compression velocities are in the range from 0.7 to $6 \times 10^5\,\mathrm{m\,s^{-1}}$, and depend mainly on the filling density [20, 47], current density, geometry of the electrodes, and structure of the current sheath. Figure 13 shows two streak-pictures [95] (for the same (!) initial discharge parameters: 500 kJ, 600 Pa D_2) for a "good" (with regard to neutron yield) and a "poor" shot. The velocities in the two shots differ by more than 45%. The pinch time t_{p} can be defined as the time between the first compression and the $m = 0$ instability. This time correlates with the neutron yield: the shorter t_{p}, the higher the neutron yield (for fixed discharge parameters). The time t_{p} is much larger than the radial Alfvén transit times of the pinch column; this is usually attributed to the strong axial flow, the two-dimensional curvature of the current flow, $\boldsymbol{B}\times\nabla\boldsymbol{B}$ drift [47], the influence of self-generated axial magnetic fields [96], and, possibly, plasma turbulence.

Magnetohydrodynamic calculations are generally inadequate to describe the pinch phase, while they are quite useful for describing the run-down phase, as well as the compression phase up to the time when the sheath reaches the axis [97, 98]. In order to study the pinch phase in more detail, it is convenient to divide it into several subphases [94] (see Figure 14). Maximum values of the electron density

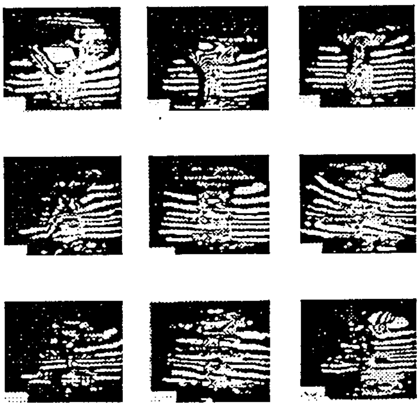

Figure 12. Interferograms of the same discharge on POSEIDON (280 kJ, 60 kV, 500 Pa D_2, hollow inner electrode, 131 mm diameter). The interferograms were taken at the following times: first line from left to right, -26 ns, 7 ns, 29 ns; second line, 54 ns, 81 ns, 107 ns; third line, 127 ns, 146 ns, 159 ns. Neutron emission maxima occur at $t=0$ (first pulse) and at 170 ns (second pulse) [94].

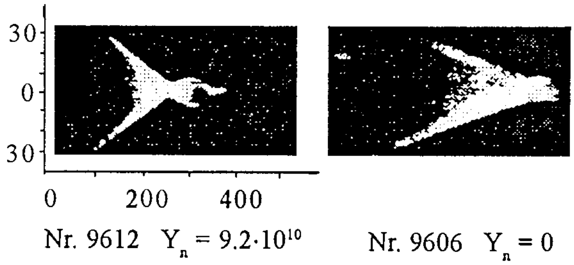

Figure 13. Streak pictures taken for a "good" and a "poor" discharge (500 kJ, 80 kV, 600 Pa D_2, insulator material Al_2O_3) [95].

and electron (ion) temperature have been determined by spectroscopic [99, 100], interferometric [27, 94], laser scattering [27, 101] and other methods [100, 102]. These values were found to be

$$5 \times 10^{18}\,\mathrm{cm}^{-3} < n_{\mathrm{e,max}} < 10^{20}\,\mathrm{cm}^{-3}$$

$$100\,\mathrm{eV} < T_{\mathrm{e,max}} < 2\,\mathrm{keV}$$

$$300\,\mathrm{eV} < T_{\mathrm{i,max}} < 1.5\,\mathrm{keV}$$

Apparently, the peak values of n_e, T_e, and T_i are rather universal, and do not scale appreciably either with the size (energy) of the plasma focus or with the initial conditions. There is, however, a tendency for low filling densities to be more favorable for high electron temperatures. Some researchers claim that "good" shots are also characterized by high electron temperatures [100], whereas laser scattering results have strongly indicated that there is no correlation between neutron yield and the electron or ion temperatures [101].

Comparative experiments with 100 kJ plasma focus devices [103] demonstrated that the pinch phase in Mather-type and Filippov-type devices are very similar, including the observed emission of X-rays and neutrons. Questions remain with regard to the instabilities in the two cases.

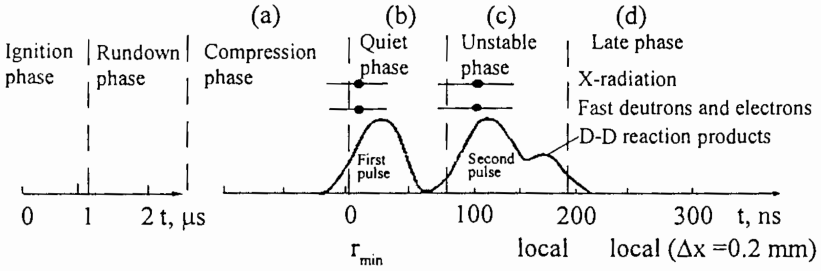

$\hat{n}_e$, cm^{-3}	10^{19}	$2\cdot10^{18}$	10^{19}	$3\cdot10^{19}$
$\hat{T}_e$, keV	2	0.8	17	4
$\hat{E}$, $kV\ /\ cm$	30	300	700	4000
$\hat{B}$, $Tesla$	70	480	300	1800

Figure 14. Plasma focus phases with emission of D–D reaction products (neutrons, protons), X-radiation, electrons, and deuterons. Data for the electron density and temperature and the electric and magnetic fields obtained experimentally (underlined) or theoretically are also given for the two fusion phases.

The Bennett relation, which assumes a continuous series of equilibria for the pinched column, states that the temperature depends only on the current I and the line density N:

$$T \propto \frac{I^2}{N}\,.$$

According to this relation, the lower the line density, the higher the temperature. One of the advantages of a plasma focus compared to a Z pinch is the reduction of the line density N due to the non-cylindrical form of the converging current sheath (see Section 4.2.). In the fast compressions observed in plasma focus experiments, the Bennett relation is only approximate. More precise calculations have been done taking into account the actual parameters of the ionized gas and the compressing force [104–106].

The time relationships of the main plasma focus phenomena can be illustrated by the time correlations (± 3 ns) between the main diagnostic signals obtained in a medium-energy deuterium-argon plasma focus discharge [107], presented in Figure 15. As shown by the He–Ne laser deflection, the plasma pinch has a duration of ≈ 50 ns, with its end nearly coincident with a second peak in the discharge current derivative. The hard X-ray emission (with a duration of ≈ 50 ns) starts immediately after the pinch decay. Low level soft X-radiation is emitted even before the pinch is formed, and continues during the pinch lifetime. The soft X-ray emission rises sharply during the pinch decay, and reaches its first peak shortly after the break-up of the pinch, continuing at a high, nearly constant level for over 300 ns. The $5\,\mu m$ microwave emission begins at the end of the pinch phase, reaches a peak at the pinch break-up, and then decays slowly, its duration being slightly over 50 ns. The CO_2-laser overdense scattering signal of duration ≈ 15 ns (which was found to correlate with the existence of X-ray-bright spots) occurs during pinch decay, when the soft X-ray emission rapidly rises. A low level of neutron emission is detected during the pinch lifetime, but the main neutron emission rises sharply during the overdense scattering (its recorded long tail may be due to scattering in surrounding structures).

Figure 15. Time correlation (±3 ns) of diagnostic signals obtained in a plasma focus experiment [107]. From top to bottom, with detector specified:

the opposite of the discharge current time derivative (magnetic loop),

infrared plasma emission at $\lambda=5\,\mu$m (cryogenic Cu : Ge detector),

soft X-ray emission in the 1–5 keV energy band (PIN diode),

hard X-ray emission with photon energy above 30 keV (PIN diode),

neutron emission (NE102 scintillator and photomultiplier),

scattered CO_2 10.6 μm) laser light (cryogenic Cu : Ge detector),

and He–Ne laser beam deflection signal (PIN diode).

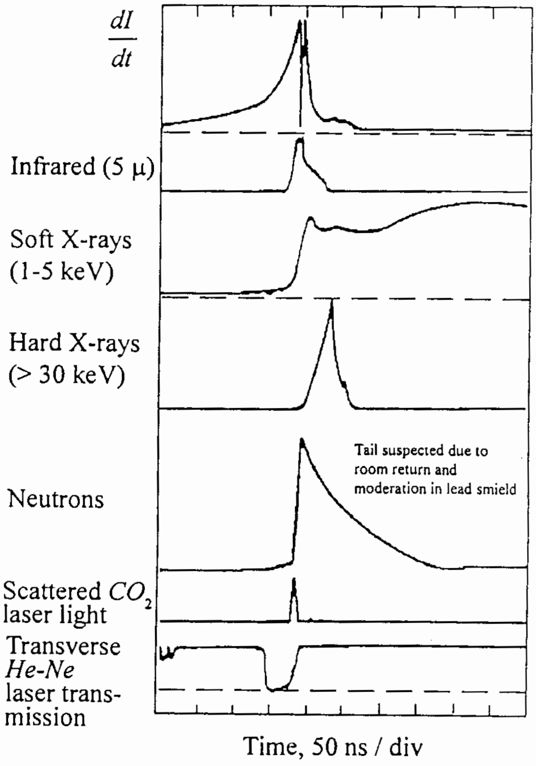

6. Plasma impedance

Experimentally, the neutron and X-ray emissions are correlated with the electrical behavior of the discharge. In spite of the many differences that are exhibited by plasma focus devices, it is universally agreed that a strong and rapid dip on the $\mathrm{d}I/\mathrm{d}t$ oscillogram trace is a necessary and sufficient condition for the emission of X-rays (and neutrons, if deuterium is in the chamber). As will be shown below, this "singularity" indicates a large impedance increase.

6.1. Impedance increase

The measurement of the voltage $V(t)$ across the plasma discharge is done outside the vessel chamber, as close as possible to the electrodes, so that:

$$V=\frac{\mathrm{d}(LI)}{\mathrm{d}t}+RI=\frac{\mathrm{d}L}{\mathrm{d}t}I+RI+L\frac{\mathrm{d}I}{\mathrm{d}t}$$

where L and R are the time-dependent inductance and resistance of the current sheath (the fraction of the inductance due to the connections can be accounted for, if it is not negligible). During the singularity, the current derivative is negative, so that

Table 1

Energy (kJ)	I_c (kA)	$[\mathrm{d}I/\mathrm{d}t]_c$ ($10^{11}\,\mathrm{A\,s^{-1}}$)	V_{pc} (kV)	$V_{pc}I_c$ (W)	$V_{pc}I_c^{-1}$ Ω
0.4	41	0.4	15	6.15×10^{8}	0.37
3.2	195	5.5	83	1.6×10^{10}	0.43
27	520	8	110	5.7×10^{10}	0.21
191	1470	78	420	6.3×10^{11}	0.29
340	1920	83	520	10^{12}	0.27

at time t_c, when it reaches its maximum negative value

$$V_c - L_c\left(\frac{\mathrm{d}I}{\mathrm{d}t}\right)_c = \left(\frac{\mathrm{d}L}{\mathrm{d}t}\right)_c I_c + R_c I_c\,. \tag{6.1}$$

The term $-L_c\,(\mathrm{d}I/\mathrm{d}t)_c$ is positive, and can reach values of hundreds of kilovolts for a large device in which the gun is long, the current is several megaamperes, and the singularity is strong. This term can be much larger than the measured voltage V_c. We see here a specific feature of a plasma focus. The large voltage V_{pc}

$$V_{pc} = \left(\frac{\mathrm{d}L}{\mathrm{d}t}\right)_c I_c + R_c I_c \tag{6.2}$$

created by the terms on the right-hand side of equation (6.2) is, so to speak, screened by the inductance to the residual voltage V_c, which is limited by restrikes and never exceeds more than about 100 kV. Thus, a large inductive gun is important to allow the development of high voltages in the pinch area. This role of the inductive gun is even more important than that already noted: to give the discharge current the time to reach its maximum and to make it possible to use relatively slow energy banks.

The quantities V_{pc}, $V_{pc}I_c$, and $V_{pc}I_c^{-1}$ are given in the following table for a large range of plasma-focus devices powered by banks from a few hundred joules to hundreds of kilojoules [108.]

One striking feature of the table is the near constancy of the peak value of V_{pc}/I_c in the last column, and the corresponding linear growth of V_{pc} as a function of current, which reaches half a megavolt for the largest facility. For a given installation, the peak value of V_{pc}/I_c appears as a kind of factor of merit of the discharge, in the sense that, if it can be increased by adjusting various parameters, the X-ray and neutron yields are also increased. The figures given in the preceding table are those for discharges with the largest peak values.

Due to the high ohmic term V_{pc}/I_c, the current decreases strongly, as shown by measurements of $\mathrm{d}I/\mathrm{d}t$ using Rogowski coils. The ohmic increase can be attributed preferentially to either term of the right-hand side of equation (6.2). Let us examine these two possibilities.

i The second term can be neglected. This follows from the assumption that the plasma column is thermal and its resistivity is given by Spitzer's expression. The first term corresponds to a dynamical effect via which electrical energy is transferred to kinetic energy in the sheath imploding toward the axis with velocity v. In a

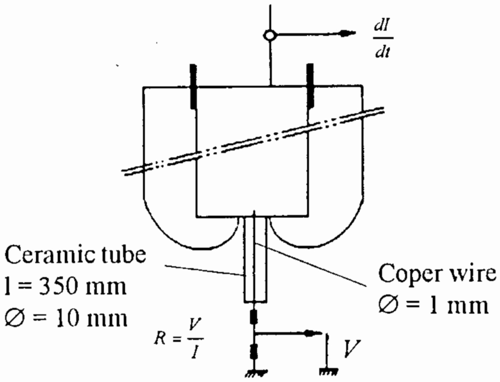

Figure 16. Non-inductive voltage drop along the plasma sheath [109].

simplified analysis, we can view the plasma discharge as a coaxial system with the outer conductor being the cathode and the inner conductor being the plasma sheath imploding on axis. If l is its length, r_{sh} its radius, and R_{K} the cathode radius

$$L = 2 \times 10^{-7} l \ln \left(\frac{R_{\mathrm{K}}}{r_{\mathrm{sh}}} \right)$$

and its time derivative is:

$$\left[\frac{\mathrm{d}L}{\mathrm{d}t} \right] (\Omega) = 2 \times 10^{-7} \times l\,(\mathrm{m}) \times v\,(\mathrm{m/s}) \times [r_{\mathrm{sh}}(m)]^{-1}$$

where v is the sheath implosion velocity.

Resistances of up to 80–100 mΩ—the values found in the first experiments—can be accounted for by a thin plasma-sheath compression, however, this is questionable for the largest values, which require both large velocities and small radii. Numerically, $\mathrm{d}L/\mathrm{d}t$ can take on values above $0.3\,\Omega$ with, for instance, $v = 10^7\,\mathrm{cm\,s^{-1}}$, $r_{\mathrm{sh}} = 1\,\mathrm{mm}$, and $l = 1\,\mathrm{cm}$ or a similar set of values. In fact, the sheath is strongly decelerated when it gathers on axis, so that such velocities, although below the peak value, are fairly high, particularly in view of the fact that the plasma impedance remains high over 50 ns or more: this would imply a sheath displacement of 5 mm at $10^7\,\mathrm{cm\,s^{-1}}$, which is too large for the radius considered here.

If the current sheath was compressed to a 1 mm radius, nearly all of it would be carried by the dense filament. The electrical behavior of the discharge should then be closely related to the filament compression. In fact, this is *not* the case, and electrical singularities and corresponding high X-ray and neutron yields are occasionally seen at times when optical measurements show that the filament is not compressed uniformly.

Experiments were conducted to measure the voltage drop along the axis of the device in the zone where the dense filament usually forms [109], as seen in Figure 16. In spite of the large diameter of the protecting ceramic tube, the characteristic singularity is observed with positive polarity.

ii The first term can be neglected. This implies that the purely resistive term is the most important. The experiment shown in Figure 16 provides support for this possibility in a direct way, since the voltage probe is outside the magnetic flux and measures only the resistive term.

The preceding discussion was based on measurements done with Mather-type experiments. In Filippov devices, lower implosion velocities and larger current-sheath radii are observed, so that inductive effects are even lower. It is thus concluded that the resistivity of the current-carrying sheath must be much higher than the value given by Spitzer's formula (geometrical effects are not possible).

Scattering experiments support the idea that non-thermal processes take place in the sheath. This was demonstrated during filament break-up [27], but also when the sheath was in the compression phase. Observations have been done 10 mm from the anode solid surface and at a radius of 12.5 mm. The scattered light intensity was measured ahead of, at, and behind the dense part of the sheath [103]. The dense part is thermal or nearly thermal, while scattered signals are visible in the two other cases, in spite of the fact that the density gradients are steep. This implies that there is a non-thermal plasma whose extent is centimeters, as opposed to millimeters for the dense part. The scattering from the plasma behind the sheath is anisotropic, with fluctuations larger along the z axis, which indicates that current flows behind the dense part, consistent with other measurements done with magnetic probes [103, 110].

At this time, there is not yet universal agreement about the origin of the ohmic impedance, and this should certainly be a subject for future investigations. Whatever its cause, however, it is possible to deduce simple extrapolation laws based on the virtually constant value 0.2–0.5 Ω observed experimentally in a large range of devices. The voltage developed along the plasma filament scales as I, taking the plasma resistance to be constant. In a similar way, the power scales as I^2, as does the energy, since the resistive phase lasts 30–50 ns.

6.2. Beam generation

Sections 7 and 9 are devoted to detailed studies of electron and ion beams, respectively. The only aim of this section is to put their gross characteristics into perspective with the electrical properties of the discharge. Deuteron beams were observed as a consequence of interferometric measurements of the plasma density [27] during and after the filament maximum compression. In particular, the development of an ionized bubble is created by deuterons emitted near the anode moving outwards from it with energies of 10–20 keV in a 500 kA device.

The spatial extent of the deuteron beam was independently determined by measuring the zones in the chamber where the neutrons originate. In addition, by changing the geometry of diaphragms and obstacles close to the anode, it is possible to show that the deuteron beams emit neutrons as they move outwards from the anode, leading to an increase in the duration of the neutron emission. This duration is much shorter when a high density (solid) CD_2 target is placed in front of the anode. In this case, the penetration of the deuterons into the target is only a few microns. However, the analysis here simplifies the complexity of the phenomena, as it was shown that microbeams of medium energy deuterons can interact during gyration around magnetic field lines (see Section 9).

It is observed experimentally that the X-ray emission in neutron-producing devices is large, and comes mostly from the anode when it is in solid metal. This shows that an energetic electron beam strikes the anode, where Bremsstrahlung radiation is emitted. Experiments were conducted on a 2 MA device to find the relationship between the electrical parameters and the beam characteristics [103, 111, 112]. These

Table 2

plasma electrical voltage:	0.5 MV	electrical power:	1 TW
electron energy:	0.2–0.3 MeV	electron beam power:	0.3–0.45 TW
ion energy: (interaction in gas)	0.3–0.4 MeV	ion beam power: (interaction in gas)	0.4–0.5 TW
ion energy: (interaction in solid)	0.3 MeV	ion beam power: (interaction in solid)	0.3 TW

were deduced from neutron and Bremsstrahlung measurements. In the case of neutrons, these measurements were done using two different setups: one with a usual chamber filled with deuterium, and the other with a CD_2 target.

The detailed studies presented in Sections 7 and 9 indicate that the electron and ion beams created through turbulent phenomena do not have a very simple structure: the particles have different energies and directions. The neutron and X-ray data are, consequently, limited to providing estimates of the deuteron and electron energies and of the beam powers. One interesting feature of Table 2 is the convergence between the electrical and beam values. This is no coincidence: the same convergence is present in a 500 kA device.

It appears that the high voltage and power generated by the current–plasma instabilities are essentially transferred to the fast particle beams, so that the scaling laws noted above can probably also be applied to them.

7. Electron beams

7.1. *Introduction*

Energetic electron beams have long been observed in plasma focus experiments with energy much in excess of the discharge voltage. The interaction of the electron beam with the metallic anode has been proposed as a source of hard X-ray emission [47, 113]. Various acceleration mechanisms have been considered to account for these energetic electrons, as well as for the ion beams [113, 114] (see also Section 11.5.). Some of these mechanisms are applicable only to the ion beams, while others are relevant for both ion and electron beams. Below, a review of experimental results on the properties of plasma focus electron beams is presented. Theoretical models for the acceleration mechanisms will be discussed in Sections 9 and 11. The plasma focus experiments considered cover the energy range from 1 kJ to 1 MJ, with initial voltages from 15 to 200 kV and maximum currents from 100 kA to more than 3 MA.

7.2. *Experimental measurements*

Because the total discharge current (and possibly electron beam current) in plasma focus experiments is much higher than the Alfvén–Lawson limit [115], it is difficult to investigate directly the entire electron beam separated from its charge and current neutralizing background. There have been few experiments in which direct measurements of electron beams have been made (as a rule, a small fraction of the total

Table 3

Lab/ Author	Type	Bank Energy (kJ)	Bank Voltage (kV)	Energy (keV)	Efficiency	Reference
Livermore/ Gullickson	M	57	16	150	800 kA/1.2 kJ	121
Stevens/ Bostick	M	5	15	300	10 kA/500 J	139
Lebedev/ Gribkov	F	50	27	100	6–8 kJ	140
NASA/ Harries	M	25	25	50		141
Limeil/ Bernard	M	340	40	300	800 kA	142
Maryland/ Rhee	M	3	17	27–280		118
Illinois/ Stygar	M	12.5	25	27		117
Gunma/ Hirano	M	24	30	<300		143
Old Dominion/ Molen	M	17	14	150–700	30 kA	116
Stuttgart/ Choi	M	28	60	50 >180		123
Stuttgart/ Jakubowskii	M	280	60	300±80		124

NOTA BENE

In the second column, F and M refer to Filippov-type and Mather-type experiments. The fifth column lists the electron-beam current intensity (with duration 25–50 ns) or the energy of the beam.

current is measured). Most measurements use the X-ray emission from a target, frequently the anode, to infer the existence and properties of electron beams. All direct measurements [116–118] have used a Faraday cup to derive the beam characteristics. Some spot measurements of time-resolved spectra have been obtained using additional filters in front of the Faraday cup, as well as using a β-ray spectrometer with a slit in front of it [119]. Time-integrated energy spectra using magnetic spectrometers and photographic recording media have been obtained [117, 118, 120, 121]. Time-resolved measurements performed in the 1960s and 1970s tend to be limited by the bandwidth of the recording instruments to a resolution of 10 ns or so. Recent results [122–124] (see also Section 11) establish the evolution of the electron beams with nanosecond resolution, in particular, using Cherenkov detectors. A summary of reports on the properties of plasma focus electron beams is presented in Table 3.

7.3. Scaling of electron beams

Most measurements of charged particle beams indicate that the peak energy of the particles does not appear to be related to the charging voltage of the capacitor bank or to the size of the bank. Even relatively small devices have reported MeV electron beams and ion beams [30].

Plasma focus electron beams tend to have distinct temporal structures, depending on the energy of the beam. It is convenient to discuss separately the high-energy (> 150 keV) and low-energy (< 150 keV) components of a beam. The low-energy component lasts from 50 to 300 ns, and is produced during the collapse of the current-sheath shock wave on the chamber axis, beginning from the first compression to the end of the pinch decay phase. The high-energy component is produced in short bursts of duration <10 to 30 ns during the first compression [122, 124, 125] and after the disruption of the plasma pinch column [126–129].

Time-integrated electron energy spectrum have been measured directly using nuclear emulsion techniques. Between electron energies of 30 keV and 400 keV, the energy spectrum can be described by a power law:

$$I(E) = AE^{-\alpha}$$

where $\alpha = 2.5$ to 5 depending on the angle of view of the electron beam axis. This spectrum hardens as the bank voltage, and therefore the discharge current, increases [117, 120, 121, 130, 131]. Experiments with nanosecond time resolution [132] have shown that the spectrum of the high-energy component at a given time is very similar to the monochromatic e-beam energy spectrum, but with a certain change of the accelerating E field in time. Thus, the above power law is the result of the time integration of a variable diode-like law.

Note that, in the presence of a strong plasma current in a plasma focus, the low energy electrons, in addition to the restrictions imposed by the Alfvén–Lawson limit, should be magnetized, and cannot be easily extracted. Additional problems can be expected in connection with the propagation of the low-energy beam through the several-torr background pressure of the plasma focus. A number of high-Z gases have been used, and it is not clear whether the spectra reported are relevant for operation with hydrogen.

In small devices, the beam current was found to vary as $I^{(2.9\pm0.5)}$ for a fixed filling pressure, and is close to the total pinch current in large plasma focus devices. When the filling pressure is varied between 0.2 and 4 Torr, the electron beam current was observed to increase as the pressure decreases.

7.4. Optimization of electron-beam production

In a plasma focus, there are difficulties in creating the conditions required to produce a pure or nearly monoenergetic electron beam. The beam production mechanism arises due to particular plasma conditions, but the resulting electron beam interacts with the plasma and modifies the plasma conditions. Such self-modifying situations, coupled with the highly dynamical nature of the plasma focus, make it very difficult, if not impossible, to design a plasma focus for non-transitory electron beam production. Nevertheless, there is a range of operating conditions under which enhanced electron beam production is observed. These will be discussed briefly below.

In general, the filling gas pressure has a direct influence on the number of high-energy electrons produced in a discharge. As the operating pressure is lowered, the number of hard X-rays produced by the electron beam is increased [133]. The reproducibility is reduced, however, as the pressure is lowered [118]. Together with the increase in intensity of the electron beam, there is an increase in its hardness. This low-pressure enhancement is observed down to a certain optimum value, beyond which the focus plasma is poorly formed, and the intensity of the emission decreases [134]. Note that the current flowing in the plasma column is some fraction of the total current, and that this fraction falls from 80% to 60% as the operating pressure is changed from 2 Torr to 0.2 Torr [69]. On the contrary, the higher the operating pressure, the more effective the beam–plasma interaction inside the pinch column, which decreases the absolute X-ray yield even under the same beam production efficiency [127, 135].

In high-voltage plasma focus experiments, the high-energy electron beam usually originates during the first compression, when the flute-shaped, curved plasma sheath coalesces on axis [136]. This is in contrast to low-voltage devices, in which high-energy electron beams have been detected at the time of $m = 0$ instabilities [30, 129]. In high-energy and high-voltage Mather-type devices and during the formation in Filippov-type devices, X-ray measurements demonstrate the presence of a small electron-beam pulse some 50 ns prior to the first compression [30, 127]. The electron beam during the first compression correlates with the symmetry and quality of the collapsing sheath, both of which can, in principle, be modified in a controlled manner. High-voltage operation is beneficial for the creation of a uniform sheath quickly in the initial breakdown phase, with reduced energy losses and impurity ablation from the insulator [137].

In general, the higher the maximum current-discharge magnetic field, the more efficient the beam generation. Devices operating with a higher bank voltage have a higher source impedance for a given plasma current. This higher impedance permits a higher $\mathrm{d}L/\mathrm{d}t$, and thus a higher terminal run-down velocity for the current sheath. The speed of the sheath alone, however, is not sufficient to guarantee proper conditions for the production of an electron beam. The uniformity of the collapse in the axial direction has a strong effect on the yield of the high-energy electron beam. A first compression that progress uniformly along the axis on a time scale of less than 10 ns is associated with strong high-energy beams [136]. In addition, the thickness of the collapsing sheath determines the tightness of the first compression [16, 129]. A broad sheath tends to produce a weak compression, due to preheating of the plasma ahead of the collapsing sheath.

When a small amount of high-Z impurities is present, the collapse dynamics are not grossly modified. However, the structure of the collapsing plasma shell changes: the current-sheath thickness is diminished as a result of enhanced energy dissipation at the front of the collapsing sheath owing to ionization and radiation from these impurities. A small amount of high-Z impurities can increase the discharge reproducibility in medium-size devices [134]; this is usually attributed to modification of the sheath. Increase of the content of high-Z impurities ($Z > 40$), however, appears to draw too much energy from the plasma as it compresses, leading to significantly lowered production of high-energy electron beams in smaller devices [136]. In very small devices, operating in pure argon produces reproducible electron beams, though at the expenses of lower beam current compared with that for lower-Z discharges [118].

7.5. Summary

No specific experiments positively identifying the exact mechanisms for the production of various (early and late, low- and high-energy) electron-beam components have been reported. Detailed correlations have shown that a relativistic component, with an energy much in excess of the operating voltage, is produced around the time of first compression, in the absence of any large-scale disruptive instabilities. This component decays within a few nanoseconds in Mather-type devices, but lasts for up to 200 ns in Filippov-type devices. This is connected with the onset of anomalous resistivity, detected through laser-scattering and other measurements, though a temporal correlation has not been clearly established. The intense low-energy beam is probably associated with an electric field supported by anomalous resistivity. This resistivity is the result of plasma turbulence, in which electrons are scattered by a random electric field, rather than ions. This random electric field could originate from a variety of micro-instability mechanisms. Any plasma conditions facilitating the growth of these instabilities would enhance the production of electron beams.

When the plasma column disrupts, intense electron beams are again observed in both plasma-focus geometries, though the energy of the electrons can be lower or higher than during first compression. The formation of these beams is especially promoted when high-Z impurities are present in the discharge in sufficient quantities.

There have been other reports concerning special properties of plasma-focus electron beams, though these results have not, in general, been corroborated. There have been reports of electron beams in both the forward and reverse axial directions. There are also claims [138] that electrons are emitted in short bunches (1 ps) at regular intervals (10 ps), and that corresponding bursts were observed at microwave frequencies. There is no doubt that microwaves are emitted from plasma focus devices, however, the method used in these studies, which involves the deconvolution of the spectrum from the noise, is fraught with difficulties that can give rise to artifact spectra.

It is clear that significant knowledge can be gained through detailed observations of the evolution of plasma-focus electron beams in conjunction with measurements of the plasma dynamics. Most models put forward so far deal, as a rule, with a single aspect of beam production, whereas the experimental results clearly point toward a complex series of physical processes taking place in the first 40 ns or so of pinch formation. Good-quality measurements of the electron beams produced in plasma focus devices with sufficient temporal, spatial, and energy resolution, together with plasma density and temperature data, will allow us to identify the physics behind the formation and evolution of high-density, high-temperature plasmas, and perhaps elucidate the true nature of truly dynamical pinches.

8. X-RAYS

8.1. Introduction

X-ray emission in plasma-focus devices was initially studied in relation to neutron emission, for hard X-rays [144], or in experiments concerned mainly with the effect of impurities on the overall device performance when using deuterium or slightly heavier gases (e.g., helium, neon [145]), for soft† X-rays. Later, heavier gases were added to the base hydrogen-isotope working gas, or metal inserts were attached to the end of the plasma-focus anode. This made it possible to use X-ray spectroscopy techniques to determine the parameters of plasmas producing highly charged ions of heavier elements and to study their radiation properties (transition energies, term levels, and ionization energies) [146]. Such studies revealed plasma phenomena such as bright plasma spots [147], made it possible to control some plasma parameters during the pinch phase [148], and increased the soft X-ray yield [149–151]. The application potential as an intense soft X-ray source [150, 152], as well as interest in the study of high-energy density states in plasmas and associated radiative-collapse phenomenon, have inspired more intensive studies during the last decade, especially concerning plasma-focus operation in heavy gases [153–156].

Radiation losses via X-ray emission can make a significant contribution to the plasma-focus energy balance in the case of discharges produced in low- or medium-Z gases or hydrogen-heavier gas mixtures. Using medium-Z fill gases (neon or argon), the energy emitted in the form of electromagnetic radiation can easily be of the order of a few percent of the total energy of the capacitor bank [152], reaching in some special cases values as high as 10–15% [5]. At such high radiative energy losses, the X-ray emission has a strong influence on the plasma evolution (plasma dynamics and pinch compression): it has been suggested that the compression produced by the driving current can continue relatively unimpeded until very high densities are reached, and a process of radiative collapse is attained [148, 153, 157, 158].

8.2. Mechanisms of plasma-focus X-ray emission

The electromagnetic radiative processes in a plasma focus cover a range from the emission of a set of individual electrons (as in cosmic ray physics or accelerator physics) to the (quasi-)equilibrium thermal radiation of macroscopic plasma structures. The former type of emission is covered by the electron beams in plasma focus devices (see Section 7), while the latter type would be approached by the intense radiation of bright ("hot") spots. In addition, plasma focus devices emit soft X-rays due to electrons propagating in periodic electron density structures [150].

Most of the energy emitted by plasma-focus devices at X-ray wavelengths is due to the following electron–ion interaction processes: Bremsstrahlung (free–free transitions), recombination radiation (free–bound transitions), and line radiation (bound–bound transitions). Any evaluation of the actual contribution of these processes to the radiation power output requires some assumption regarding the applicable thermodynamic model for the plasma-focus conditions. This is not an easy matter, since no single model is satisfactory for the wide range of conditions attained in a plasma focus. It was shown [146], for instance, that the same experimental conditions could lead to different results if only the composition of the working gas was changed: neon discharges produced plasmas with substantially steady-state populations, while argon discharges did not.

A strong anisotropy of the soft X-ray emission at 1 keV was observed in some plasma focus experiments [150], and considered to confirm the existence of nonequi-

---

† Photons with energy roughly in the range 0.5–10 keV will be regarded as soft X-rays, although sometimes higher energy quanta (30–40 keV) will still be included in this category.

librium states originating from a two-stream instability. This was thought to generate a periodic density structure of short wavelength in the plasma focus, such that the motion of relativistic electrons in this structure would lead to the emission of soft X-ray radiation.

The interaction of the high-energy, high-current electron beams generated in plasma focus devices with an electrode structure is thought to be responsible for the emission of X-rays having a broad spectrum with energies up to several hundreds of keV. However, the mechanisms by which such X-rays are emitted in plasma-focus devices are still not fully understood. At first, it was thought that the X-rays (as well as the neutrons) were emitted by thermal processes [4] occurring in deuterium plasmas with densities estimated to exceed $10^{19}\,\mathrm{cm}^{-3}$ and electron and ion temperatures thought to be several keV [159]. Further work has shown, however, that the dominant hard X-ray emission is due to nonthermal high-energy electrons striking the anode, and that the hard X-ray distribution fits a power-law spectrum [144, 160, 161] and is certainly not due to electrons with a Maxwellian distribution. The fact that the exponential power law for 100–500 keV found for plasma-focus X-rays is similar to the solar flare spectrum at 20–100 keV, which can also be represented by a power law [162], suggests that the magnetic-field decay processes believed to occur in solar-flare phenomena could also contribute to the generation of the fast component of the plasma-focus electron population. Later, measurements with good time resolution [163] showed that the plasma-focus X-ray power law spectrum is the result of time integration over spectra produced by quasi-monochromatic electron beams whose average energies change on a time scale of 10 ns.

8.3. Characteristics of plasma-focus X-ray emission

A plasma focus produces intense pulses of X-rays with durations between a few and a few hundred ns, with energies from less than 1 keV to over 0.5 MeV. Their integrated energy represents a significant fraction of the electromagnetic energy stored in the plasma focus driver. The soft X-ray emission exhibits, generally, two or three pulses, and comes mainly from plasma sources associated with the plasma-focus pinch and post-pinch phases. Hard X-rays are usually emitted in a short (a few to a few dozen ns) pulse, with the source being the anode surface exposed to the fast electron beams generated in the focus region.

The soft X-ray emitting source is situated in the vicinity of the inner electrode face, usually on the electrode axis. It is from less than 1 mm to over 10 mm in diameter, with an axial length of about 0.1 cm to a few cm. The time-integrated image of the region emitting soft X-rays is roughly a cylinder with these dimensions, but spectral filtering of the X-ray image reveals fine structure with bright spots and micropinches [147], as well as filaments inside the pinch and along the axis [24, 159], depending mainly on the composition of the working gas and the energetic level of the device. In reality, the plasma-focus soft X-ray source continuously changes its dimensions, structure, and spectral characteristics on a ns time scale, as indicated by high-speed X-ray photography in many plasma-focus installations covering a wide range of operating parameters [23, 150, 154].

In a low-energy deuterium plasma focus [23, 150, 154], the soft X-ray emission (Figure 17) extends over a time interval of 60–70 ns and features three reproducible peaks (Figure 17(i)). The first of these is emitted by the dense, pinched plasma, the

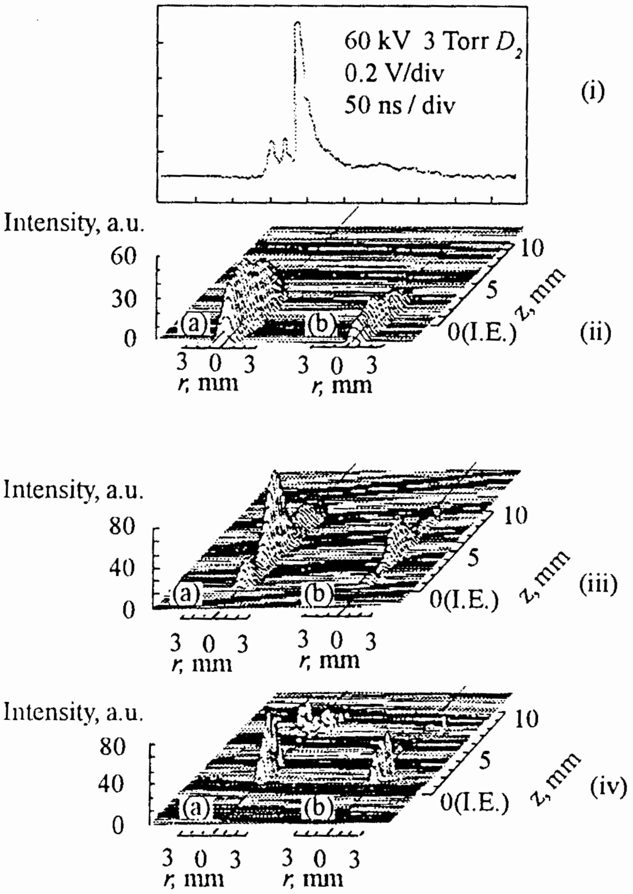

Figure 17. Time and space characteristics of the soft X-ray emission of a low-energy (250 kA pinch current), high-voltage (60–65 kV) plasma-focus device operating with deuterium (3–4.5 Torr) [23]. (i) Soft X-ray emission detected by a PIN diode filtered with 25 μm Be. Spatial distribution of soft X-ray intensity for the (ii) maximum plasma compression, (iii) unstable plasma, and (iv) plasma disruption phases. (Obtained with a two-channel, filtered microchannel plate system with an exposure time of 3 ns and a spatial resolution of 85 μm). (a): 25 μm Be filter; (b): 25 μm Be + 2 μm Al filter. I.E. represents the inner electrode face.

second by the unstable plasma column, and the third (corresponding to the plasma disruption phase) by the face of the inner electrode. The energy of the second peak is below about 6 keV. The spatial distribution of the X-ray intensities corresponding to the three times in the plasma evolution shows that, at maximum plasma compression (Figure 17(ii)), the X-ray emitting region has a diameter of 1.5 mm and a length of 7–8 mm. The intensity varies only slightly over this length. Figure 17(iii) shows the soft X-ray image during the unstable ($m = 0$ instability) phase. The intensity shows well defined maxima along the z axis. A clear peak in the intensity distribution can be seen near the face of the inner electrode. The X-ray intensity distribution during the plasma disruption phase is shown in Figure 17(iv). There are two distinct emission

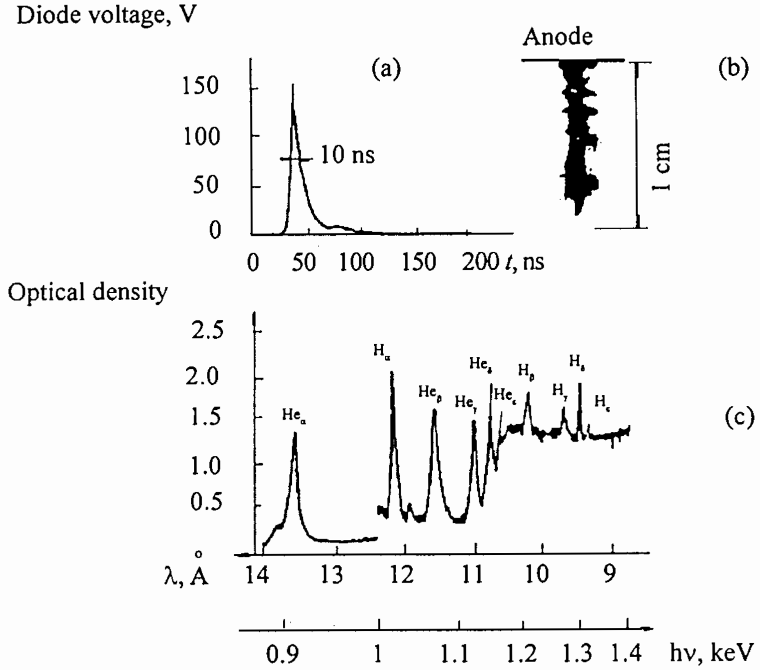

Figure 18. Characteristics of the soft X-ray emission of a neon discharge [164]. (a) Emission rate detected by a fast plastic scintillator coupled to a fast visible photodiode. (b) Time-integrated image of the soft X-ray source from a pinhole camera ($100\,\mu$m pinhole and $12.5\,\mu$m Be filter). (c) Neon X-ray emission spectrum obtained from two different shots by a flat crystal spectrograph.

regions recorded by the (a) channel. A strongly emitting zone can be seen near the inner electrode face (probably coming from electrode material). A second, highly irregular, structure (emitting X-rays at 0.4–0.8 nm) is situated between 7 and 10 mm from the inner electrode face and extends radially over 5–6 mm.

Figure 18 presents the temporal, spatial, and spectral characteristics of the soft X-ray emission for a discharge in a slightly heavier gas (neon) produced in a medium-energy plasma focus [164]. Figure 18(c) shows that the spectral emission features lines of H- and He-like neon ions, as well as a distinct contribution from the He-like ion free–bound emission.

In a medium-energy (28 kJ, 800 kA discharge current), high-voltage (60 kV) plasma focus working with hydrogen–argon gas mixtures [154], two periods of X-ray emission were identified. The first began at the first pinch compression; the second was observed after the break-up of the plasma column, and originated from a small region on axis at distances greater than 15 mm from the anode. Simultaneous temporally and spatially resolved soft X-ray streak camera measurements revealed the truly dynamic nature of the plasma focus X-ray source. Subsequent experiments using the same device have shown that the addition of a heavier gas (krypton) to the deuterium–argon mixture strongly affects the argon ion emission spectrum: 2% (volume) Kr leads to a reduction of the Ar XVII line intensities below the level of a neighboring quasi-continuum peak [165].

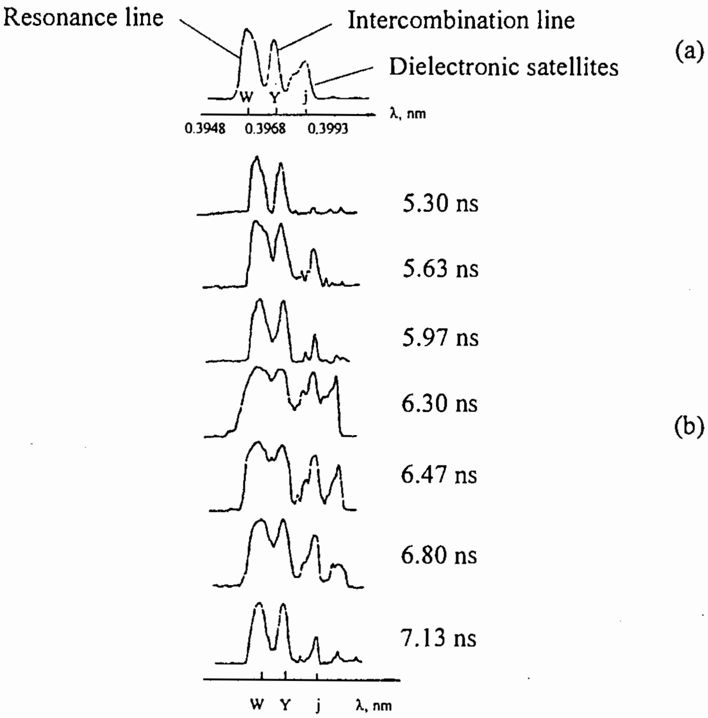

Figure 19. Line spectrum of He-like (resonance and intercombination lines) and Li-like (dielectronic satellites) argon ions. (a) time-integrated and (b) time-resolved spectra [155].

The highly transient nature of the plasma focus process, in general, and of the associated X-ray phenomena, in particular, can be further illustrated by the time dependence of the line spectrum in deuterium-argon mixtures at energies around 3 keV. Figure 19 presents the He-like ion Ar XVII resonance and intercombination lines and Li-like Ar XVI satellite line structure emitted by a deuterium–argon plasma-focus discharge for which both time-integrated (a) and time-resolved (b) spectra were recorded [155]. These clearly show that the line spectrum, and especially the dielectronic satellite structure, changes on a sub-nanosecond time scale.

The spatial structure of the soft X-ray source indicated by the time-integrated images [153] changes when going from a pure deuterium discharge (Figure 20(a)) to a discharge using a deuterium–xenon (2% Xe) mixture. When the spectral bandwidth of the recording system is changed (Figure 20(c)), the images of the bright spots become sharp, indicating that the dimensions of the emitting sources are much smaller than those of the pinhole.

The time-integrated spectral distribution of the hard photons emitted by a plasma focus fits a power law spectrum of the form

$$\frac{\mathrm{d}N_{\mathrm{hx}}}{\mathrm{d}E} = AE^{-n} \qquad (E \text{ in keV}) \tag{8.1}$$

where N_{hx} is the hard X-ray flux in photons per cm^2, and A and n are constants. For photon energies in the range $7 < E < 29$ keV, $n \approx 2$ [144], while at higher energies (30–200 keV) [160], a slightly different value $n \approx 2.5$ was fitted to the experimental points. A similar power law spectrum was shown [161] to occur at energies above 100 keV, with n about 4.

The spatial reproducibility of the plasma focus soft X-ray source (time-integrated image) can be quite high: for a neon operated plasma focus, the diameter of the X-ray emitting region was 0.4 mm for a single discharge and 0.9 mm for a series of 30 discharges [166].

8.4. Dependence of the X-ray emission characteristics on plasma-focus operating parameters and regimes

The characteristics of plasma-focus X-ray emission depend strongly on the plasma-focus operating parameters (gas filling composition and pressure, stored energy, plasma current, driver impedance, electrode material and configuration). This dependence makes difficult any comparative analyses of X-ray emission results obtained for different devices, but provides, at the same time, ample means to tune the plasma-focus X-ray output.

The strongest influence on plasma-focus X-ray emission is produced by the gas composition and pressure. For plasma focus devices working with gas mixtures of hydrogen or deuterium with heavier gases, or with pure heavy gas filling, the soft X-ray yield depends on the type and composition of the gas used. It was found [151] that, for hydrogen-rare gas mixtures, the X-ray emission displays clear peaks in terms of the volumetric ratio of the gas mixture. For pure neon gas filling, the energy emitted at 0.85 nm depends on both the gas pressure and the capacitor voltage [166] (Figure 21).

The influence of the gas pressure and composition on the plasma-focus hard X-ray emission exhibits a strong dependence on the hydrogen [68] or deuterium pressure [167]; the optimum pressure for high X-ray yield does not correspond to the optimum neutron yield pressure [168]. The maximum hard X-ray yield was obtained [167] at 2.5 Torr, a pressure lower than that corresponding to the maximum neutron yield, which was obtained at 5 Torr; at this pressure, the X-ray yield was $1:10$ of its maximum value. A study performed on a medium-energy (57.3 kJ), low-voltage (16 kV) plasma focus [168] showed that the hard X-ray yield Y_{hx} displays an obvious dependence on each of the following operating parameters: gas filling pressure (the highest Y_{hx} was obtained at 1 Torr deuterium, and was more than double than the yield at 4 Torr, which was the optimum pressure for maximum neutron yield), fill gas composition (lower Y_{hx} was obtained with pure Ar than with deuterium, and the ratio of the hard-to-soft X-ray yields $Y_{\mathrm{hx}}/Y_{\mathrm{sx}}$ decreased), electrode insert material (lower hard X-ray yields were obtained with a W than with a Ta insert), and vacuum chamber geometry (reducing the distance between inner electrode end and vacuum chamber end wall reduces Y_{hx} and decreases the $Y_{\mathrm{hx}}/Y_{\mathrm{sx}}$ ratio). The effect on the hard X-ray emission of decreasing the gas pressure was considerable [166]: at lower pressures, the intensity increases, the pulse width decreases, and the spectrum is shifted to higher energies, while maintaining its power law ($n = 2$) shape.

One operating regime maximizing the X-ray yield was obtained in a Filippov-type plasma focus [149]. At 100 kJ capacitor bank energy, X-ray yields up to $300\,\mathrm{J}/4\pi$ have been measured at an emission level $\approx 4\,\mathrm{J/cm^2}$ near the anode. The mean photon energy was 300 keV for a tungsten anode. The intensity and hardness of the X-ray emission decreases for lower-Z (and lower boiling point) metals (mean photon energies

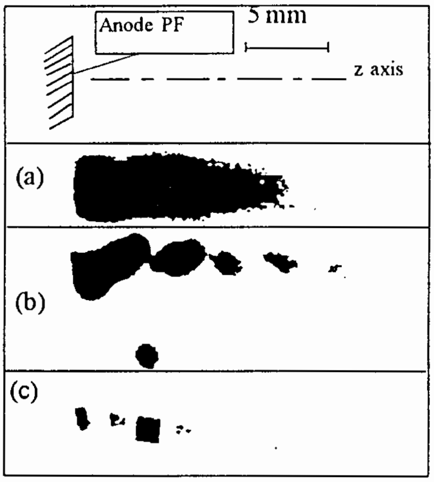

Figure 20. Plasma focus soft X-ray time-integrated images [153]. (a) Pure deuterium at 7 Torr; 0.6 mm pinhole; 9 μm Al filter. (b) D_2 at 6 Torr + 2% Xe; 0.6 mm pinhole; 9 μm Al filter. (c) D_2 at 6 Torr + 2% Xe; 0.5x0.5 mm^2 square pinhole; 0.5 mm Be filter.

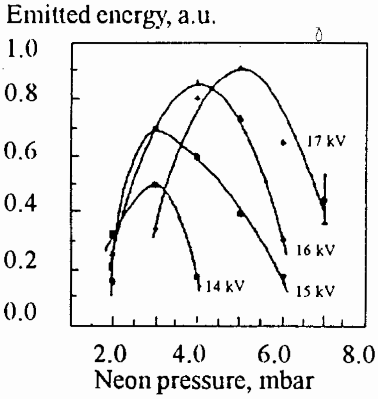

Figure 21. Dependence of the soft X-ray emitted energy on the neon pressure and capacitor charging voltage [166].

were 130 keV for Cu and 70 keV for Al). A very high soft X-ray yield was obtained working with a higher-energy device ($E = 0.9$ MJ) in the same regime with a pure neon gas fill (0.2 Torr) [5]: 120 kJ was emitted in the lines of H-like and He-like neon ions. The soft X-ray yield scaling for this device was $Y_x \propto I^4_{\text{pinch}}$ (similar to the neutron scaling).

Studies of plasma-focus hard X-ray spectra have shown [160] that the quantity A in equation (8.1) depends on the device used, the anode material, and the bank energy; in addition, the spectra were affected by the fact that emission of lower-energy X-rays depended on bank energy, anode geometry, and composition, while the emission of the higher-energy component did not. The polarity of the inner electrode has a strong influence on the X-ray emission: operation with a positive-centre electrode produces up to 50 times more soft X-rays than operation with an electrode with the opposite polarity [4]. Optimization studies have shown that the plasma X-ray yield

Y_x depends on peak current and pinch radius roughly as

$$Y_x \propto \frac{I^4}{r^2} \,. \tag{8.2}$$

This dependence [169] reflects better operation at higher voltages (for constant stored energy). This is similar to the scaling found for Z pinches [170].

8.5. Plasma phenomena revealed by X-ray emission

The plasma focus soft X-ray source usually has an internal structure, which has been revealed by various methods (spectral filtering, addition of heavier gases to the main, hydrogen-isotope gas fill, time resolved recording of the X-ray image). The existence of several regions of intense X-ray emission with very small sizes (0.2 mm), called "hot spots", within a larger region 1.5 to 2.5 mm in size was observed as early as in 1965 [4]. Plasma "beads" emitting strongly at soft X-ray energies and located roughly along the current channel were observed in a Filippov-type plasma focus [171]. They were thought to originate, not from the gas plasma, but from metal vapor ejected from the electrode that was ionized and had undergone a radiative collapse process. A direct indication that the bright spots represented plasma features of high particle density (rather than high temperature) came from CO_2 laser-scattering experiments [107], which indicated the same dimensions for the bright spots as the X-ray pinhole images: approximately 40 microns.

Tiny plasma structures intensely radiating soft X-rays and having elongated shapes are considered to be micropinches, in which the particle distribution is at least related to (if not confined by) the magnetic field (or current density) distribution. Bright soft X-ray sources produced in the KPF–3 installation (100–150 kJ stored energy and 1.5 MA discharge current) [153] operating with deuterium–xenon (2%) mixtures were regarded as micropinches having radial dimensions from 10 microns (lower limit of detection) to 100 microns, with axial sizes at least three times greater. The axial size may be the result of axial motion of the X-ray source.

In the SPEED II high-voltage plasma focus [155] working in an argon gas-puff mode, micropinches were reproducibly produced along the discharge axis; their formation was thought to be favored by small temperatures and relatively high densities. It was found that micropinch generation first starts near the end of the central electrode, and that micropinch lifetimes are from 0.25 to 1 ns. Micropinch-like structures produced in argon with dimensions from 40 to 250 μm were also obtained in krypton and xenon, but not for lower-Z gas filling, such as neon or nitrogen. It was deduced from time-integrated spectra that argon micropinches have mean temperatures and densities of 1.5 keV and $10^{22}\,\mathrm{cm}^{-3}$.

It was initially thought [4] that multiple "hot spots" resembled the $m = 0$ instability of a pinched discharge, and thus might be related to this process. A more likely explanation for the generation of bright X-ray emitting plasma structures invokes radiative collapse phenomenon [157, 158]. Indeed, studies of a bright-hot-spot regime in the DPF–78 plasma focus [154] showed that at least some of these plasma entities were not connected with the development of instabilities; observations made with various high-Z gas mixtures indicated an obvious relation to radiation. The strong influence of radiation processes on the plasma evolution in the plasma-focus pinch phase was distinctly indicated in experiments with neon-seeded deuterium discharges carried out in a 12.5 kJ, 600 kA plasma focus [148]. Radiative cooling was considered to be responsible for the more than tenfold increase in the plasma density. In the DPF–78 device, the addition of a few percent of neon to the deuterium gas filling lead to dramatic changes in the radiative characteristics of the discharge in the pinch configuration as well, resulting in the generation of high-aspect-ratio (length/diameter $\gg 10$) pinches (HARPs), shown clearly and reproducibly in X-ray pinhole camera images and Schlieren pictures [172]. The experimental results obtained on the KPF–3 device [153] noted above were considered by the authors of that study to be consistent with a model of radiative compression that explains the formation of micropinches as a result of both the onset of $m = 0$ instabilities (leading to local plasma displacement) and of intense radiative losses via line emission by multiply charged heavy ions.

Axial filaments extending over the whole pinch length were observed in the POSEIDON and PF–360 plasma-focus devices [24, 172] working in deuterium at pressures of about 5 mbar and 15 mbar, respectively. Soft X-ray pinhole pictures show that the compressed plasma contains several filaments, including one on the axis. The filaments were observed at certain optimum pressures (5 mbar for POSEIDON), appeared 20–30 ns before maximum compression, and existed for 30–40 ns after it. The existence of a filamentary structure in the envelope of the compressed plasma had been previously suggested by soft X-ray spectroscopy and refractometric studies [159]. The influence of the filaments on the pinch properties seemed to be weak. One explanation proposed for the formation of filaments in the plasma-focus pinch [173] suggested that it was the result of current self-pinching due to current–current interaction in accordance with the Biot–Savart law, initiated by microinstabilities associated with electron cyclotron activity.

8.6. Conclusions

The plasma focus produces intense X-ray pulses with photon energies from below 1 keV to over 0.5 MeV, with pulse durations between a few and a few hundred nanoseconds. The integrated energy represents a significant fraction (10–15%) [5] of the electromagnetic energy stored in the plasma-focus driver. The soft X-ray emission generally exhibits two or three periods of emission, corresponding to the stable-pinch, unstable-pinch and pinch-disruption phases. Hard X-rays are usually emitted in a short (a few to a few dozen nanosecond) pulse that results from the interaction of the fast electron beams generated in the pinch region with the anode surface.

The characteristics of the plasma-focus X-ray emission depend in a very complicated way on the plasma-focus operating parameters (gas filling composition and pressure, stored energy, plasma current, driver impedance, electrode configuration) and on the energetic and spatial distributions of the electron and ion populations, with all of these determining the mechanisms involved in the radiation processes. The electromagnetic radiative processes in a plasma focus include not only the (quasi-)equilibrium thermal radiation of macroscopic plasma structures, but also radiation due to electron beams interacting with non-plasma targets (electrodes), and also with periodic electron density structures [150]. The basic emission mechanisms for the "thermal", plasma X-ray component are associated with electron–ion collisions: Bremsstrahlung, recombination, and line radiation. The dominant hard X-ray emission is due to nonthermal high-energy electrons striking the anode. The time-integrated X-ray distribution obeys a power law, and is proportional to E^{-n}, where E is the photon energy and $n = 2$ to 4.

Internal structure of plasma-focus soft X-ray sources has been revealed by various methods (spectral filtering, addition of heavier gases to the main, hydrogen-isotope gas fill, time-resolved recording of the X-ray image). These provide evidence for the existence of intensely radiating small macroscopic entities (called by various authors hot spots [4], micropinches [147, 153, 155], bright spots [147], or plasma beads [171]), as well as well-defined filamentary structures [24, 159]. The lifetimes of bright spots are less than 1 nanosecond, and they have dimensions of a few dozen microns [155].

The measurement of plasma-focus X-ray emission requires methods capable of operating over very wide energies (spectrum) and space and time ranges, with high resolving powers in these ranges. For instance, proper study of the radiative properties of bright spots requires a spectral resolution of 10^4 in the spectral range 0.1–1 nm, together with 0.1 ns temporal and $10\,\mu$m spatial resolutions. Methods and devices meeting such requirements have only recently become available [155].

9. Ion beams

In many plasma-focus experiments, fast deuterons [25, 111, 117, 174–190] have been observed, as well as energetic impurity and admixture ions [183, 185]. Investigation of those ions provides some information about the dynamics of plasma phenomena and mechanisms for ion acceleration. On the other hand, ion emission studies are also of importance for various technological applications of plasma-focus facilities.

9.1. *General characteristics of deuteron beams*

High-energy deuteron beams emitted from plasma-focus discharges with deuterium filling have been investigated in many laboratories. More than 10^{15} deuterons with 1 MeV average energy were observed using deuteron reactions with lithium and the time-of-flight method in a hybrid Filippov–Mather configuration [174]. Using nuclear emulsions in a Filippov-type experiment [190], 10^{13} deuterons per shot were measured. An energy analysis of the fast (> 100 keV) deuterons escaping from plasma-focus discharges was carried out using a magnetic spectrometer and time-of-flight calculations [189]. It was found that the deuteron energy spectrum (>70 keV) extends to above 400 keV, and can be approximated by an exponential function $\exp(-kE_{\rm d})$. The total ion flux from a small 1 kJ plasma-focus discharge was estimated to be about 10^{14}.

Nuclear activation techniques were also used to measure the fluence of high-energy deuterons [186, 188]. Activation measurements with carbon targets indicated that a 76 kJ discharge can generate about 10^{15} deuterons with energies higher than 330 keV. Based on thick-target yields for carbon and aluminum (d, n) reactions, it was estimated that such discharges can create more than 10^{12} deuterons with energies above 5 MeV [188]. Using the foil stack technique [186], it was found that a large 250 kJ plasma-focus facility can generate deuterons with an energy spectrum ranging to about 6 MeV. In many experiments [25, 111, 117, 174, 179–190], ion emission was observed to appear at pressures lower than the pressure for neutron emission, and the maximum ion emission occurs at a pressure that is lower than that at which the highest

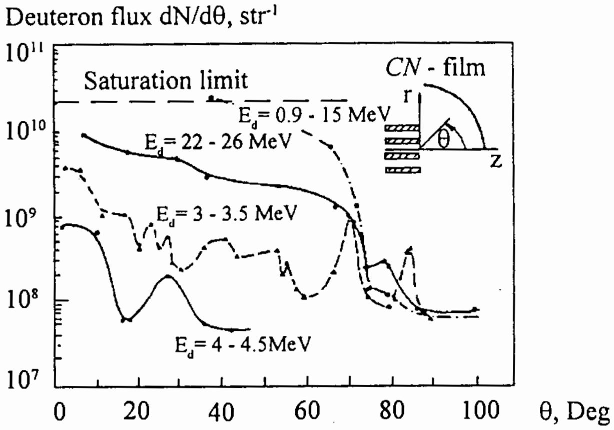

Figure 22. Angular distribution of deuterons emitted from a single 28 kJ plasma-focus discharge [185] performed at p_0=6.7 mbar D_2, Y_n=5.5×10^9.

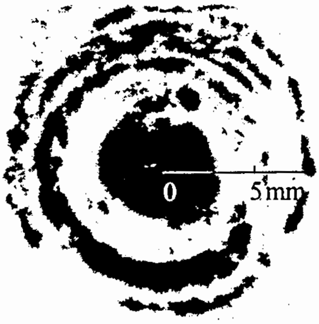

Figure 23. Typical ion beam picture obtained behind a 0.2 mm pinhole placed at z=15 cm from the anode; p_0=6.5 mbar D_2, Y_n=7.9×10^9, deuteron energy 0.9–1.5 MeV.

neutron yield is obtained. At the same time, the deuteron beam angular distribution usually peaks at the z axis, but can show distinct asymmetry.

Measurements with spatial resolution and a rough ion energy analysis were also performed using nuclear track detectors and thin absorption filters placed around the plasma-focus region and behind pinhole diaphragms [181, 185]. It was shown that deuteron beams with energies ranging above 4.5 MeV are emitted, and the angular distribution of these fast ions is strongly anisotropic, as shown in Figure 22. The fine-scale spatial modulation of the ion emission, which appears particularly at higher energies, varies considerably from shot to shot.

On the basis of pictures taken with ion pinhole cameras, it was found that the ion beams emitted primarily within a small solid angle along the z axis can form complex concentric structures, which are composed of numerous spots with sizes smaller than 0.5 mm, as shown in Figure 23. Analysis of ion pinhole pictures taken side-on [185] enabled identification of relatively large (several mm^2) sources emitting deuterons with energies $E_d < 2$ MeV, very small (about 0.2 mm) sources emitting deuterons with energies 2 MeV $< E_d <$ 4.5 MeV, and larger sources emitting impurity ions.

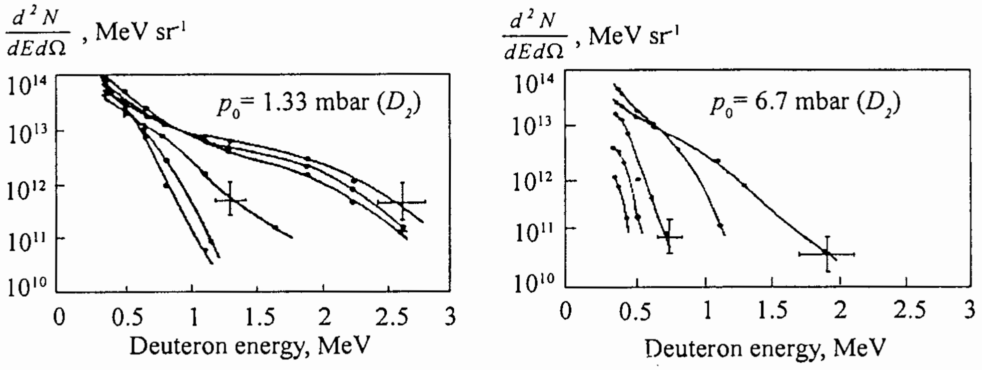

Figure 24. Energy distribution functions of fast deuterons obtained from plasma-focus shots performed with a 56 kJ facility [183].

Ion pinhole measurements performed with various absorption filters [181] showed that the spatial and energetic characteristics of the ion beams (and sources) are generally irreproducible on microscopic scales, but are quite reproducible macroscopically. It was demonstrated that, microbeams with high energies ($E_\mathrm{d} > 300\,\mathrm{keV}$) are usually generated among numerous deuteron beams with more moderate energies ($30\,\mathrm{keV} < E_\mathrm{d} < 300\,\mathrm{keV}$). The number of deuteron microbeams decreases with increase in their energy [181].

A Thomson-type analyzer equipped with a special inlet system (skimmer) adopted for dense plasma studies [183, 185] was used to perform detailed mass and energy analyses for various ions. Deuteron and heavy impurity ion parabolas were registered and the energy distribution functions of fast ($E_\mathrm{d} > 350\,\mathrm{keV}$) deuterons were determined, as shown in Figure 24. The deuteron energy spectrum can be approximated by an exponential function $\exp(-kE_\mathrm{d})$, where $k = 2\,\mathrm{MeV}^{-1}$ for low-energy deuterons and $k = 4$–$8\,\mathrm{MeV}^{-1}$ for high-energy deuterons. With regard to low-energy deuterons, we must take into account that there is considerable attenuation of ions in a dense plasma, as well as in the surrounding gas [181]. Therefore, the energy spectrum below 100 keV must be treated with caution.

Energy spectra of ions with energies down to about 20 keV were measured using a combined time-of-flight and electrostatic-deflection method in a 10 kJ plasma-focus device [180, 184]. The experimental data were analyzed taking into account charge-exchange and energy-loss processes, and it was concluded that the medium-energy (50–100 keV) deuterons make the major contribution to the neutron yield.

The total number of fast deuterons (with energies above 0.5 MeV) emitted from a 60 kJ plasma-focus discharge exceeded 10^{12}, and the total energy contained in the deuteron beams was estimated to be 0.2–0.8 J [183]. This indicated that plasma-focus discharges generate a large number of lower-energy deuterons (< 350 keV), which predominantly contribute to the neutron production.

In some plasma-focus experiments, the energy spectra of protons originating from the primary filling were measured. Such spectra (in the energy range from about 70 keV to above 200 keV) can be approximated by the function $E^{-\alpha}$, where α varies from 2 to 3.5 [177].

In order to carry out time-resolved deuteron beam measurements, a Thomson analyzer was equipped with miniature scintillation detectors [25]. Single deuteron pulses with minimum FWHM < 8 ns (the rise and fall time of the detection system)

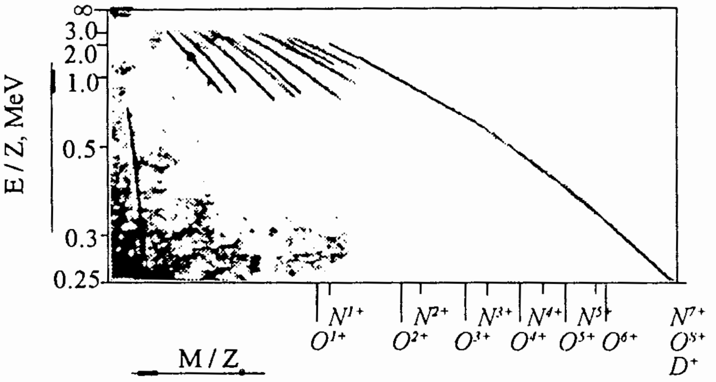

Figure 25. Ion mass spectrogram obtained with a Thomson-type analyzer for a single 56 kJ plasma-focus discharge performed at p_0=4.6 mbar D_2, with Y_n=5.0×10^9.

were registered with a small entrance aperture, revealing a multi-spike structure. The time delays of these deuteron pulses relative to the X-ray signals were consistent with their time-of-flight values, and the time jitter was smaller than 5 ns. Ion measurements carried out with a larger aperture showed longer ion pulses with a complex structure with many ion spikes, probably emitted by different micro-sources located on- and off-axis.

In some plasma-focus experiments, as described for instance in [179] or [182], correlations of hard X-rays, fast electron beams, medium-energy ions, and fusion neutrons were investigated. The maxima of some deuteron pulses coincided with the neutron yield, but were usually delayed by about 20 ns relative to the hard X-rays. In this type of analysis, we must take into account differences in the locations of local sources and in the times-of-flight of the species considered. The general characteristics of the deuteron beam emission from plasma-focus discharges have been confirmed by many experiments [25, 117, 175–185].

9.2. Impurity and admixture ion beams

The acceleration and emission of heavy impurity ions in plasma-focus facilities have been observed experimentally in both Filippov-type [191] and Mather-type facilities [185]. The impurity ions were studied by analyzing micro-craters registered in nuclear track detectors irradiated in pinhole cameras [185] and by using Thomson analyzers [183]. In typical ion mass spectrograms, several parabolas, assigned to different ion species, are usually seen, as shown in Figure 25. All ions detected, except for deuterons, are impurities of the deuterium plasma. Impurity protons can also be registered with more sensitive CR–39 plastic films. Impurity ions with the same M/Z_e ratio, e.g., C^{3+} and O^{4+}, cannot be separated. The deuterons can, however, be discerned from C^{6+}, N^{7+}, and O^{8+} impurity ions registered in track detectors, since the diameter of the deuteron-induced craters is considerably different from those for these other species.

The amount of impurities changes from shot to shot, but on average the percentage of the impurity ions corresponds approximately to the percentage of impurities introduced by leaks, vacuum oil vapors, and deuterium gas filling [183]. Detailed analyses of the Thomson parabolas enable determination of the energy spectra of

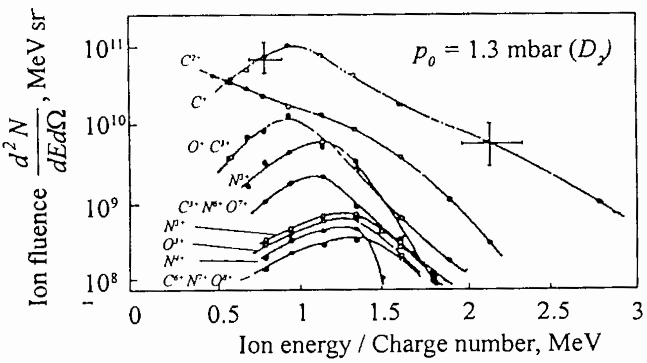

Figure 26. Energy distributions of heavy impurity ions generated by a 56 kJ plasma-focus discharge [183].

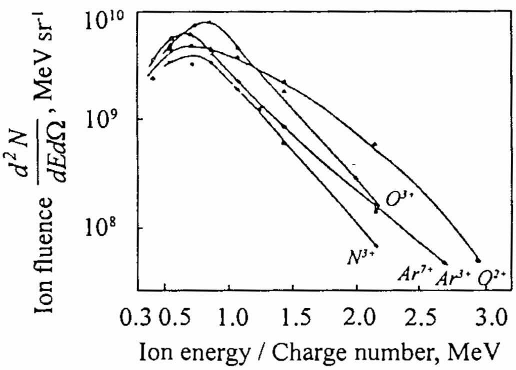

Figure 27. Energy distribution of heavy admixture and impurity ions from a 56 kJ plasma-focus facility [183] operated at p_0=4 mbar (D_2+1%Ar admixture).

different impurity ions, as shown in Figure 26. The corresponding curves can be described by an exponential rise and exponential decay, with the maximum ranging from E_i/Z = 0.8–1.3 MeV. The rise and decay coefficients are 3 to 6 MeV^{-1} and −2.5 to −5 MeV^{-1}, respectively. In other experiments [184], highly ionized copper ions were also observed.

For highly ionized species ($Z > 4$), the maximum E_i/Z ratio is about 1.8 MeV, while it reaches 2–2.8 MeV for lower-ionized impurities ($Z < 4$) [183]. Taking into account the fact that the ions are emitted from submillimeter sources, local electrical fields can reach values of the order of 50 MV/cm.

For some purposes, plasma-focus discharges can also be performed with special gas admixtures. Ion measurements carried out for plasma-focus shots with argon admixtures (0.5–4.5 volume percent) have shown that it is possible to obtain heavy-ion parabolas corresponding to all the ionized species from Ar^+ to Ar^{7+}. The energy spectra for various argon ions are similar to those for other impurities [183], as shown in Figure 27. It has been found that a 50 kJ plasma-focus discharge can emit about 5×10^{10} argon ions per steradian in the energy range 0.5–14 MeV.

Mechanisms for ion acceleration and the formation of intense ion beams are not yet well understood. Since this review is intended to be devoted to well-established experimental facts, theoretical analyses and critical judgments concerning different physical models falls outside its scope. Note, however, that the most commonly invoked mechanisms are based on interactions of the strong electrical fields that can result from local constrictions of the plasma column, due to the development of magnetohydrodynamic instabilities [192, 193] or the degradation of plasma conductivity by strong turbulence [103, 194, 195]. Other proposed models assume collective ion acceleration [196], wave particle interactions [197], or other processes [198, 199]. Ion-acceleration mechanisms connected with phenomena occurring at the anode and connected with the development of the $m = 0$ instability have also been considered [200]. Another model considers multiple reflections from the magnetic piston layer [201]; however, the most popular models assume the formation of a plasma diode [202].

None of the models noted above can explain all the characteristics of ion-beam emission, although some qualitative conclusions are in good agreement with the experimental data. Note also that the motion of medium energy deuterons from 20 to 200 keV is well described by the so-called Gyrating Particle Model [203], which can also explain the neutron generation (see next chapter).

9.3. Conclusions

Studies of the ion-beam emission from plasma-focus discharges can be summarized as follows.

(1) Plasma-focus facilities can be considered as powerful ion-beam generators [187, 188]. Fast deuteron beams (200 keV), as well as impurity and admixture ions, are emitted in a wide solid angle (about 60° around the z axis), and their energy spectra range to above 10 MeV and show strong spatial modulation [183, 188].

(2) The total yield of ions reaches 10^{10}–$10^{14}\,\mathrm{sr}^{-1}$, and depends on energetics and other experimental conditions, e.g., the initial pressure [181, 189]. Higher ion yields are usually observed at pressures lower than those corresponding to the highest neutron yields.

(3) Medium energy (20–100 keV) deuterons with axial and radial velocity components are responsible for the largest part of the neutron yield in fusion reactions [184, 203].

(4) Fast ions are emitted from many point-like (submillimeter) sources [25, 181, 185], primarily in the form of narrow microbeams with durations of 2–8 ns [25, 187]. These can form intense bunches whose total power reaches 10^{11}–10^{12} W [111, 187].

(5) Heavy impurity and admixture ions can be effectively accelerated in plasma-focus discharges to energies up to 15 MeV, and can form ion clusters [176, 181, 183]. Note that, in general, the observed ion energy spectrum extends to higher values than the fast-electron spectrum, and the ion generation efficiency ranges from 0.001 tol 0.1 percent.

We conclude that future ion beams studies should be concentrated on:

(1) further investigation of correlations between ion-beam emission and other plasma phenomena;

(2) verification and further development of existing theoretical models;

(3) further tests aimed at optimizing the emission of various ion species, including heavy admixture ions.

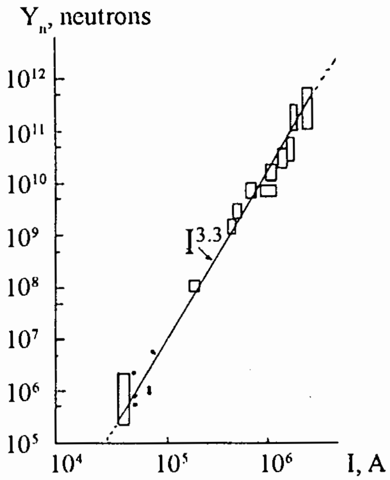

Figure 28. Neutron yield Y_n as a function of pinch discharge current I_p.

10. Fusion products: neutrons and protons

10.1. Fusion yield

Since the operation of the first plasma-focus devices in the late 1950s, their neutron emission has fascinated scientists, due to its unexpected high intensity and characteristic features. Fusion reactions take place in a limited volume in front of the inner electrode during the pinch phase. The neutron yield Y_n scales roughly proportionally to the square of the input (bank) energy W_0. From measurements done in a large range of pinch currents I_p, an experimental scaling law was deduced [204]:

$$Y_n \propto I_p^{3.3}$$

as can be seen in Figure 28. A smaller increase of Y_n was found in a more limited range for high pinch currents.

In comparison to fusion devices based on various principles, the plasma focus is one of the most efficient neutron sources, and combines high neutron fluxes of up to 10^{20} neutrons/s with high fusion energy multiplication Q ($Q =$ fusion energy output/energy input) [205]. The favored scaling of the fusion efficiency (linear rise with the input energy W_0) has its limits at W_0 above several hundred kilojoules, as found experimentally in all large plasma-focus facilities [20]. This observed saturation in the neutron yield is most likely caused by the incorrect formation of a proper plasma sheath due to many reasons (e.g., impurities, sheath instabilities). In contrast, there exists a fundamental threshold for saturation in the neutron yield (not yet reached experimentally); this may become relevant at much higher input energies W_0, due to the inevitable decrease of the role of beam target fusion processes [206].

Experiments with a mixture of deuterium and tritium as the filling gas were made in several laboratories [47, 261]. Maximum yields of 6×10^{12} neutrons (14 MeV) per shot were reported [207]. The neutron yield increase in comparison to that for DD filling ranges from 30 to 80, and is due to the larger fusion cross section.

The original idea that the neutrons have a thermonuclear origin (the moving boiler model) [47], which would be desirable from an energetic point of view, is in contradiction to the experimental data on pinch density, temperature, volume, lifetime, and the measured neutron yield. In many experiments for which experimental data on density, temperature, volume, and lifetime are available, the calculated thermonuclear neutron yield accounts for only around 1% of the measured yield. Although the nature of fusion reaction mechanisms is still under discussion [208–211], the relevance of thermonuclear models is questionable. Experimental data support the dominance of beam target mechanisms. No correlation between the maximum plasma density of the pinch and neutron yield could be found. This suggests that primarily the beam properties and not the target properties determine the fusion yield.

For the characterization of various events during the third (pinch) phase of a plasma-focus discharge, this phase should be divided into four subphases [94] (see Figure 14):

(a) the compression phase ($t < 0$)
(b) the quiescent phase, during which the plasma expands to $r \approx 2r_{\mathrm{min}}$
(c) the instability phase, during which macroinstabilities (predominantly $m = 0$) develop
(d) the late phase, in which the plasma decays after the break-up of the plasma column caused by the instabilities.

Only in large and medium-size ($W > 10\,\mathrm{kJ}$) plasma-focus devices can phases (a) to (d) be clearly discerned. The duration of phases (b + c) varies from about 10 ns (W=10 kJ) to more than 500 ns ($W \approx 500\,\mathrm{kJ}$). In all plasma-focus devices with deuterium filling, neutron emission is observed starting at the beginning of phase (c), whereas mainly in large plasma-focus devices, an additional (first) neutron pulse occurs starting at the end of phase (a). This first neutron pulse can strongly dominate in large and very high-voltage plasma-focus experiments [212, 213]. The plasma-focus phases for POSEIDON and the emission periods for emission of X-rays, electrons, deuterons, and neutrons are shown in Figure 14.

The clear distinction between the two neutron emitting phases in large plasma-focus devices was first found at POSEIDON [214, 215], where the maxima of the two pulses are 100 ns to 200 ns apart and correspond to the ends of phase (a), the compression phase, and phase (c), the instability phase, respectively, as shown in Figure 29. The amplitude of the second pulse increases strongly with the total neutron yield, i.e., with the quality of a shot, whereas the contribution of the first pulse to the yield is approximately constant.

10.2. Neutron anisotropy and spectra

The neutron emission can exhibit a strong forward anisotropy. Anisotropy factors A of 0.8 to 3 have been measured (A = neutron output in axial direction/neutron output in radial direction) [216–218]. The factor A decreases with increasing filling density, and usually increases with higher neutron yield. The high anisotropy is a strong indication of the dominant role of axially directed ion beams in the neutron generation process. Neutron energy [204, 219–221] and flux [216–218, 222] anisotropy measurements provide information about both the energetic and angular characteristics of the ion population responsible for the neutron production.

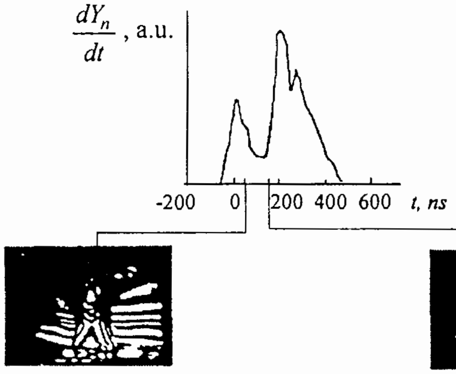

Figure 29. Neutron signal side-on in POSEIDON (280 kJ, 60 kV, 500 Pa D_2, hollow inner electrode, 131 mm diameter) with two interferograms taken at t=16 ns (quiescent phase) and t=154 ns (instability phase).

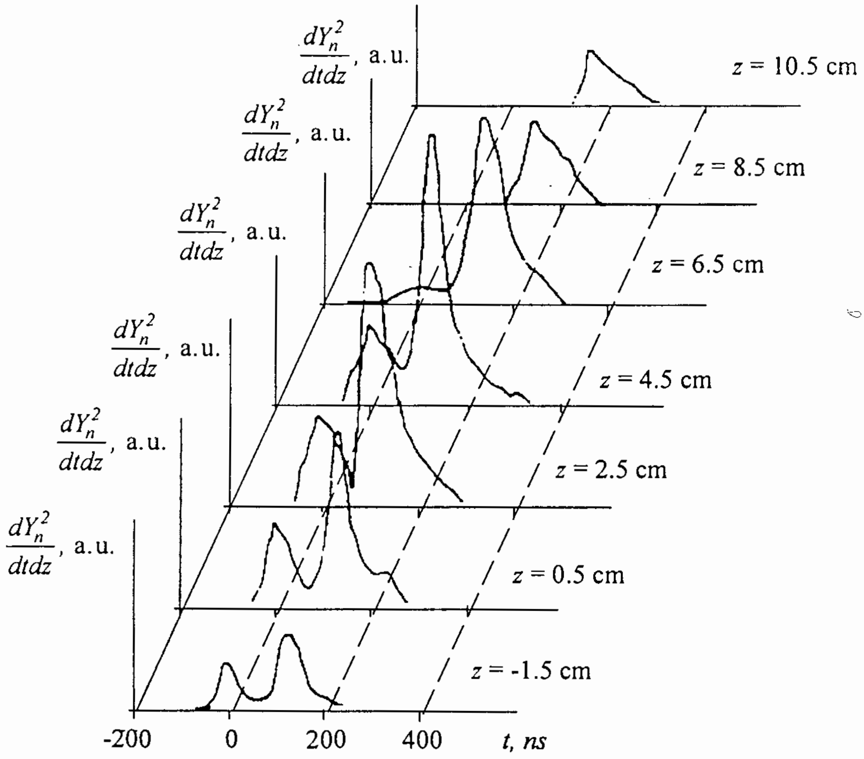

Figure 30. Result of neutron pinhole measurements. Neutron emission spatially resolved in the axial direction (resolution $\Delta z \leq 2$ cm, $\Delta t \leq 20$ ns) in POSEIDON (280 kJ, 60 kV, 500 Pa D_2, Y_n=6.6×10^{10}, hollow inner electrode, 131 mm diameter).

Temporal and spatial neutron source development have been measured using neutron pinholes and a series of detectors [223, 224]. An example of the results of such measurements is shown in Figure 30. The increase of the axial dimension of the neutron source at the time of the second neutron pulse can clearly be seen. The neutron source dimensions coincide roughly with the compressed plasma dimensions [223], i.e., only a small fraction of the fusion reactions occur in the ambient, cold, low-density gas.

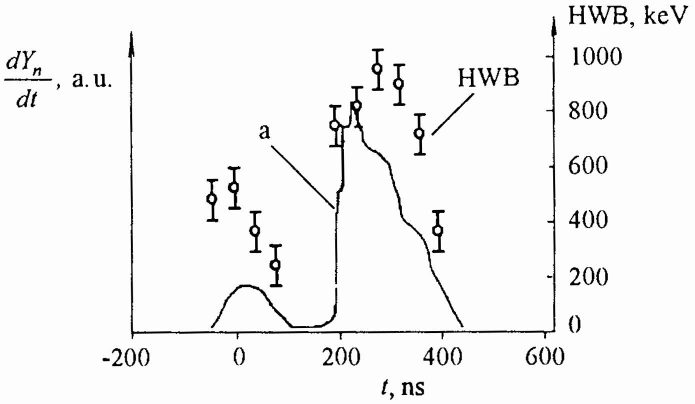

Figure 31. Neutron flux (a) and FWHM (HWB) of the neutron spectra as functions of time, measured during one discharge in POSEIDON (380 kJ, 70 kV, 800 Pa D_2, hollow inner electrode, 208 mm diameter).

The mechanisms for accelerating deuterons to high energies are not yet well understood. Neutron spectra, i.e., experimental data on the energy distribution of the neutrons emitted from a plasma focus [94, 204, 212–218, 221, 223, 224], at least reflect the result of the deuteron acceleration process; in other words, the deuteron spectra can be deduced from the observed neutron spectra. Therefore, a large effort in several laboratories [223, 225–228] has gone into measuring time-resolved neutron spectra. From the theoretical point of view, the problem is finding a solution of the integral equation relating the neutron velocity distribution with the time-dependent neutron flux recorded at various distances from the source [226]. First, an iterative technique was used [225] to process the data obtained with a set of four detectors; it was found that the neutron velocity spectrum shifts towards lower energies during the emission time. Then, a variable separation method was developed for the solution of the integral equation [226]. The application of this method to measurements performed on a low-energy (about 10 kJ) plasma-focus device indicated that the average neutron energy decreases during the emission time [227]. The neutron energy distributions have also been calculated using a computer-assisted Laplace transformation procedure [223, 228]. This method enables the determination of the time-resolved spectra from eight time-of-flight signals taken at various (optimized) distances from the neutron source. An example of results obtained is shown in Figure 31 [94], which plots the neutron signal and FWHM of the neutron spectra as functions of time. Assuming that the FWHM corresponds to a quasi-temperature T_i^* in the fast deuteron distribution function, this quasi-temperature T_i^* is lower in the first neutron pulse (15 keV to 80 keV) than in the second neutron pulse (up to 120 keV). Deuteron acceleration begins 100 ns to 50 ns before the maximum compression, and may be the result of ion reflection at the radially collapsing plasma sheath [229] and/or of electric fields that are generated inductively and by the onset of anomalous resistivity. A decrease in the FWHM of the neutron spectra is observed during the first and second neutron pulses; this can be explained by relaxation in the deuteron distribution function. It seems that there are, generally, two short acceleration periods at the end of the compression phase and in the instability phase. The long-lasting second neutron pulse (200 ns) suggests the existence of a third acceleration period, which may be associated with rapidly decaying magnetic fields in small plasma structures.

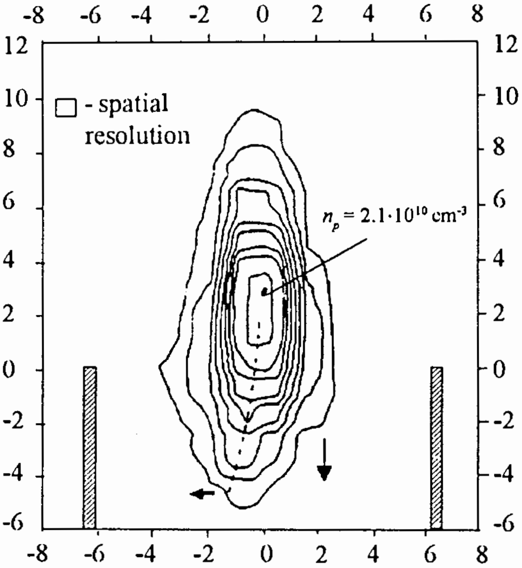

Figure 32. Source of reaction protons with axial and radial distortion (spatial resolution $\Delta x \leq 0.6\,\mathrm{cm}$). The reconstruction is not corrected for the influence of azimuthal (B_θ) and axial (B_z) magnetic fields. Lines of constant proton density on the film are plotted, $n_p = 1.1\times10^{10}\,\mathrm{cm}^{-3}$ is the maximum reaction proton density in the plasma. The arrows indicate the axial and radial shift of the picture, caused by the B_θ and B_z fields, respectively.

10.3. Protons

The measurement of fusion reaction protons can be considered a valuable complementary method to neutron measurements. Since solid-state particle track detectors suited for the registration of single particles, such as CR39 or PM355 [230], have become available, proton measurements have been increasingly applied to fusion devices [94, 231]. Proton measurements can usually be performed with higher spatial and spectral resolution than neutron measurements. The deflection of the protons in electromagnetic fields can be a disadvantage, however, and sets a limit to their applicability in strongly magnetized plasmas. On the other hand, proton diagnostics can be used to determine magnetic field distributions [203, 232].

The source of reaction protons in a plasma focus has been imaged using a pinhole camera. Equidensity contours derived from the track density distribution on a CR39 film using a modified Abel inversion are shown in Figure 32. The reconstruction is not corrected for the influence of azimuthal or axial magnetic fields. An axial magnetic field produced by an azimuthal current (200 kA to 600 kA) of the order of magnitude of the axial current can be deduced from the shift of the density axis (broken line in Figure 32) to the left.

Proton spectra have been measured in eight angular directions with resolution $\Delta E \approx 70\,\mathrm{keV}$. Aluminum foil spectrometers with 54 energy steps and PM355 films for registration were used and calibrated with an ion accelerator. Figure 33 shows proton spectra measured at four different emission angles, together with spectra calculated using the Gyrating Particle Model.

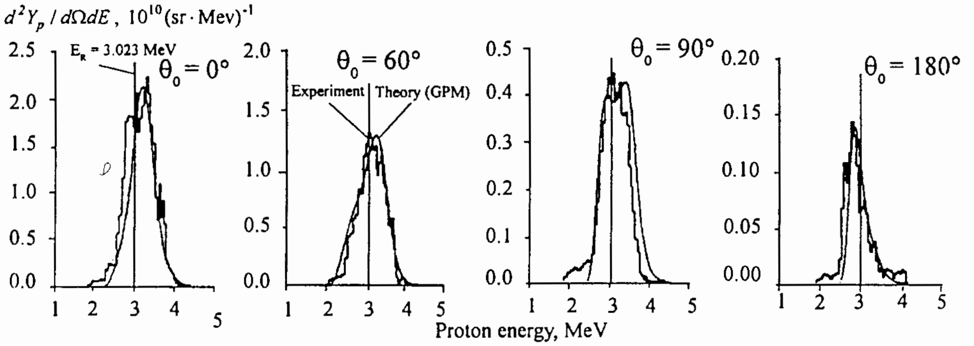

Figure 33. Reaction proton spectra in POSEIDON (280 kJ, 60 kV, 500 Pa D_2). The proton yield is $Y_p = 5.7\times10^{10}$ and the contribution of the first pulse is 34%. For the GPM calculations [203] of the curves, $T_{i1}^* = 75$ keV, $N_{b1} = 5\times10^{16}$, $T_{i2}^* = 200$ keV, $N_{b2} = 3\times10^{14}$, $A_d = 3$, $I_p = 790$ kA.

10.4. Fast ion kinetics and fusion reactions

A beam target model has been applied to describe the fusion processes taking place in both phases of large plasma-focus devices such as POSEIDON. It is assumed [203] that high-energy deuterons (a beam with an assumed energy distribution characterized by a quasi-temperature T_i^*) interacts with a target consisting of the high-density thermal background plasma and the low-density neutral or partially ionized gas near the pinch. Since the initial spectral and directional distributions of the fast deuterons (after the short acceleration process and before their relaxation) are not known, they are chosen arbitrarily for the calculations. In these calculations, in the trajectories of fast ions in the transient structure of the focus pinch and the surrounding gas are determined by a ray tracing code. The results are compared with measurable quantities, such as the time-integrated and spectrally-resolved distributions of the fusion protons and neutrons. The initial distributions of the fast deuterons are found in an iterative process. The deceleration of the fast deuterons by the thermal electrons is taken into account, and fusion collisions of the fast deuterons with the thermal background plasma are treated using a Monte Carlo method [94, 203].

Due to the important role of the gyro-motion of the ions, the model for the ray tracing calculations is called "Gyrating Particle Model" (GPM). The main result of applying the GPM to the POSEIDON plasma focus (280 kJ, 1100 Pa D_2) is plotted in Figure 34. The experimental points (T_i^*) are evaluated from series of reaction proton spectra (see Figure 33). The number of gyrating fast deuterons $N_b = N_{b1} + N_{b2}$ in the first and second fusion pulses was normalized to yield the experimentally observed number of DD reactions in an average yield discharge. N_{b1} and N_{b2} were kept constant, while T_i^* was varied. The agreement between the calculated yield as a function of the quasi-temperature of the fast deuterons T_i^* (assuming that their number is constant) and the T_i^* values determined from the proton spectra strongly suggests that the experimental fusion yield is determined primarily by the quasi-temperature of the fast deuterons T_i^* and not by the number of fast particles. The numbers of fast particles seem to be approximately equal in high- and low-yield discharges. Spatially- and spectrally-resolved measurements of fast deuterons show

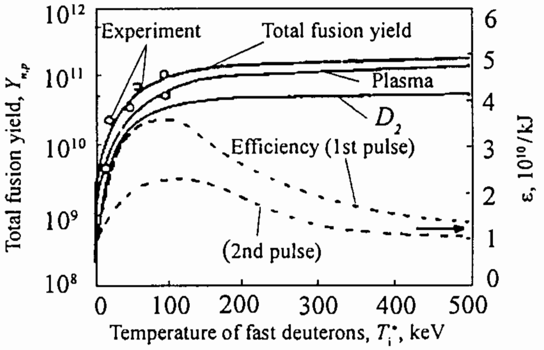

Figure 34. Dependence of the calculated fusion yield $Y_{n,p}$ on the quasi-temperature T_i^* of fast deuterons for POSEIDON. The experimental values (circles) are evaluated from series of reaction proton spectra. Solid lines: "total fusion yield" is the sum of the yields in the "plasma" and in the neutral gas "D_2." Dashed lines: efficiency ε of fusion reactions, i.e., the number of reaction protons divided by the total energy of the fast deuterons (plotted separately for the plasma target conditions during the first and second fusion pulses) [217].

Table 4

Components of thermal and accelerated deuterons in the POSEIDON plasma focus

(I) Quiet phase			
Deuteron component	N_i	T_i, T_i^*, E_d	Y_F
Thermal	1×10^{19} to 1×10^{20}	T_i=200 to 400 eV	1×10^{7} to 1×10^{9}(•)
Fast 1	5×10^{15} to 2×10^{16}	T_i^*=15 to 60 keV	5×10^{9} to 3×10^{10}
(II) Unstable phase			
Thermal	1.5×10^{19} to 5×10^{19}	T_i=0.5 to 1 keV	9×10^{7} to 8×10^{9}(•)
Fast 1	1×10^{16} to 2×10^{17}	T_i^*=40 to 120 keV	1×10^{10} to 1.5×10^{11}
Fast 2	1×10^{12} to 1×10^{14}	T_i^*=200 to 400 keV	1×10^{7} to 1×10^{9}
Fast 3	1×10^{10} to 1×10^{11}	E_d=3 to 6 MeV	1×10^{6} to 1×10^{8}(•)

T_i: Temperature of thermal deuterons
T_i^*: Quasi-temperature of fast deuterons
Y_F: Fusion yield of the deuteron component
N_i: Number of thermal or fast deuterons
E_d: Energy of fast deuterons
•: not verified by experiment

three components [203]. The values of these components for the typical fusion yields of POSEIDON (280 kJ) are listed in Table 4.

Note also that a radically different interpretation has been given by some researchers [210, 233]. This is based on the existence of very small filaments, and consequently large fields, which trap and confine ions in localized regions smaller than 100 μm. These ions would play a dominant role in fusion reactions.

11. Plasma instabilities

Beginning from early studies, the fundamental importance of instabilities for plasma-focus dynamics and hard-radiation output has been unanimously admitted. Macroscopic filamentation during current-sheath formation, hydrodynamical Rayleigh–Taylor instabilities in the $(r,\ z)$ plane at the pinch stage, and micro-instabilities in the current sheath near the time of rupture and in the electron beam–plasma interaction region have been investigated. Attempts to understand plasma-focus acceleration mechanisms have been undertaken together with studies of turbulence, and electron-beam macroscopic instabilities have been observed in plasma-focus experiments. Later, very many experimental and theoretical investigations were undertaken to obtain detailed measurements of the instabilities' nature, wavelengths, growth rates, levels, dumping mechanisms and, in particular, their influence on the plasma-focus dynamics, confinement, acceleration processes, and radiation production.

Various experiments have successively used laser interferometry, shadowgraphy, scattering, beam deviation and Schlieren methods, electric and magnetic measurements (plasma resistivity, voltage spikes, etc), plasma radiation near characteristic plasma frequencies, spectroscopy, and other methods. These experiments have demonstrated that, in a plasma focus, "instability" does not necessarily turn into "turbulence", and "turbulence" does not necessarily induce "abnormal resistivity." The opposite is also true: "abnormal resistivity" is not necessarily the result of plasma micro-instabilities and turbulence, and a plasma turbulence (nonlinear) state does not necessarily appear due to the development of plasma instabilities (linear stages). Instabilities during the breakdown and current-sheath run-down stages have been discussed in the corresponding chapters, so here, we will examine the so-called "turbulence phase" of a plasma focus.

11.1. Micro-instabilities in a current sheath

Accurate theoretical treatment of electrical measurements of the plasma resistivi [illegible] namics and the plasma-density evolution during the current-sheath collapsing p [illegible]ss, together with comparison with the results of numerical simulations, have shown that there is an anomalous resistivity in the focus zone during this period of time. This is probably determined by electron–acoustic and low-hybrid drift instabilities. These instabilities have a very low threshold, $(m/M)^{0.25}\,V_{T_\mathrm{i}} < U = U_\mathrm{thresh} < V_{T_\mathrm{e}}$ and $U_\mathrm{thresh} < V_{T_\mathrm{i}}$, respectively (where U is the current drift velocity, m/M is the ratio of the electron and ion masses, V_{T_e} and V_{T_i} are the mean thermal velocities of the ions and electrons). This should result in an abnormal plasma resistivity, which can be simply estimated:

$$r = (1 + n_\mathrm{eff} t_\mathrm{e})\, r_\mathrm{Col} \tag{11.1}$$

where n_eff is the effective collision frequency, t_e is the time of the electron–ion collisions, and r_Col is the Coulomb resistivity.

It is easy to show that the resistivity becomes abnormal when the linear density is lower than $10^{18}\,\mathrm{cm}^{-1}$ in the region of the current-carrying plasma, and for $N \sim 10^{17}\,\mathrm{cm}^{-1}$, can be 3–4 orders of magnitude lower than the classical value. This estimate is supported both by direct electric measurements and by laser-scattering experiments [103, 126, 234]. Numerical simulations of the current-sheath dynamics after the first compression with an abnormal resistivity of the type indicated above can fit the experimental data [235].

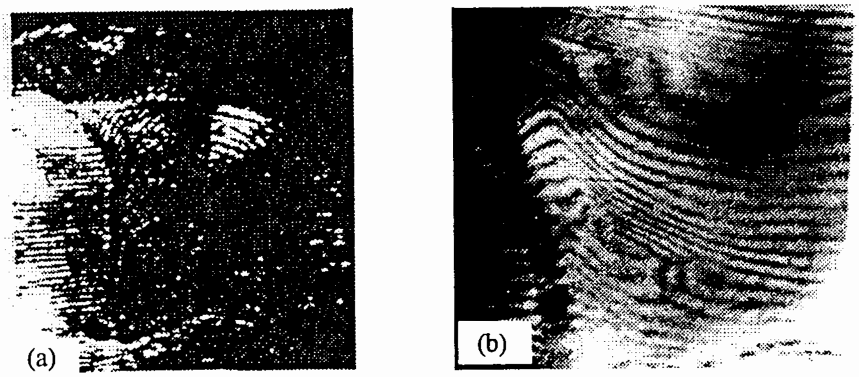

Figure 35. Anomalous laser-beam scattering in the current-sheath skin layer; (a) filling gas is D_2; (b) filling gas is D_2+3% Xe.

Detailed interferometry of the current-sheath skin-layer in the final stage of current-sheath compression and before the current disruption phenomenon [127, 236] has shown the absence of interferometric fringes (see Figure 35), which could not be explained by absorption, classical refraction, and scattering—only by stochastic refraction due to micro-turbulence. Analyses of many similar interferograms and investigations of the scattering angle, degree of coherence, and other parameters [126] of the probe laser beam can give an idea [237]:

of the nature of the turbulence (electron gas fluctuations)

$$p_{\text{ion acoustic}} > p_{\text{photon}} > p_{\text{Langmuir}}\text{—forward scattering} \qquad (11.2)$$

of the size of the turbulence cavities:

$$\frac{1}{2k_{\text{photon}}} < \frac{1}{k_{\text{L}}} \approx \frac{\omega_{\text{pl}}}{v} \approx d_{\text{cavity}} < d_{\text{spatial resolution}} \qquad (11.3)$$

i.e., $0.5\,\mu\text{m} < d < 30\,\mu\text{m}$

of the power of the turbulence occurring after the first compression, using scattering cross-section measurements: $W/nT \sim 0.1$.

In the preceding formulae, p is the quasi-particle momentum; k the wave vector; ω_{pl} the plasma frequency; d the spatial scale; W the Langmuir wave energy density; and v, n, T the electron velocity, density, and temperature, respectively.

11.2. Magnetohydrodynamic instabilities

Plasma-focus installations have several modes of operation ("regimes").

(i) *Regime with one compression.* In this case, immediately after the 10–200 ns confinement time of the pinch, we do [46, 159] or do not [127] have Rayleigh–Taylor instability ($m = 0$ and $m = 1$; see Figure 36(a, b)), which is followed by the explosive breach of the current-sheath boundary due to certain nonlinear phenomena. This time coincides with the very sharp rise time of the hardest X-ray burst and with the slow increase of the second (main) neutron pulse.

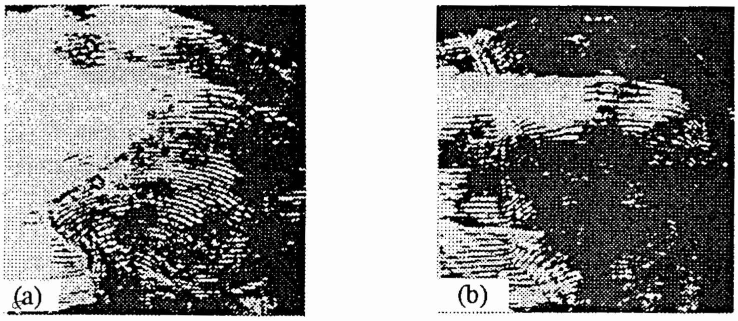

Figure 36. Rayleigh–Taylor instability of a pinch for (a) $m=0$ and (b) $m=1$.

(ii) *Regime with two compressions* or with well-developed (normal for "Mather") Rayleigh–Taylor instabilities. Here, at the end of the instability growth, it is possible to observe the break-up of the plasma column either in the vicinity of (but not in!) the neck (Mather) or near the anode (Filippov).

(iii) *X-ray regime* [128, 238]. Here, the hard X-ray yield increases by an order of magnitude, and the neutron yield is also maximum. The physical picture differs from the previous one in that the break-up of the current sheath takes place near the anode during the run-down phase, before the first compression. This results in the formation of a very short (low-inductive), very fast moving ($10^8\,\mathrm{cm\,s^{-1}}$) current sheath that is compressed near the axis, forming in this manner a short (3 mm), dense (higher than $3 \times 10^{19}\,\mathrm{cm^{-3}}$) pinch. The rupture of the current takes place here immediately after the time of collapse of the current sheath near the axis.

Theoretical treatments of instabilities have taken into account the plasma viscosity as a stabilizing mechanism from the short wavelength limit. Later, it became clear [129, 236] that, when the focus plasma has no impurities (which is normal for a Filippov chamber operating with pure deuterium and sometimes for a Mather focus, operating in a "soft" mode—on the low limit of its matching condition, when the electrode erosion is negligible), anomalous plasma resistivity (>10 times higher than the classical value) takes on a much more important role in comparison with the viscosity, and can promote perfect stabilization of the Rayleigh–Taylor instability:

the Rayleigh–Taylor growth rate (plasma boundary acceleration or magnetic field line curvature) $(gk)^{1/2}$ (1)
the plasma viscosity dumping rate nk^2 (2)
the plasma resistivity dumping rate $\left(k^2\rho\right)/(4\pi)$ (3)

where n is the kinematic viscosity, ρ the resistivity, g the boundary acceleration or $g = V_{T_i}^2/R$, k the instability wave number, and R the boundary curvature. The effective acceleration due to boundary (magnetic field) curvature is a competitive mechanism to normal acceleration for the case of assumed collisionless ions.

The relative contributions of both stabilization mechanisms are determined by the ratio of the hydromagnetic and hydrodynamic Raynolds numbers:

$$N = \frac{R_{\mathrm{HM}}}{R_{\mathrm{HD}}} = \frac{4\pi n}{\rho} \tag{11.4}$$

where ρ is in CGSM units. The smallest possible wavelength in the $(r,\ z)$ plane will be determined in the normal Mather operational case by the viscosity:

$$2\pi g^{-1/2} n^{2/3} \approx 1\,\text{cm} \tag{11.5}$$

and in the typical Filippov case by the abnormal resistivity:

$$\left(\frac{\pi}{2}\right)^{1/3} g^{-3} r^{2/3} \approx 10\,\text{cm} \tag{11.6}$$

where (11.5) is of the order of the experimental value for the Mather, and (11.6) is much higher than the pinch height for the Filippov cases. The latter case, where the plasma current sheath must be very rigid, is supported by the experimental absence of Rayleigh–Taylor instabilities for the first Filippov operational mode with pure deuterium.

During the evolution of well-developed instabilities, in their final stage (or at the end of the confinement period of the focus), the rupture of the pinch and of its current (of the 50–100% that flows through the dense pinch plasma) are occurring. Sometimes (rather seldom) this break-up of the pinch results in the development of $m = 0$ instabilities right up to the end [159, 239]. More often, this rupture of the pinch current does not take place in the neck (where the current density has its maximum) or in the thick part of the pinch (where the magnetic field has its minimum), but rather in the region of the maximum boundary curvature [240], and only in those places where grad N_{e}, $\boldsymbol{k}_H$, and $\boldsymbol{H}$ form the right triple basis. At this time, the third acceleration mechanism is switched on (see next paragraph), but the pinched plasma begins to spread out, decreasing its density in accordance with Bohn's law, which determines the linear confinement time dependence on the magnetic field [241].

In some regimes, primarily when the pinched plasma has many impurities and the anomalous resistivity cannot reach a high level, the evolution of the neck ($m = 0$ mode of the instabilities) can have a special nature, resulting in the radiative collapse and the formation of so-called "hot spots." The basic idea is that the neck of a hydromagnetic sausage instability forms a smaller plasma column. Collapse can proceed when the energy loss due to radiation in a characteristic instability time $t \approx r/v_{\mathrm{A}}$ (v_{A} is the Alfvén speed at the edge of the pinch) exceeds the heat content of the plasma [242]; equivalently, the radiation power per unit length of the plasma must be larger than the energy loss due to expulsion of plasma from the pinch. It is important to realize that the plasma increases the value of $n_{\mathrm{e}}t$ during its compression [243]. We stress that the neck of Z pinches is a very interesting example of a natural singularity, and is the first singularity for which its development follows up an explicit analytical solution. This can give a push to the theory of self-organization of nonlinear systems.

11.3. Acceleration by turbulence

At least three plasma-focus particle acceleration mechanisms can be recognized. The fast particle beams are usually investigated using measurements of plasma-focus hard X-rays, fast electrons and ions, electric fields, etc. The first acceleration takes place in the focus due to a "runaway" process [129, 159], when the critical field $\boldsymbol{E}_{\mathrm{cr}}$ begins to be lower than the electrical field along the pinch column $\boldsymbol{E}_{\mathrm{p}}$ resulting from the increase of its current-sheath anomalous resistivity (redistribution of the applied voltage in the circuit and the IR_{anom} term) and/or from the inductive field $\boldsymbol{v} \times \boldsymbol{B}$:

$$E_{\mathrm{cr}} = 10^{-8} N_{\mathrm{e}} Z^2 T_{\mathrm{e}}^{-1} \approx 10^3\,\mathrm{V/cm} \leq E_{\mathrm{p}} = \frac{U}{h} \approx 3 \times 10^3\,\mathrm{V/cm} \tag{11.7}$$

where U is the voltage across the pinch and h is the pinch height. This process takes place when the cylindrical shock collapses on the axis in the magnetic field-free region, in those parts of the current flowing along the shock front.

Two other acceleration processes are connected with plasma turbulence in a more direct way. These are particle acceleration by strong turbulence [237] and the nonlinear effects of electron magnetohydrodynamics (EMH) [244]. Acceleration by strong turbulent structures is one of the most important particle-acceleration mechanisms in powerful pulsed plasma discharges. Mechanisms for particle acceleration and absorption by cavity structures and the arrest of collapse have been recently discovered; this predicts cavity damping and, consequently, a limit to particle acceleration near the cavity sizes:

$$r \approx (15\text{–}20) d_{\mathrm{e}} \tag{11.8}$$

where d_{e} is the Debye radius. This means that effective particle acceleration corresponds to the velocities:

$$V \approx (15\text{–}20) V_{T_{\mathrm{e}}} \tag{11.9}$$

where $V_{T_{\mathrm{e}}}$ is the thermal electron velocity; i.e., the energy of the accelerated particles should be of order:

$$(15\text{–}20)^2 T_{\mathrm{e}} \approx (300\text{–}400) T_{\mathrm{e}}\,. \tag{11.10}$$

Theory predicts a broad spectrum, and is also able to predict the fast particle distribution. The process of acceleration should be very fast, with a time scale:

$$t\omega_{\mathrm{pl}} \approx 10^3 \tag{11.11}$$

which for plasma focus means $t < 1\,\mathrm{ns}$. The acceleration happens at the last stage of collapse of the structure, although different structures can collapse independently at different times. The acceleration should be accompanied by bursts of emission at local electron plasma frequencies.

Time-resolved hard X-ray spectral measurements together with direct electron energy spectral investigations and interferometric measurements [132] have shown the appearance of two different groups of fast electrons after the compression phase:

(1) with energy near 150 keV and pulse duration of the order of 100 ns and
(2) with electron energy above 600 keV with a very sharp rise time (smaller than 1 ns) and pulse duration near 20 ns (Figure 37).

The first group of electrons has a rather broad energy spectrum and many similar features with the acceleration mechanism based on strong turbulence; the second group of electrons appear rather monochromatic, but with their energy changing in time. The time of the appearance of the faster group coincides with the explosive break-up of the pinch boundary. Experiments have included the treatment of pinhole pictures in hard X-rays, X-ray spectra, anomalous laser-beam scattering, electron spectra, etc, all with good time and spatial resolution.

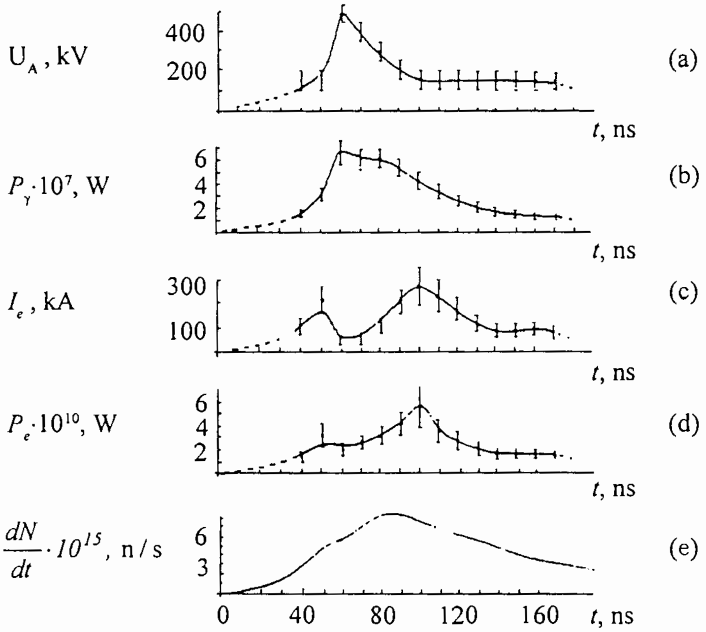

Figure 37. Evolution in time: (a) virtual voltage across the plasma diode; (b) X-ray power; (c) electron-beam current; (d) electron-beam power; (e) neutron intensity.

The third (and most effective!) acceleration mechanism can be interpreted in terms of the nonlinear electron magnetohydrodynamics [244]. As the magnetic field penetrates the pinch at the moment of current rupture with a velocity (measured by multi-frame interferometry) of the order of the Alfvén velocity, convective transfer occurs, rather than a diffusion process. The realization of the conditions for EMH requires:

- small spatial scales ($a < c/\omega_{\mathrm{pl,i}}$, which means for a pinch $Ne^2/AMc^2 < 1$, where N is the number of particles in the cross section)
- short characteristic times (neglecting the ion movement)
- high current drift velocities ($U_{\mathrm{d}} \gg V_{\mathrm{i}}$).

All of these requirements are satisfied in the current-sheath skin layer during the so-called "X-ray pause", which takes place after the first compression. In addition, we need a violation of the Bennett equilibrium for the initiation of EMH effects. This occurs due to the rapid cooling of the plasma by impurity ionization and luminescence, which results in a sharp increase of the ratio of the drift and thermal velocities (the current and pinch diameter are not changed).

Consequently, the overall picture is as follows. After the pinch magnetohydrodynamic compression, heating, and impurity ionization due to Joule heating, as well as ion–ion impacts (shock wave heating and adiabatic compression), the electrons begin to play the major role in the processes. They successively:

(1) sharply cool the pinch, decreasing the electron pressure via impurity ionization and/or radiation;
(2) switch on a whole "bouquet" of micro-instabilities, such as Bunemann, two-

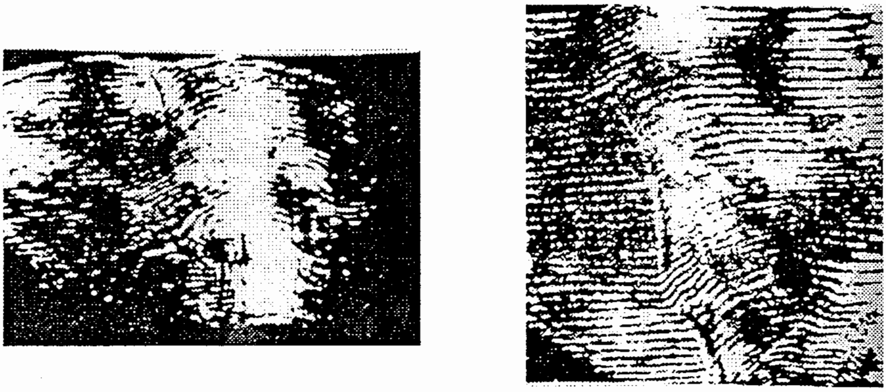

Figure 38. Two examples of the disruption phenomenon.

stream, ion-acoustic, etc, since the current drift velocity remains constant;

(3) create anomalous resistivity, which is determined, not by the instability with the lowest threshold, but by the instability with the highest growth rate;

(4) due to (1) and (3), violate the Bennett equilibrium.

Later, there is a rapid (convective) magnetic field penetration into the plasma, and the "field" EMH resistivity is

$$R = 15\frac{v}{c}\ (\Omega) \tag{11.12}$$

where the drift velocity $v = I/\pi r^2 ne$ and c is the speed of light.

The disappearance of a sharp boundary between plasma and magnetic field is situated in the place, where density gradient, magnetic nonlinear wave vector and magnetic field construct the right triple vector basis (Figure 38) as predicted by theory. The magnitude of the pinch resistivity is in agreement with the data of the table of Section 6.

It is now necessary to discuss the problem of instabilities in the focus, associated with the state of the rare residual plasma surrounding the pinch. The main problem is the following: why does this plasma not take on itself the whole current from the pinch, when its impedance (both inductive or abnormally resistive) increases to extremely high values? One possibility [245] is that this behavior is connected with the fact that this residual plasma is in a turbulent state, and that its anomalous resistivity is dynamic, and is at any time equal to the pinch impedance. These factors probably determine the percentage of lost current, forming a third type of electrical insulation (like vacuum and magnetic insulation).

Indeed, interferometric measurements can be used to obtain the electron density of this rare plasma ($<10^{14}\,\mathrm{cm}^{-3}$), so that it is easy to show that the current velocity is of order V_{T_e}. This means that the drift-dissipative, Bunemann, ion-acoustic and other instabilities should develop in this residual plasma. This turbulence has been investigated experimentally [103, 234] using electric and laser-scattering methods. The importance of the residual plasma state is also connected with the magneto-hydrodynamic stability of the pinch neck.

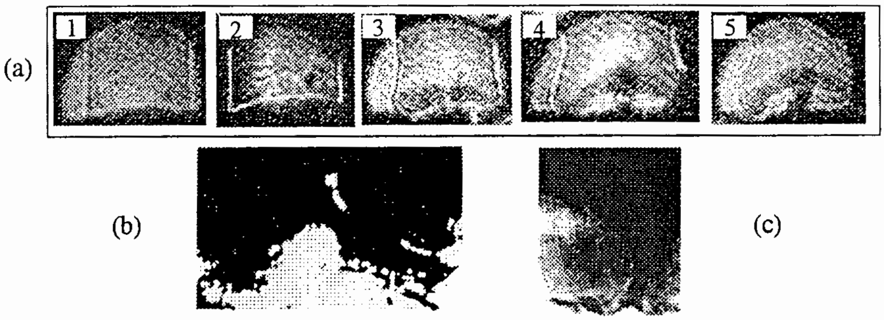

Figure 39. Electron-beam dynamics: (a) five-frame shadowgraphy ($\tau \approx 1$ ns; $\Delta \approx 20$ ns) of the beam self-focusing; (b) filamentation (Weibel instability); (c) hose instability.

11.4. Electron-beam instabilities

Turning to the problems of the relativistic electron-beam dynamics inside the pinch, we should stress that, absolute measurements of the hard X-ray yield and certain other factors (see below) indicate that this relativistic electron beam can exceed the Alfvén current by two orders of magnitude. Outside the acceleration zone, during propagation through the plasma to the focus anode (in the drift space), the relativistic electron beam is subject to self-focusing by its own magnetic field. This occurs due to the imperfect compensation of the free-streaming relativistic electron-beam current by the collisional back-current, and also due to some distortions (Figure 39(a, b, c)).

It is known that during its propagation, the relativistic electron beam can undergo various macroscopic instabilities. In the pinch phase (usually during the final stage), the relativistic electron beam can be divided into several filaments (Weibel instability [246]) and distorted by the "hose" instability [115]. The wavelength and growth rate of the hose instability $\left(k_z \approx 2\text{–}3\,\mathrm{cm}^{-1},\ \Im\omega < 5 \times 10^7\,\mathrm{s}^{-1}\right)$ indicated by five-frame shadowgraphy and interferometric measurements [28] can provide a lower limit for the beam current: $I_{\mathrm{REB}} > \frac{1}{3} I_{\mathrm{current}}$. The proof of this statement is provided by theoretical formulae, as well as absolute hard X-ray yield measurements and certain other direct and indirect evidence, which can be found in the literature.

However, here, we should stress that absolute hard X-ray measurements give a lower limit for the relativistic electron-beam efficiency, since the beam heats the anode plasma during its interaction with the anode, and at some point the interaction becomes non-classical. As a result of this process, the role of the impact parameter (which is small for binary collisions and, thus, delivers the hard X-ray radiation) begins to be played by collective plasma parameters—the Debye length, strong turbulence cavities, etc—which have much larger dimensions, so that the main part of the luminescence of this interaction is in the infrared, near plasma frequencies [135].

Let us examine the role of anomalous electron-beam relaxation in the plasma near the anode, which takes place in the transient plasma-focus regime, in the framework of the first neutron production model (the "shock wave heating" model). As can be seen from the interferograms, after the self-focusing of the relativistic electron beam, the hard X-ray pulse decreases severalfold, while the beam channel continues to be seen in the interferometric pictures over tens of nanoseconds. At this time, it is easy to see the formation of a shock wave and its propagation inside the pinch along the z axis (see Figures 39(a) and 40(a)) [244].

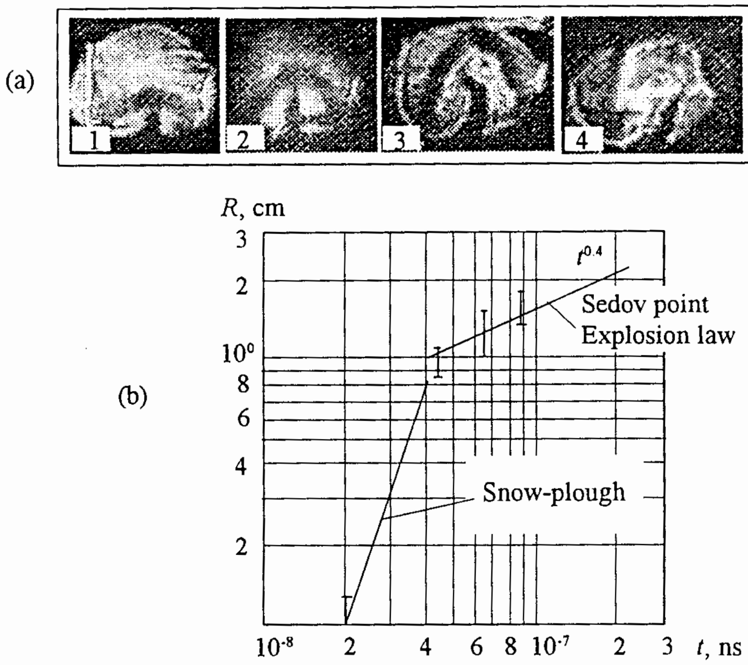

Figure 40. Electron-beam-induced shock-wave propagation inside the pinch (shadowgraphy): (a) five-frame shadow picture (τ=1 ns, $\Delta t_{1\ldots5}$=20 ns); (b) R–t diagram.

Five-frame shadowgraphy and interferometric measurements should make it possible to

- measure directly the mass and velocity of the plasma captured by the shock wave, and to investigate the shock dynamics, together with neutron-pulse generation;
- compare this process with the Sedov formula for a "point explosion";
- estimate the masses of the exploded anode evaporated by the relativistic electron beam and released after the pressure decrease;
- investigate anomalous diagnostic laser-beam scattering in the turbulent plasma in the relativistic electron-beam relaxation zone, and to measure the level of the turbulence, size of the turbulent cells, and certain other turbulence parameters;
- measure the temperature and density distributions of the copper plasma in the turbulent relativistic electron-beam absorbing zone;
- investigate the spectral, time, spatial, and absolute characteristics of the turbulent plasma noise near the plasma frequency for this region [135];
- estimate the relaxation length of the relativistic electron beam in the copper plasma.

All these data suggest the following picture for the anomalous relativistic electron beam–plasma interaction during a transient focus operation regime:

(1) the relativistic electron beam in the plasma focus, after its formation and classical interaction with the cold anode material, is subject to self-focusing, at the same time heating the evaporated copper plasma via back-current heating;

(2) when the condition in this "corona" plasma is suitable for collective processes, beam instabilities develop, resulting in anomalous relativistic electron-beam absorption, a decrease in the hard X-ray pulse, and powerful infrared radiation near the plasma frequency (see Section 11.6.);
(3) the anomalous relativistic electron-beam absorption creates a powerful shock wave, which penetrates the pinch, heats ions, produces neutrons, and explodes the pinch column.

11.5. High electric and magnetic fields

The following possibilities for the creation of high electrical fields in a plasma focus are discussed in the literature:

(1) rupture of the conductivity current due to pinch break-up (neck shrinking to zero radius) and appearance of a displacement current [240, 247, 248];
(2) an inductive field due to the rapid compression of the current sheath [159];
(3) creation of anomalous resistivity in the current sheath and pinch and of a voltage drop in the plasma column near the time of maximum current [127, 159, 234];
(4) creation of a number of strong turbulence cavities with low plasma density and high electric field inside them [236, 237];
(5) EMH effects—here, the high electrical fields are associated with the voltage drop over the EMH resistance and with the inductive field, due to the penetration of magnetic vortices inside the plasma [132, 244];
(6) an inductive $\boldsymbol{E}$ field created by fast reconnection of magnetic field lines, which can take place in the final stage of the pinch evolution, due to tiring instabilities [249, 250], or by magnetic vortex annihilation [251], or by some others mechanisms.

In the first mechanism, the magnetic field energy after the loss of the conductivity current is converted into electromagnetic wave energy, where $E \sim B$. Setting $B \sim 1/r$, it is easy to estimate the maximum voltage during the neck break-up to be near 60 MV [248]. Because this voltage exists for a short time, the ions cannot displace much, so that their energy must be lower, in agreement with the experimental values.

The second mechanism could be responsible for the low-energy part of the fast particle spectrum, due to the insufficient current-sheath velocities. The only exception is a so-called X-ray regime, where the current-sheath velocity can exceed $10^8\,\mathrm{cm\,s^{-1}}$ and electric fields

$$E = \left\langle \frac{|\boldsymbol{v} \times \boldsymbol{B}|}{10^8} \right\rangle = 10^6 \;\; (\mathrm{V\,cm^{-1}})$$

can be reached.

Anomalous plasma resistivity has been reported in many experiments and simulations, so that this mechanism for the creation of high $\boldsymbol{E}$ fields is of considerable importance. Together with the voltage drop over the EMH resistance, these mechanisms can supply $\boldsymbol{E}$ fields for an individual plasma diode of the order of $U = IR_{\mathrm{anom}} \sim 10^6\,(\mathrm{A}) \times 1\,(\Omega) \sim 10^6\,\mathrm{V}$.

The critical questions concerning the fourth mechanism are the level of instability pumping that can be reached in the focus and which mechanism will be the most important for strong turbulence saturation (minimum cavity size). Both these problems are still under investigation both theoretically and experimentally. Some theoretical estimates for the fast particle energy at the same level suggest

$$E_e \approx (15\text{–}20)^2 T_e \approx 1\,(\mathrm{MeV})\,.$$

The most complicated situation experimentally in terms of comparison with theoretical predictions is connected with the last mechanism indicated above (and also the second part of the fifth mechanism). These can provide figures at least an order of magnitude higher, but, as is also the case for the first mechanism, difficulties are presented by the necessity to have temporal and spatial resolutions at the level of 1 to $10\,\mu$m and 1 to 10 ps during a single experiment [252], which is not yet common in plasma-focus research.

Fast-particle energy measurement, which gives $E_e < 1\,\mathrm{MeV}$ and $E_i < 10\,\mathrm{MeV}$, is not an irreproachable method. In reality, due to the presence of the current-carrying residual plasma near the pinch, there is shunting of the pinch, which can be strong enough to draw off the electric field in the space surrounding the pinch. In this case, multiple rotations of particles with large Larmor radii (ions) permit them to acquire energies much higher than the electrical field across the plasma diode. The same multiplicity effect may be present in Fermi mechanisms for particle acceleration due to multiple reflections from the moving magnetic fields of the current sheath or fluctuations, in successive stochastic acceleration by strong turbulence cavities, etc.

Thus, the question of the creation of high $\boldsymbol{E}$ fields in plasma-focus experiments is still open from two points of view: the need for direct measurements of the actual $\boldsymbol{E}$ fields in the plasma (possibly using spectroscopic techniques or electro-optical effects), and the need for searches for ways to organize in a plasma focus the special conditions required to realize the first, fifth, and sixth mechanisms listed above for the creation of high $\boldsymbol{E}$ fields.

Plasma-focus magnetic fields have been investigated via precise current measurements near the chamber axis obtained with a miniature Rogowsky coil [253], Faraday rotation of a ruby laser beam [254], magnetic probes [234, 255], spectroscopic methods based on the Zeeman effect [256], and X-ray luminescence anisotropy [257]. Most of these experiments yield figures near 1 MG, which is supported by estimates performed for the first compression phase taking into account independent density–temperature measurements for the plasma column. Corrections for the current leakage (15–50% leaving the pinch) do not affect the validity of these figures, due to the uncertainties of the field measuring methods. For example [256], taking into account the uncertainty of the compression velocity at the time of a flash of line radiation from a carbon CV $2s^3S\text{–}2p^3P$ multiplet transition, assuming the absence of a π component and allowing for the fact that the half-width of the line profile in the non-magnetized case is smaller than the magnetic splitting, it is possible to determine upper and lower limits for the magnetic field:

$$0.8\,\mathrm{MG} < B_\theta < 2.0\,\mathrm{MG}\,.$$

An important point in focus magnetic field investigations is the detection of the longitudinal component B_z, which (if it exists!) should play an important role in the neutron-production process. This component is predicted to be higher than $10^5\,\mathrm{G}$, based on an analysis of the plasma stream behavior inside the pinch after the action of the laser on the anode surface [128], and has been directly measured in a Faraday rotation experiment [258]. The existence of a strong B_z field (up to 550 kG measured) is of paramount importance to our understanding of the pinch magneto-hydrodynamic stability during the column phase, and of the eventual relaxation of the plasma when the neck finally develops. This field, together with the B_θ component, gives rise to a sheer, which helps to fill the pinch quickly by ions with moderate energy during the neutron-production phase. The presence of this internal longitudinal B_z field has been attributed [241, 259] to the compression by the current sheath ($\sim 10^3$ times in radius, $\sim 10^6$ times in area!) of the Earth's magnetic field, the remaining magnetic fields of the set-up, and the Hall field components initiated at the beginning of discharge vortex formation during the breakdown phase.

The most intriguing question of $\boldsymbol{H}$-field creation is what part of the current flows through the "hot spots"—micro-pinchs—during their maximum compression. It is easy to estimate that, if the entire current flows through a micro-pinch with a diameter of several micrometers, consistent with those measured by current installations, the magnetic fields should be of the order of 10^9 G. Those fields have great importance for fundamental plasma-focus science and also for many applications. Unfortunately, currently only one experiment [257] has been performed, in which the value 160 MG was obtained. It is clearly necessary to develop more refined experimental techniques ($1\,\mu$m–1 ps resolution) to test various possibilities for field creation mechanisms.

11.6. Long wavelength radiation

Important information about the plasma-focus dynamics and turbulence is carried by radiation at infrared and other long wavelengths, emitted by the pinch plasma. Currently this radiation has been investigated at wavelengths from $\lambda \approx 1$ to $15\,\mu$m, near 1 mm, and from 3 to 10 cm [135, 252, 260, 262]. At present, some important parameters of this radiation are available with good temporal and spectral resolution (Figure 41(a, b). Two peaks can be distinguished in the long-wavelength spectrum: at $\lambda \approx 10\,\mu$m ($\omega \approx 1.9 \times 10^{14} s^{-1}$) and $\lambda \approx 5\,\mu$m (2ω), attributed to the first and second harmonics of the plasma frequency, respectively. There is sometimes an intermediate minimum at $\lambda \approx 7\,\mu$m. In different series of discharges, i.e., for a small change of the initial conditions (pressure of the working gas, supply voltage of the plasma focus by a capacitor battery, etc), the maxima frequencies change by 20 to 40%, however each time, the frequencies ω_2 coincide with $2\omega_1$. The infrared pulse has two maxima in time (Figure 42), which nearly coincide with the hard X-ray pulses; the maximum for the second infrared pulse is slightly later (10–20 ns) than the hard X-ray maxima. The first maximum is associated with the electron "escape", when the cylindrical shock wave collides at the axis of the chamber, and the second maximum is associated with the "cutoff" of the main current flowing along the current shell.

In series where the neutron yield is maximum, the intensity of the second harmonic (Figure 41(a)) considerably exceeds the intensity of the first harmonic along the entire discharge. This can be explained if we assume that, in this regime, isotropic plasma turbulence is established, which develops in the region of the anode plasma (where the concentration is $n_e \approx 10^{19}\,\text{cm}^{-3}$).

The radiation at frequency ω is the result of the transformation of Langmuir waves into transverse waves of plasma electrons ($\text{l} + \text{e} = \text{t} + \text{e}$); the radiation at frequency 2ω results from the combination of two Langmuir waves ($\text{l} + \text{l} = \text{t}$) [237]. In the case of anisotropic Langmuir turbulence, the total contribution of the second process can exceed the total contribution of the first, as is observed experimentally.

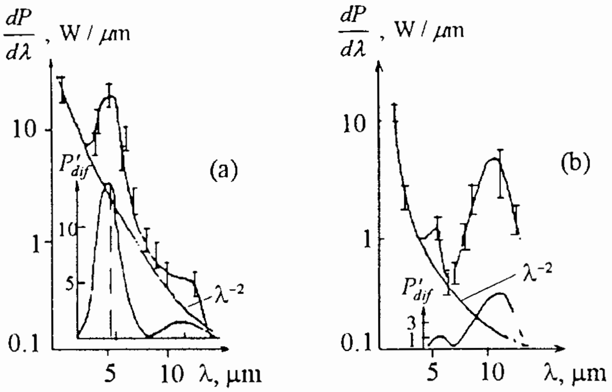

Figure 41. Infrared spectrum of the plasma-focus radiation for series 33 and 34 (a) and series 16 and 17 (b). The insert shows the difference $P'_{\rm dif}$ between the registered spectrum and a blackbody spectrum.

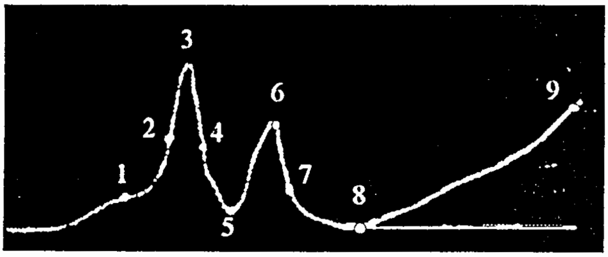

Figure 42. Infrared emission oscillogram (1...9 are points where spectral measurements have been made).

In the second regime—with a low neutron yield, (6 to 9) × 10^7 neutrons per pulse—we have the opposite situation: along the discharge, the first harmonic is more intense than the second (Figure 41(b)). This can be explained by anisotropic plasma turbulence models with $I_{2\omega}/I_\omega < 1$. The power of the epithermal noise in the case of anisotropic turbulence [263] can also be estimated, and the resulting value is comparable with the experimentally measured quantity $I \approx 10\,\mathrm{W}\,\mu\mathrm{m}^{-1}\,\mathrm{sr}^{-1}$. A comparison with the experimental value $I_{2\omega}/I_\omega \approx 10^{-2}$ shows that the characteristic electron energy in the current is below 100 keV in this regime, and the electron temperature is less than 1 keV, consistent with the results of many other independent experiments.

Long-wavelength radiation with a characteristic spatial scale of the order of a centimeter can result from the pinch and electron-beam magneto-hydrodynamic instabilities, plasma-vortex reconstruction due to excitation of the chamber resonator by rapid current rupture, and propagation of the electron beam in a magnetic field corrugated by plasma magnetohydrodynamic instability. The main results [262] of simultaneous measurements of the pulsed emission of hard X-rays (>30 keV), microwaves (wavelengths ≈3 to 10 cm), and DD neutrons in focused deuterium plasmas provide evidence for correlations between these emission processes.

Some results [252, 264] obtained at 30 to 120 GHz ($P \approx 1\,\mathrm{MW}$, $\Delta f/f < 5 \times 10^{-2}$, $\Delta\tau < 600\,\mathrm{ps}$, together with the power of the harmonics), and also the optical spatially modulated self-luminescence of the current sheath and the characteristics of the Cerenkov emission of the electron beam, provide some evidence for picosecond temporal structure of the electron beam, and give some information about the nature of the beam-plasma instabilities in the current sheath. These results and the corresponding analysis suggest that:

(1) Epithermal plasma-focus noise is associated with the interaction of the powerful electron beams generated in plasma-focus devices with the pinch and anode plasmas.
(2) The spectrum of harmonics of this epithermal radiation in the infrared can be explained by models invoking Langmuir turbulence: anisotropic in the case of low neutron yield (spontaneous scattering of Langmuir waves by electrons) and isotropic in the case of high neutron yields (interactions between Langmuir waves).

12. Discussion and conclusion

As shown in the preceding chapters, plasma-focus devices have been and are being extensively investigated by many teams throughout the world, using both small and large installations. Since the costs of setting up experiments is relatively small compared to that for studies of other plasmas, plasma-focus experiments have also been the subject of many theses and academic investigations. This is certainly one of the best diagnosed plasmas (more than a thousand references could be given), and yet many essential facts are still unclear, providing strong motivation for future studies in this field. As in other plasma research, the complexity of the phenomena has proved to be greater than expected, with the consequence that important facts remain to be elucidated. Yet this is a type of fundamental problem, in the sense that it addresses a conceptually simple type of experiment: the interaction of a cylindrical column of current with a plasma.

Let us classify the various results we have presented according to their degree of recognition by the community. The transport of current via the Lorentz force has been clearly measured and, after proper conditioning, efficiencies of more than 80% are standard. The concentration of the sheath toward the axis is accompanied by the emission of neutrons and X-rays and, for many years, there was a large debate about whether the neutrons were emitted by thermal plasma. Since this was, indeed, a most important point, there was a very large effort to make measurements under various types of operation. Now, this issue is settled, in the sense that, whatever device is used, in regimes when large neutron yields are created, the emission is due to the bombardment of accelerated deuterons onto the deuterium ions from the plasma, or even the cold deuterium that fills the chamber. Similarly, large X-ray yields are primarily the result of Bremsstrahlung by accelerated electrons striking the metallic surface of the anode. We stress these facts again to show that considerable progress has been made in plasma-focus studies, compared to the state of thinking in the first decade of research in this field. However, let us also look toward the main issues requiring further investigation.

The sheath structure has been found to differ according to the device used and its polarity, but consistent and systematic studies have not yet been done. This is true partly because the first plasma phase has attracted less interest than the phase in which neutrons are produced, and also because of limitations of probes. In the propagation phase, probes with smaller sizes could be used, and also Faraday rotation observations performed. In this phase, according to some researchers, the sheath is organized in twin vortex structures that store magnetic energy. This would explain the large energy density obtained at concentration, when the magnetic energy is transferred to the accelerated particles, and the subsequent high velocities of the ejected particles. These explanations have met some skepticism, in part because the corresponding observations are difficult; for this reason, we have not described them in detail in this article, however, they certainly should be included in further systematic studies.

One question that can be asked is the influence of the sheath on the emission of particles. For instance, is it possible that differences in the results yielded by two devices used to study the timing of the neutron emission and its characteristics are not due to different physical behavior (e.g., types of instability), but are the result of different initial conditions due to a difference in the formation of the plasma sheath? Systematic study of the relationship between the early sheath structure, its evolution along the gun, and its influence on the beam generation is one example of a study that has not yet been conducted, due to its scope.

It is an important question whether one phenomenon could be responsible for the various forms acquired by the emitted beams. The fact that many Z pinch plasmas have similar gross behavior is a qualitative indication that argues in favor of unity. However, in spite of the attractiveness of this view, there is certainly not enough experimental evidence to support it, and it is one of the most interesting fields of magnetized-plasma research that should be developed.

*

* *

The future research program for the International Centre for Dense Magnetized Plasmas must be discussed and prioritized by the Scientific Advisory Committee. Several possible topics for further study have already been indicated. We note the following three general lines of research.

- One major issue is the detailed physics of the breakdown and propagation phases. This can be studied using refined diagnostic techniques, such as interferometry, Faraday rotation, and laser scattering, which have been used to investigate later phases of the discharge. The aim is to determine the structure of the electric current sheath and how it leads to the generation of fast particles. Such knowledge should eventually make it possible to understand the currently puzzling difference in the behavior of positive and negative polarity operation.
- The generation of beams is strongly anisotropic and time dependent. In recent years, it has been shown experimentally that the tools exist to measure the spatial and time distributions of fast plasma-focus particles. Yet, there have been no simultaneous measurements of the electron and ion characteristics. Such measurements should be obtained together with laser scattering measurements, to determine the nature of density fluctuations. These measurements are clearly possible, but imply the design and construction of new installation chambers, as well as extensive measurement campaigns that are beyond the capabilities of laboratories currently engaged in similar research.

- Another promising topic of research is decoupling the early phases of breakdown and propagation from the phase in which the beams are generated. This concept has been demonstrated practically through the use of a valve that injects a gas in the breakdown volume. It was observed that the energy transfer to the beams can be increased, but no systematic studies have been conducted. This extra degree of freedom in the operation of the experiment makes it possible to attain a larger range of regimes, which may be important in understanding the physics of microinstabilities and beams.

Figure 43. Geographical distribution of plasma-focus research (Argentina, Chile, China, Egypt, France, Georgia, Germany, India, Indonesia, Italy, Japan, Korea, Malaysia, Nigeria, Pakistan, Poland, Romania, Russia, Sierra Leone, Singapore, Taiwan, Thailand, Turkey, United Kingdom, Ukraina, United States of America, Zimbabwe).

References

[1] Petrov P P, Filippov N V, Filippova T I, and Khrabrov V A 1960 in *Plasma Phys. and the Problems of Contr. Thermonuclear Reactions* ed L A Leontovich vol IV (New York: Pergamon) p 198

[2] Filippov N V, Filippova T I, and Vinogradov V P 1962 *Nucl. Fusion Suppl.* 2 577

[3] Mather J W 1964 *Phys. Fluids Suppl.* 7 28

[4] Mather J W 1965 *Phys. Fluids* 8 366

[5] Filippov N V, Vinogradov V P, Krivtsov V A, Myalton V V, Filippova T I, and Khutoretsky I V 1991 in *Proc. IEEE Int. Conf. on Plasma Sci.* vol rep 2C7–8 p 116

[6] Filippov N V, Filippova T I, Kukushkin A B, and Myalton V V in *Proc. Third Int. Conf. on Dense Z-Pinches, Imperial College* (London, 1993) (AIP Conf. Proc. Ser.)

[7] Ware K D, Williams A H, and Clark R W 1973 *Bull. Amer. Ph. Soc.* 18 1364

[8] Bernard A, Garçonnet J P, Jolas A, and de Mascureau J in *Proc. Fourth Int. Topical Conf. on High Power Electron and Ion Beam Research and Technology* (Palaiseau, France, 1981) p 295

[9] Artsimovich L A, Andrianov A M, Bazilevskaya O A, Prokhorov Y G, and Filippov N V 1956 *Sov. J. of Atomic Energy* 1 367

[10] Stephanakis S J, Levine L S, Mosher S, Vitkovitsky I M, and Young F 1972 *Phys. Rev. Lett.* 29 568

[11] Lochte-Holtgreven W 1976 *Atomkernenergie* Bd. 28 3 150

[12] Lee T N 1974 *Astrophys. J.* 190 467

[13] Oppenländer T 1981 Experimentelle Untersuchung des Einflusses hoher Spannungen auf einen Plasmafokus *Doctorate thesis* (Institut für Plasmaforschung der Universität Stuttgart)

[14] Lee S, Chen Y H, Chow S P, Tan B C, Teh H H, and Thong S P 1972 *Int. J. Electronics* 33 85

[15] Decker G, Flemming L, Kaeppeler H J, Oppenländer T, Pross G, Schilling P, Schmidt H, Shakhatre M, and Trunk M 1980 *Plasma Phys.* 22 245

[16] Decker G, Kies W, Mälzig M, van Calker C, and Ziethen G 1986 *Nucl. Instrum. Meth.* A249 477

[17] Burns E J T, Falacy S M, Hill R A, Thacher P D, Koehler H A, Davis B, and Shafer R E 1988 *Phys. Lett.* A 133 144

[18] Borowiecki M and Czekaj S in *Proc. Fourth Int. Workshop on Plasma Focus and Z-Pinch Research* (Warsaw, 1985) p 86

[19] Kies W 1986 *Plasma Phys. Contr. Fusion* 28 1645

[20] Herold H, Jerzykiewicz A, Sadowski M, and Schmidt H 1989 *Nucl. Fusion* 29 1255

[21] Bruzzone H, Kelly H, and Moreno C 1990 *IEEE Trans. on Plasma Sci.* 18 689

[22] Wong C S and Lee S 1985 *J. Appl. Phys.* 57 5102

[23] Hirano K, Nakajima H, Kaneko I, Yamamoto T, and Shimoda K 1990 *Jap. J. Appl. Phys.* 29 779

[24] Sadowski M, Herold H, Schmidt H, and Shakhatre M 1984 *Phys. Lett.* 105A 117

[25] Sadowski M, Schmidt H, and Herold H 1981 *Phys. Lett.* 83A 435

[26] Yamamoto T, Ishii K, and Hirano K 1990 *Jap. J. Appl. Phys.* 29 1841

[27] Bernard A, Coudeville A, Jolas A, Launspach J, and de Mascureau J 1975 *Phys. Fluids* 18 180

[28] Gribkov V A, Nikulin V Ya, Semenov O G, and Sklizkov G V 1978 *Sov. J. Plasma Phys.* 4 589

[29] Choi P, Wong C S, and Herold H 1989 *Laser Part. Beams* 7 763

[30] Neff W, Kromphölz H, Rühl F, Schönbach K, and Herziger G 1980 *Phys. Lett.* 79A 165

[31] Gerdin G, Stygar W, and Venneri F 1981 *J. Appl. Phys.* 52 3269

[32] Steinmetz K, Hübner K, Rager J P, and Robouch B V 1982 *Nucl. Fusion* 22 25

[33] Burtsev V A, Kalinin N V, Kuzmin V A, Litunovsky V N, Ovsyannikov V A, Popitaev A N, and Titov V M in *Proc. Fourth Int. Workshop on Plasma Focus and Z-Pinch Research* (Warsaw, 1985) p 235

[34] Salge J, Braunsberger U, Fell B, Ueno I, and Conrads H 1978 *Nucl. Fusion* **18** 972

[35] Bernard J, Boussinesq J, Morin J, Nazet C, Patou C, and Vedel J 1971 *Phys. Lett.* **35A** 288

[36] Antoni B, Landuré Y, and Nazet C 1976 in *Proc. Int. Conf. on Energy Storage, Compression and Switching* (Torino, 1974) ed W H Bostick, V Nardi, and O Zucker (London and New York: Plenum) p 481

[37] Burenin Y A 1981 *Zh. Prikl. Mekhan. Tekhn. Fiz.* **3** 81

[38] Fowler C M, Caird R S, Erickson D J, Freeman B L, Thomson D B, and Garn W B 1983 in *Proc. IInd Int. Conf. on Energy Storage, Compression and Switching* (Venice, 1978) vol 2 (New York: Plenum) p 19

[39] Freeman B L, Caird R S, Erickson D J, Fowler C M, Garn W B, Kruse H W, King J C, Bartram D E, and Kruse P J 1984 in *Applications of Ultrahigh Magnetic Fields* ed V M Titov and G A Shvetsov (Moscow: Nauka) p 136

[40] Ursu I, Ivascu M, Cotruta D, Dumitrescu–Zoita C, Ludu A, Mandache N, Novac B, Zambreanu V, and Zoita V in *Proc. Twelth European Conf. on Contr. Fusion and Plasma Phys.* (Budapest, 1985) vol 9F part 1 p 558

[41] Novac B, Zambreanu V, and Zoita V in *Proc, Eighth IEEE Pulsed Power Conf.* (San Diego, 1991) p 434

[42] Knoepfel H 1970 *Pulsed high magnetic fields* (Amsterdam: North Holland)

[43] Chatterton P 1978 in *Electrical Breakdown in Gases* ed Meek and Craggs, chapter 2 (New York: Wiley)

[44] Mather J W 1966 in *Plasma Phys. and Contr. Nuclear Fusion Research (Proc. 2nd Int. Conf.)* (Culham, 1965) vol 2 (Vienna: International Atomic Energy Agency) p 389

[45] Bostick W H, Grunberger L, and Prior W 1969 in *Proc. Third European Conf. on Contr. Fusion and Plasma Phys.* (Utrecht, 1969) vol 1 p 120

[46] Filippov N V, Agafonov V I, Belyaeva I F, Vikhrev V V, Gribkov V A, Golubchikov L G, D'yachenko V F, Imshennik V S, Ivanov V D, Krokhin O N, Moiseeva M P, Sklizkov G V, and Filippova T I in *Plasma Phys. and Contr. Nuclear Fusion Research (Proc. 4th Int. Conf.)* (Madison, 1971) vol 1 (Vienna: International Atomic Energy Agency) p 573

[47] Mather J W 1971 in *Methods of Experimental Phys.* (New York: Academic) vol 9 pt B p 187

[48] Nowikowski J and Jankowicz Z in *Proc. Ninth European Conf. on Contr. Fusion and Plasma Phys.* (Oxford, 1979) vol 2 p 542

[49] Donges A, Herziger G, Krompholz H, Rühl F, and Schönbach K 1980 *Phys. Lett.* **76A** 391

[50] Krompholz H, Neff W, Rühl F, Schönbach K, and Herziger G 1980 *Phys. Lett.* **77A** 246

[51] Bruzzone H 1987 in *Proc. Second Latin American Workshop on Plasma Phys. and Contr. Thermonuclear Fusion* (Medellin, 1987) vol 12 p 313 (CIF Series)

[52] Jerzykiewcz A and Brandt S 1989 in *Plasma Phys. and Contr. Nuclear Fusion Research (Proc. 12th Int. Conf.)* (Nice, 1988) vol 2 (Vienna: International Atomic Energy Agency) p 737

[53] Bruzzone H, Vieytes R, and DiLalla N in *Proc. Third Latin American Workshop on Plasma Phys. and Contr. Thermonuclear Fusion* (Santiago de Chile, 1988) vol. Contributed Papers p 7

[54] Bruzzone H and Bagala G in *Proc. Fourth Latin American Workshop on Plasma Phys. and Contr. Thermonuclear Fusion* (Buenos Aires, 1990) vol Contributed Papers p 104

[55] Sadowski M in *Proc. XXth Int. Conf. on the Phys. of Ionized Gases* (Pisa, 1991) vol Invited Papers p 271

[56] Kolesnikov Y A 1968 *Sov. J. Tech. Phys.* **13** 626

[57] Potter D 1971 *Phys. Fluids* **14** 1911

[58] Maxon S and Eddelman J 1978 *Phys. Fluids* **21** 1856

[59] Bazdenkov S V and Vikhrev V V 1975 *Sov. J. Plasma Phys.* **1** 250

[60] Denus S and Scholz M in *Proc. XXth Int. Conf. on the Phys. of Ionized Gases* (Pisa, 1991) vol 6 p 1255

[61] Kvartskhava I F and Zukakishvili G G 1971 in *Plasma Phys. and Contr. Nuclear Fusion Research (Proc. 4th Int. Conf.)* (Madison, 1971) vol 1 (Vienna: International Atomic Energy Agency) p 183

[62] Feugeas J N 1989 *J. Appl. Phys.* **66** 3467

[63] Gribkov V A, Dubrovskiĭ A V, Krasil'nikov V S, Krokhin O N, Mikhailov V I, Nikulin V Ya, and Safronov P P in *Proc. Fourth Latin-American Workshop on Plasma Phys.* (Buenos Aires, 1990) vol 1 p 120

[64] Gribkov V A *et al* 1983 in *Proc. Second Int. Workshop on DPF* (Moscow, 1981) p 64 (*Preprint FIAN, Moscow, 1983*)

[65] Peacock N J, Hobby M G, and Morgan P D 1971 in *Plasma Phys. and Contr. Nuclear Fusion Research (Proc. 4th Int. Conf.)* (Madison, 1971) vol 1 (Vienna: International Atomic Energy Agency) p 537

[66] Baconnet J P, Cesari G, Coudeville A, and Watteau J P in *Proc. IX Int. Conf. on Phenomena in Ionized Gases* (Bucharest, 1969) vol 1 p 665

[67] Bilbao L and Bruzzone H 1984 *Phys. Lett.* **A101** 261

[68] Bernard A, Coudeville A, Garçonnet J P, Jolas A, de Mascureau J, and Nazet C 1977 in *Plasma Phys. and Contr. Nuclear Fusion Research (Proc. 6th Int. Conf.)* (Berchtesgaden, 1976) vol 3 (Vienna: International Atomic Energy Agency) p 471

[69] Oppenländer T, Pross G, Decker G, and Trunk M 1977 *Plasma Phys.* **19** 1075

[70] Gourlan C, Kroegler H, Maisonnier C, Oppenländer T, and Rager J P in *Proc. Eighth European Conf. on Contr. Fusion and Plasma Phys.* (Prague, 1977) vol 2 p 247

[71] Kobata T S 1984 *Plasma Phys. Contr. Fusion* **26** 575

[72] Ananin S I, Vikhrev V V, and Filippov N V 1978 *Sov. J. Plasma Phys.* **4** 175

[73] Bruzzone H, Moreno C, and Kelly H 1991 *Meas. Sci. and Tech.* **2** 1195

[74] Morgan P and Peacock N in *Proc. Second Topical Conf. on Pulsed High Density Plasmas* (Garching, 1972) vol 1 p E9

[75] Schmidt H, Nahrath B, and Rückle B in *Proc. Seventh European Conf. on Plasma Phys. and Nuclear Fusion* (Lausanne, 1975) vol 1 p 57

[76] Hamada F, Shimoda K, and Hirano K 1979 *Phys. Fluids* **22** 1217

[77] Kwek K H, Tou T Y, and Lee S 1990 *IEEE Trans. on Plasma Sci.* **PS–18** 826

[78] Bilbao L, Bruzzone H, Kelly H, and Esper M 1985 *IEEE Trans. on Plasma Sci.* **PS–13** 202

[79] Bilbao L, Bruzzone H, and Kelly H in *Proc. IEEE Int. Conf. on Plasma Sci.* (Arlington, 1987) p 118

[80] Kelly H and Giudice G 1990 *IEEE Trans. on Plasma Sci.* **PS–18** 646

[81] Bruzzone H and Fischfeld G 1989 *Phys. Lett.* **A134** 484

[82] Bostick W H, Grunberger L, Nardi V, and Prior W in *Proc. Fourth European Conf. on Contr. Fusion and Plasma Phys.* (Rome, 1970) vol 1 p 108

[83] Bruzzone H, Gratton R, Kelly H, Milanese M, and Pouzo J 1976 in *Proc. Int. Conf. on Energy Storage, Compression and Switching* (Torino, 1974) ed W H Bostick, V Nardi, and O Zucker (London and New York: Plenum) p 255

[84] Bilbao L, Bruzzone H, and Nikulin V Ya 1980 *Associazione CNEN–EURATOM sulla Fusione, Frascati, Report CNEN–FAL 80.11*

[85] Basque G, Jolas A, and Watteau J P 1968 *Phys. Fluids* **11** 1384

[86] Gratton F and Vargas M in *Proc. Seventh European Conf. on Plasma Phys. and Nuclear* Fusion (Lausanne, 1975) vol 1 p 64

[87] Vargas M, Gratton F, Gratton J, Bruzzone H, and Kelly H 1977 in *Plasma Phys. and Contr. Nuclear Fusion Research (Proc. 6th Int. Conf.)* (Berchtesgaden, 1976) vol 3 (Vienna: International Atomic Energy Agency) p 483

[88] Gratton R, Kelly H, Milanese M, and Pouzo J 1980 *Phys Lett.* **A62** 422

[89] Dyachenko V and Imshennik V 1969 *Sov. Phys. JETP* **29** 947

[90] Behler K and Bruhns H 1987 *Phys. Fluids* **30** 3767

[91] Bilbao L, Bruzzone H, and Kelly H *Trends in Plasma Sci.* vol I p 785 (Council of Scientific Research Integration, India, 1990)

[92] Godunov S K, Filippov N V, and Filippova T I 1967 *Sov. Phys. JETP* **25** 755

[93] Bazdenkov S V, Gureev K G, and Filippov N V 1976 *Sov. J. Plasma Phys.* **2** 406

[94] Schmidt H 1987 in *Proc. Second Latin American Workshop on Plasma Phys. and Contr. Thermonuclear Fusion* (Medellin, 1987) vol 12 p 1 (CIF Series)

[95] Herold H, Kaeppeler H J, Sadowski M, Schmidt H, and Shakhatre M 1988 *Universität Stuttgart, Report IPF-88-1*

[96] Rager J P, Alexeev Y, Appelt J, Brzosko J S, Ehrhardt J, Gourlan C, Hübner K, Ingrosso L, Kazeev M, Kirchesch P, Klobukowska J, Kroegler H, Podda S, Robouch B V, and Steinmetz K 1982 *Frascati, Report 82.40/cc*

[97] Maxon S and Wainwright T 1984 *Phys. Fluids* **27** 2535

[98] Vikhrev V V and Braginskii S I 1986 *Rev. of Plasma Phys.* **10** 425

[99] Bernstein M J, Meskan D A, and van Paassen H L L 1969 *Phys. Fluids* **12** 2193

[100] Paduch M, Socha R, Tomaszewski K, and Wereszczynski Z 1991 *IPPLM Warsaw, Report 13/91*

[101] Wenzel N 1985 *Universität Heidelberg, Report IAP 1/85*

[102] Schmidt H and Rückle B 1978 *Appl. Optics* **17** 1275

[103] Bernard A, Garçonnet J P, Jolas A, Le Breton J P, and de Mascureau J in *Plasma Phys. and Contr. Nuclear Fusion Research (Proc. 7th Int. Conf.)* (Innsbruck, 1978) vol 2 (Vienna: International Atomic Energy Agency) p 159

[104] Lee S 1983 *Plasma Phys.* **25** 571

[105] Lee S 1983 *Australian J. Phys.* **35** 891

[106] Sasorov P V 1990 *Sov. J. Plasma Phys.* **16** 281

[107] Neil G R and Post R S 1981 *Plasma Phys.* **23** 425

[108] Bernard A 1978 *Atomkernenergie* **32** 73

[109] Bernard A, Jolas A, Garçonnet J P, de Mascureau J, Nazet C, Coudeville A, and Békiarian A 1977 *Report CEA-R-4807*

[110] Herold H, Kaeppeler H J, Schmidt H, Schumacher A, Shakhatre M and Win Thein in *Proc. Workshop on Plasma Focus and Z-Pinch* (Toledo, 1987) p 7

[111] Bernard A, Garçonnet J P, Jolas A, Le Breton J P, de Mascureau J, and Romary P in *Proc. IEEE Int. Conf. on Plasma Sci.* (Montreal, 1979) vol Invited Papers

[112] Bernard A, Garçonnet J P, Jolas A, Le Breton J P, and de Mascureau J in *Proc. Third Int. Topical Conf. on High Power Electron and Ion Beam Research and Technology* (Novosibirsk, U.S.S.R., 1979)

[113] Bernstein M J 1970 *Phys. Fluids* **13** 2858

[114] Trubnikov B A 1986 *Sov. J. Plasma Phys.* **12** 490

[115] Ivanov A A and Rudakov L I 1970 *Zh. Èksp. Teor. Fiz.* **58** 1332

[116] Molen G M 1983 in *Proc. IInd Int. Conf. on Energy Storage, Compression and Switching* (Venice, 1978) vol 2 (New York: Plenum) p 629

[117] Stygar W, Gerdin G, Venneri F, and Mandreakas J 1982 *Nucl. Fusion* **22** 1161

[118] Smith J R, Luo C M, Rhee M J, and Schneider R F 1985 *Phys. Fluids* **28** 2305

[119] Denus S, Dubrovskiĭ A V, and Gribkov V A 1987 *Kratkie Soobshchenia po Fizike* **11** 32

[120] Aleksandrov A A, Gribkov V A, and Kushin V V 1977 *Kratkie Soobshchenia po Fizike* 9 26

[121] Gullickson R L and Barlett R H 1975 in *Proc. Adv. in X-ray Anal.* vol 18 p 184

[122] Choi P, Deeney C, and Wong C S 1988 *Phys. Lett.* **A128** 80

[123] Choi P, Deeney C, Herold H, and Wong C S 1990 *Laser Part. Beams* **8** 469

[124] Jakubowski L, Sadowski M, and Schmidt H in *Proc. Workshop on Phys. of Alternative Magnetic Confinement Schemes* (Varenna, 1990) p 1001

[125] Decker G, Pross G, Rückle B, Schmidt H, and Shakhatre M 1975 in *Proc. 3rd Topical Conf. on Pulsed High Beta Plasmas* p 401

[126] Afanasiev Yu V, Basov N G, Gribkov V A, Isakov A I, Kalachev N V, Krokhin O N, Krupnova L V, Nikulin V Ya, Pustovalov V V, Romanov A B, Savchenko M A, Semenov O G, Silin V P, and Sklizkov G V 1978 *P N Lebedev Physical Institute, Report (Trudy FIAN)* vol 103 (Moscow: Nauka) p 202

[127] Gribkov V A 1976 in *Proc. Int. Conf. on Energy Storage, Compression and Switching* (Torino, 1974) ed W H Bostick, V Nardi, and O Zucker (London and New York: Plenum) p 270

[128] Gribkov V A, Dubrovskiĭ A V, Isakov A I, Kalachev N V, Kozlova T A, Korzhavin V M, and Nikulin V Ya 1980 *P N Lebedev Physical Institute, Report (Trudy FIAN)* vol 127 (Moscow: Nauka) p 32

[129] Gribkov V A, Krokhin O N, Sklizkov G V, Filippov N V, and Filippova T I 1976 *P N Lebedev Physical Institute, Report (Trudy FIAN)* vol 85 (Moscow: Nauka) p 193

[130] van Paassen H L L, Vandre R H, and White S R 1970 *Phys. Fluids* **13** 2606

[131] Johnson D L 1974 *J. Appl. Phys.* **45** 1147

[132] Gribkov V A, Dubrovskiĭ A V, Kalachev N V, Krokhin O N, and Sledzinski S 1989 in *First Symposium on Radiative Plasma Dynamics* ed Y S Protasov vol 2 (Moscow: Ènergoatomizdat)

[133] Krauz V I, Salukvadze R G, and Khautiev E Y 1985 *Sov. J. Plasma Phys.* **11** 163

[134] Filippov N V and Filippova T I in *Plasma Phys. and Contr. Nuclear Fusion Research (Proc. 2nd Int. Conf.)* (Culham, 1965) (Vienna: International Atomic Energy Agency) p 270

[135] Gribkov V A, Isakov S A, and Romanov A B 1984 *Kratkie Soobshcheniya po Fizike* **11** 60

[136] Choi P, Deeney C, Herold H, and Wong C S in *Proc. 1988 Z-Pinch and Plasma Focus Workshop* (Nice, 1988) p 76

[137] Decker G, Deutsch R, Kies W, and Rybach J 1985 *Plasma Phys. Contr. Fusion* **27** 609

[138] Schmitt K, Krompholz K, Rühl F, and Herziger G 1983 *Phys. Lett.* **95A** 239

[139] Nardi V 1979 in *Plasma Phys. and Contr. Nuclear Fusion Research (Proc. 7th Int. Conf.)* (Vienna, 1978) vol 2 (Vienna: International Atomic Energy Agency) p 143

[140] Gribkov V A in *Proc. IEEE Int. Conf. on Plasma Sci.* (Monterey, 1978)

[141] Harries W L, Lee J H, and McFarland D R 1978 *Plasma Phys.* **20** 95

[142] Bernard A, Garçonnet J P, Jolas A, Le Breton J P, and de Mascureau J 1983 in *Proc. IInd Int. Conf. on Energy Storage, Compression and Switching* (Venice, 1978) vol 2 (New York: Plenum) p 307

[143] Kondoh J, Shimoda K, and Hirano K 1981 *Jap. J. Appl. Phys.* **20** 393

[144] Bernstein M J, Meskan D A, and van Paassen H L L 1969 *Phys. Fluids* **12** 2193

[145] Beckner E H 1966 *J. Appl. Phys.* **37** 4944

[146] Peacock N J, Speer R J, and Hobby M G 1969 *J. Phys. B: Atom. and Molec. Phys.* **2** 798

[147] Bostick W H, Nardi V, and Prior W 1972 *J. Plasma Phys.* **8** 7

[148] Venneri F, Boulais K, and Gerdin G 1990 *Phys. Fluids* **B2** 1613

[149] Filippov N V 1983 *Sov. J. Plasma Phys.* **9** 14

[150] Neff W, Eberle J, Holz R, Lebert R, and Richter F 1989 *SPIE* **1140** 1310

[151] Kato Y and Be S H 1986 *Appl. Phys. Lett.* **48** 686

[152] Kato Y, Ochiai I, Watanabe Y, and Murayama S 1988 *J. Vac. Sci. Technol.* **B6** 195

[153] Koshelev K N, Krauz V I, Reshetnyak N G, Salukvadze R G, Sidel'nikov Y V, and Khautiev E Y 1988 *J. Phys. D: Appl. Phys.* **21** 1827

[154] Herold H, Kaeppeler H J, Schmidt H, Shakhatre M, Wong C S, Deeney C, and Choi P 1989 in *Plasma Phys. and Contr. Nuclear Fusion Research (Proc. 12th Int. Conf.)* (Nice, 1988) vol 2 (Vienna: International Atomic Energy Agency) p 587

[155] Bayley J M, Decker G, Kies W, Mälzig M, Müller F, Röwekamp P, Westheide J, and Sidel'nikov Y V 1991 *J. Appl. Phys.* **69** 613

[156] Zoita V, Presura R, Dumitrescu-Zoita C, and Herold H 1993 *Chinese Phys. Lett.* **10** 200

[157] Shearer J W 1976 *Phys. Fluids* **19** 1426

[158] Vikhrev V V 1978 *JETP Lett.* **27** 95

[159] Peacock N J, Hobby M G, and Morgan P D 1971 in *Plasma Phys. and Contr. Nuclear Fusion Research (Proc. 4th Int. Conf.)* (Madison, 1971) vol 1 (Vienna: International Atomic Energy Agency) p 537

[160] van Paassen H L L, Vandre R H, and White R S 1970 *Phys. Fluids* **13** 2606

[161] Lee J H, Loebbaka D S, and Roos C E 1971 *Plasma Phys.* **13** 347

[162] Fichtel C E and McDonald F B 1967 *Ann. Rev. Astron. Astrophys.* **5** 531

[163] Gribkov V A 1993 *Chinese Phys. Lett.* **10** 26

[164] Bourgade J L, Cavailler P, de Mascureau J, and Miquel J L 1986 *Rev. Sci. Instrum.* **57** 2165

[165] Presura R and Zoita V in *Proc. Sixteenth Int. Conf. on X-ray and inner-shell processes* (Debrecen, Hungary, 1993) p 104

[166] Richter F, Eberle J, Holz R, Neff W, and Lebert R in *Proc. Second Int. Conf. on Dense Z-Pinches* (Laguna Beach, 1989) vol 1 p 515 (*AIP Conf. Proc. Ser.*) (New York, 1989)

[167] Yokoyama M, Kitagawa Y, Yamanaka C, and Hirano K 1981 in *Plasma Phys. and Contr. Nuclear Fusion Research (Proc. 8th Int. Conf.)* (Brussels, 1980) vol 2 (Vienna: International Atomic Energy Agency) p 187

[168] Gullickson R L and Barlett R H 1974 in *Advances in X-Ray Analysis* ed W L Pickles vol 18 (New York: Plenum) p 184

[169] Gates D C 1983 in *Proc. IInd Int. Conf. on Energy Storage, Compression, and Switching* (Venice, 1978) vol 2 (New York: Plenum) p 329

[170] Pereira N R and Davis J 1988 *J. Appl. Phys.* **64** R1

[171] Ivanov V D, Kochetov V A, Moiseeva M P, Palkin A A, Svirskii E B, Terentiev A R, Filippov N V, Filippova T I, Veretennikov V A, Vyskubov V P, Gribkov V A, Dubrovskiǐ A V, Isakov A I, Kalachev N V, Kozlova T A, Korzhavin V M, Krokhin O N, Nikulin V Ya, Semenov O G, Silin P V, Suvorov V A, and Cheblukov Y N 1981 in *Plasma Phys. and Contr. Nuclear Fusion Research (Proc. 8th Int. Conf.)* (Brussels, 1980) vol 2 (Vienna: International Atomic Energy Agency) p 161

[172] Zoita V, Presura R, Gherendi F, and Dumitrescu-Zoita C 1993 in *Proc. Twentieth IEEE Int. Conf. on Plasma Sci.* (Vancouver, 1993) p 584

[173] Kaeppeler H J in *Proc. 1987 Workshop on Plasma Focus and Z-pinch* (Toledo, 1987) p 59

[174] Conrads H, Cloth P, Demmeler M, and Hecker R 1972 *Phys. Fluids* **15** 209

[175] Sadowski M, Zebrowski J, Rydygier E, and Kucinski J 1988 *Plasma Phys. Contr. Fusion* **30** 763

[176] Nardi V 1987 in *Megagauss Technology and Pulsed Power Applications* (New York and London: Plenum) p 269

[177] Schneider R F and Lee M J in *Proc. Fourth Int. Workshop on Plasma Focus and Z-Pinch Research* (Warsaw, 1985) p 108

[178] Sadowski M, Zebrowski J, Rydygier E, Herold H, Jäger U, and Schmidt H 1985 *Phys. Lett.* **113A** 25

[179] Yamamoto T, Shimoda K, and Hirano K 1985 *Jap. J. Appl. Phys.* **24** 324

[180] Bocancea A and Mandache N 1983 *Rev. Roum. Phys.* **28** 413

[181] Sadowski M and Chyrczakowski S 1983 in *Proc. Third Int. Workshop on Plasma Focus* Research (Stuttgart, 1983) p 39 (Institut für Plasmaforschung, Report IPF–83–6)

[182] Khautiev E Y and Krauz V I in *Proc. Eleventh European Conf. on Contr. Fusion and Plasma Phys.* (Aachen, 1983) p 505

[183] Mozer A, Sadowski M, Herold H, and Schmidt H 1982 *J. Appl. Phys.* **53** 2959

[184] Cebanu A, Chera T, Dinu L, Ionescu G, Ionescu–Bujor T, Iordanescu A, Mandache N, Tsois N, Vlad M, Zaharescu M, Zambreanu V, and Zoita V 1981 in *Plasma Phys. and Contr. Nuclear Fusion Research (Proc. 8th Int. Conf. 1980)* vol 2 (Vienna: International Atomic Energy Agency) p 197

[185] Bertalot L, Herold H, Jäger U, Moser A, Oppenländer T, Sadowski M, and Schmidt H 1980 *Phys. Lett.* **79A** 389

[186] Maisonnier C and Rager J P 1979 *Report CNEN 79.31cc*

[187] Filippov N V and Filippova T I 1979 *Sov. JETP Lett.* **29** 689

[188] Gullickson R and Sahlin H 1978 *J. Appl. Phys.* **49** 1099

[189] Krompholz H and Michel L 1977 *Appl. Phys.* **13** 29

[190] Belayaeva I F and Filippov N V 1973 *Nucl. Fusion* **13** 881

[191] Filippov N V *et al* 1979 *JETP* **76** 1547

[192] Imshenik V S, Osaovets S M, and Ostroshchenko I V 1973 *Sov. Phys. JETP* **37** 1037

[193] Kondoh Y and Hirano K 1978 *Phys. Fluids* **21** 1617

[194] Schönbach K, Krompholz H, Michel L, and Herziger G 1977 *Phys. Lett.* **62A** 430

[195] Gary S P and Hohl F 1978 *Los Alamos Laboratory, Report LA UR78-518*

[196] Gary S P 1974 *Phys. Fluids* **17** 2135

[197] Hsieh S L, Bloomberg H W, and Gary S P 1975 *Plasma Phys.* **1** 53

[198] Gureev K G 1980 *Sov. J. Tech. Phys.* **25** 192

[199] Sahlin H L 1976 in *Proc. Int. Conf. on Energy Storage, Compression and Switching* (Torino, 1974) ed W H Bostick, V Nardi, and O Zucker (London and New York: Plenum) p 219

[200] Haines M G 1983 *Nucl. Instrum. Meth.* **207** 179

[201] Deutsch R and Kies W 1988 *Plasma Phys. Contr. Fusion* **30** 263

[202] Goldstein S A and Lee R 1975 *Phys. Rev. Lett.* **35** 1079

[203] Jäger U and Herold H 1987 *Nucl. Fusion* **27** 407

[204] Bernard A, Coudeville A, Garçonnet J P, Jolas A, de Mascureau J, and Nazet C 1978 *Journal de Physique Colloque C1, supplément au n° 5* **39** C1

[205] Jassby D L 1979 *Report PPPL-1515/UC-20 a*

[206] Schmidt H in *Proc. Fifth Int. Workshop on Plasma Focus and Z-Pinch Research* (Toledo, 1987) p 65

[207] Gates D C and Demeter L J 1970 in *Proc. Bull. APS* p 1494

[208] Trubnikov B A 1986 *Sov. J. Plasma Phys.* **12** 271

[209] Vikhrev V V 1986 *Sov. J. Plasma Phys.* **12** 262

[210] Nardi V, Bilbao L, Bortolotti A, Brzosko J S, Powell C, and Zeng D 1989 in *Plasma Phys. and Contr. Nuclear Fusion Research (Proc. 12th Int. Conf.)* (Nice, 1988) vol 2 (Vienna: International Atomic Energy Agency) p 743

[211] Gentilini A, Maisonnier C, and Rager J P 1979 *Comments on Plasma Phys.* **5** 41

[212] Decker G, Kies W, and Pross G 1983 *Phys. Fluids* **26** 571

[213] Brzosko J S, Klobukowska J, and Robouch B V 1984 *ENEA, Report RT/FUS/84/6*

[214] Herold H, Bertalot L, Deutsch L, Grauf W, Jaeger U, Kaeppeler H J, Lepper F, Oppenländer T, Schmidt H, Schmidt R, Schwarz J, Schwoerer K, Shakhatre M, Hayd A, Maurer M, and Meinke P 1982 in *Plasma Phys. and Contr. Nuclear Fusion Research (Proc. 9th Int. Conf.)* (Baltimore, 1982) vol 2 (Vienna: International Atomic Energy Agency) p 405

[215] Schmidt H, Herold H, Bertalot L, Jaeger U, Kaeppeler H J, Lepper F, Schmidt R, Schwarz J, and Shakhatre M 1984 *Atomkernenergie/Kerntechnik* **44** 191

[216] Lee J H, Shomo L P, and Kim K H 1972 *Phys. Fluids* **15** 2433

[217] Michel L, Krompholz H, and Herziger G 1982 *Phys. Lett.* **88A** 400

[218] Mandache N, Tiseanu I, Zambreanu V, Zoita V, Serban A, and Doloc C in *Proc. Eighteenth European Conf. on Contr. Fusion and Plasma Phys.* (Berlin, 1991) vol 2 p 333

[219] Bernard A 1975 in *Proc. 3rd Topical Conf. on Pulsed High Beta Plasmas* p 69

[220] Genta P 1976 *Commissariat à l'Énergie Atomique, Report CEA-R-4772*

[221] Rager J P in *Proc. Tenth European Conf. on Contr. Fusion and Plasma Phys.* (Moscow, 1981) vol 2 p 71

[222] Tiseanu I, Presura R, Zoita V, Choi P, Haines M G, Aliaga R, and Herold H in *Proc. 33rd Annual Meeting Div. Plasma Phys. Am. Phys. Soc.* (Tampa, FL, 1991)

[223] Schmidt R *Untersuchung über den Ablauf der Fusionsprozesse im Plasmafokus unter Verwendung von zeitaufgelöster Neutronenspektroskopie, Doctorate thesis* (Universität Stuttgart, 1987)

[224] Rager J P, Robouch B V, Hübner K, and Steinmetz K 1981 *Frascati, Report 81.25*

[225] Kruse H W and Minerbo G N in *Proc. IEEE Int. Conf. on Plasma Sci.* (Santa Fe, NM, 1981)

[226] Vlad M 1984 *Nucl. Instrum. Meth. in Phys. Res.* **227** 327

[227] Vlad M, Ganciu M, Ivascu M, Mandache N, Spineanu F, and Zoita V 1989 *Nucl. Instrum. Meth. in Phys. Res.* **A274** 613

[228] Schmidt R and Herold H 1987 *Plasma Phys. Contr. Fusion* **29** 523

[229] Deutsch R and Kies W 1988 *Plasma Phys. Contr. Fusion* **30** 921

[230] Muehling E, Schumacher U, and Paretzke H G 1984 *Nucl. Tracks* **9** 113

[231] Bosch H 1987 *Institut für Plasmaphysik, Garching, Report IPP III/116*

[232] Jäger U 1986 *Über die Reaktionsmechanismen im Plasmafokus. Untersuchungen an beschleunigten Deuteronen und Reaktionsprotonen, Doctorate thesis* (Universität Stuttgart)

[233] Nardi V, Bilbao L, Brzosko J S, Powell C, Zeng D, Bortolotti A, Mezzetti F, and Robouch B V 1988 *IEEE Trans. on Plasma Sci.* **16** 374

[234] Bernard A, Coudeville A, Garçonnet J P, Jolas A, de Mascureau J, and Watteau J P in *Proc. Eighth European Conf. on Contr. Fusion and Plasma Phys.* (Prague, 1977) vol 1 p 64

[235] Vikhrev V V, Gureev K G, Zhdanov S K, Korzhavin V M, and Trubnikov B A 1977 in *Plasma Phys. and Contr. Nuclear Fusion Research (Proc. 6th Int. Conf.)* (Berchtesgaden, 1976) vol 3 (Vienna: International Atomic Energy Agency) p 475

[236] Gribkov V A, Krokhin O N, Sklizkov G V, Filippov N V, and Filippova T I 1973 in *Proc. Sixth European Conf. on Contr. Fusion and Plasma Phys.* (Moscow, 1973) vol 1 p 375 (Joint Institute for Nuclear Research)

[237] Tsitovich V N 1977 *Theory of Turbulent Plasma* vol 1 (London and New York: Plenum)

[238] Bazdenkov S V, Gureev K G, Filippov N V, and Filippova T I 1973 *JETP Lett.* **18** 118

[239] Schmidt H 1987 *Universität Stuttgart, Report IPF-87-5*

[240] Gribkov V A, Korzhavin V M, Krokhin O N, Nikulin V Ya, Sklizkov G V, Filippov N V, and Filippova T I in *Proc. Fifth European Conf. on Contr. Fusion and Plasma Phys.* (Grenoble, 1972) vol 1 p 64 (Commissariat à l'Énergie Atomique, 1972)

[241] Khautiev E Y, Koshelev K N, Sidel'nikov Y V, Gribkov V A, and Krokhin O N 1989 in *Plasma Phys. and Contr. Nuclear Fusion Research (Proc. 12th Int. Conf.)* (Nice, 1988) vol 2 (Vienna: International Atomic Energy Agency) p 579

[242] Shearer J M 1976 *Phys. Fluids* **19** 1426

[243] Vikhrev V V 1978 *JETP Lett.* **27** 95

[244] Kingsep A S, Chukbar K V, and Yan'kov V V 1987 in *Plasma Theory Problems* ed L A Leontovich vol 16 (Moscow: Atomizdat) p 209

[245] Gribkov V A and Krokhin O N 1981 *P N Lebedev Physical Institute, Report Preprint No 57*

[246] Lee R and Lampe M 1973 *Phys. Rev. Lett.* **31** 1390

[247] Trubnikov B A 1958 in *Fizika Plazmy i Problema Upravlyaemykh Termoyadernykh Reaktsiĭ* ed L A Leontovich vol 4 (Moscow: Academia Nauk SSSR) p 89

[248] Trubnikov B A and Zdanov S K 1976 *Zh. Èksp. Teor. Fiz.* **70** 92

[249] Filippov N V 1981 *Plazmennyĭ Focus, Doctorate thesis* (I V Kurchatov Institute of Atomic Energy)

[250] Syrovatskiĭ S I 1966 *Astron. J.* **43** 340

[251] Nardi V 1976 in *Proc. Int. Conf. on Energy Storage, Compression and Switching* (Torino, 1974) ed W H Bostick, V Nardi, and O Zucker (London and New York: Plenum) p 173

[252] Neff W, Noll R, Rühl F, Lebert R, Haas C R, Weikl B, and Herziger G 1989 *Nucl. Instrum. Meth. in Phys. Res.* **A285** 253

[253] Filippov N V 1972 *I V Kurchatov Institute of Atomic Energy, Report IAE N 3996/6*

[254] Notkin G E, Filippov N V, and Shcheglov D A in *Proc. Fifth European Conf. on Contr. Fusion and Plasma Phys.* (Grenoble, 1972) vol 1 p 69 (Commissariat à l'Énergie Atomique, 1972)

[255] Oppenländer T 1981 *Experimentelle Untersuchung des Einflusses hoher Spannungen auf einen Plasmafokus, Doctorate thesis* (Universität Stuttgart)

[256] Forrest M J, Norton B A, and Peacock N J 1973 in *Proc. Sixth European Conf. on Contr. Fusion and Plasma Phys.* (Moscow, 1973) vol 1 p 363 (Joint Institute for Nuclear Research)

[257] Bostick W H, Nardi V, Prior W J, and Rodriguez–Trelles F in *Proc. Fifth European Conf. on Contr. Fusion and Plasma Phys.* (Grenoble, 1972) vol 1 p 70 (Commissariat à l'Énergie Atomique, 1972)

[258] Rager J P and Hübner K in *Proc. Second Int. Workshop on Plasma Focus* (Moscow, 1981) vol 1 (also *CNEN Preprint, 1982*)

[259] Mather J and Ahluwalia H S 1988 *IEEE Trans. on Plasma Sci.* **16** 56

[260] Conrads H, Gollwitzer D, and Schmidt H 1973 in *Proc. Sixth European Conf. on Contr. Fusion and Plasma Phys.* (Moscow, 1973) vol 1 p 367 (Joint Institute for Nuclear Research)

[261] Cheblukov Yu N, Gribkov V A, Fedotov Yu V, Isakov A I, Il'in Yu M, Krokhin O N, Lavrov N N, Ovechkin V N, and Suvorov V A 1979 *Kratkie Soobshcheniya po Fizike* **12** 37

[262] Bostick W H, Nardi V, and Prior W 1976 in *Pulsed High Beta Plasmas*, ed Evans (Oxford and New York: Pergamon) p 408

[263] Kaplan S A, Pikel'ner S B, and Tsytovich V N 1977 in *Phys. of Plasma in the Solar Atmosphere* (Moscow: Nauka)

[264] Schmitt K, Krompholz H, Rühl F, and Herziger G 1983 *Phys. Lett.* **95A** 239